MACHINE LEARNING FOR RESERVOIR CHARACTERIZATION AND TIME-LAPSE SEISMIC ANALYSES

by
Marwa Hussein

A dissertation submitted to the Department of Earth and Atmospheric Sciences,
College of Natural Sciences and Mathematics
in partial fulfillment of the requirements for the degree of

Doctor of Philosophy

in Geophysics

Chair of Committee: Robert R. Stewart

Committee Member: David H. Johnston

Committee Member: Yingcai Zheng

Committee Member: Jiajia Sun

University of Houston
August 2020

DEDICATION

To my family, especially my mom Fatma Mohamed

ACKNOWLEDGMENTS

I would like to thank God, for giving me wisdom whenever I asked him and for an amazing life filled with health and happiness. I think it is implicit that such an achievement is not only because of my own merits. There is a large list of people who have helped me achieve today's (July 10th, 2020) goal.

First, I want to thank my family for standing by me and supporting me all these years. I like to thank my advisor Dr. Robert Stewart for the opportunity to work with him and for supporting me throughout my degree program. He always encourages us to try new research ideas and collaborate with other experts. I thank him for being a motivator to reach different milestones in the Ph.D. program. I would like to express my sincere gratitude to Dr. David Johnston for teaching me everything I know in 4D seismic studies, for reviewing and editing my manuscripts and for useful discussion. I also would like to thank my committee members, Dr. Yingcai Zheng and Dr. Jiajia Sun for their support in finishing my Ph.D.

During my 4-year program, I spent about a year working with Dr. Jonny Wu in his research group. I would express my most profound appreciation to his help, his useful technical discussion and advice. I would to acknowledge Dr. Tom Smith, Ms. Deborah Sacrey, Dr. Kurt Marfurt and Mr. Rocky Roden for their useful technical discussions and collaborations. I thank Ezzedeen Alfataierge and Spencer Fuston for their help with Visa software and geology discussion, respectively.

Lastly, but not less important, special thanks to Mr. Roland Swift, Mr. Rajas Athale, Dr. Ahmed Anwer, Mr. Said Elnoamany, Dr. Mosab Nasser, Dr. Yasser Metwally, Dr. Islam Mohamed, Mr. Islam Yehia, Mr. Mahmoud Raslan, Mr. Gary Guthrie, Mr. Mahmoud Ismaiel, Dr. Ehab Hassan and Dr. Osman Hassan for their useful technical discussions and advice.

ABSTRACT

Successful reservoir management requires a clear understanding of reservoir distribution, quality, heterogeneity, and baffles. During field development, static reservoir models are built by incorporating well logs, core, and seismic data. However, seismic amplitude data often cannot image small faults, resolve thin reservoirs, or discriminate subtle changes in reservoir properties. Seismic attributes aid in illuminating subtle faults and stratigraphic features but, analyzing numerous individual attributes can be tedious and may have limitations for revealing small petrophysical changes within a reservoir.

Using the Maui 3D dataset acquired in the offshore Taranaki Basin of New Zealand, I generate seismic attributes that are sensitive to faults as well as attributes that are sensitive to reservoir properties. I use principal component analysis (PCA) and self-organizing maps (SOM) to integrate geological information from six geometric attributes into one classification volume, which shows small faults that could affect field compartmentalization. I also develop a machine learning workflow to combine the reservoir information from eight spectral instantaneous attributes into one clustered volume. This SOM classification shows the reservoir distribution and helps to understand reservoir quality and to illuminate thin baffles.

During reservoir production, time-lapse (4D) seismic data can be acquired to monitor fluid movement and constrain simulation models. However, 4D seismic data suffer from seismic interference and tuning effects. Thus, it can be challenging to monitor fluid behavior within thin reservoirs and/or to illuminate baffles. As a result, the reservoir simulation model may not capture sufficient reservoir heterogeneity detail, which can lead to a mismatch between synthetic models and observed 4D seismic responses.

Using the 4D seismic data from the Maui field, I develop a systematic workflow to carefully select the attributes that best show 4D changes and integrate the preproduction and postproduction reservoir information from multiple 4D spectral instantaneous attributes into 4D classification volumes. Changes in SOM cluster patterns between baseline and monitor surveys suggest production-related changes within good to poor quality reservoirs that are primarily caused by water saturation changes as the reservoir is being water swept. Geobodies derived from the SOM clusters are used to calculate recoverable gas reserves that are compared to production data.

TABLE OF CONTENTS

DEDICATION III

ACKNOWLEDGMENTS IV

ABSTRACT V

TABLE OF CONTENTS VII

LIST OF TABLES IX

LIST OF FIGURES X

LIST OF ACRONYMS XXIV

1 INTRODUCTION 1

1.1 Overview 1

1.2 Dissertation outline 4

2 WHICH SEISMIC ATTRIBUTES ARE BEST FOR SUBTLE FAULT DETECTION? 7

2.1 Summary 7

2.2 Introduction 8

2.3 Geologic Background 12

2.4 Dataset 17

2.5 Methodology 18

2.6 Seismic attribute analysis 20

2.7 Interactive seismic attribute interpretation 26

2.7.1 Attribute selection for a human interpreter 27

2.7.2 Attribute selection for SOM analysis 35

2.8 Discussion 40

2.9 Conclusions 43

3 MACHINE LEARNING FOR RESERVOIR EVALUATION AND ROCK TYPE IDENTIFICATION FROM SEISMIC DATA 44

3.1 Summary 44

3.2 Introduction 45

3.3 Depositional characteristics of C Sand reservoir 48

3.4 Dataset 51
3.5 Methodology 52
3.6 Petrophysical characteristics of the C sand reservoir 55
3.7 Seismic attribute selection 57
3.8 SOM for net reservoir discrimination and rock type identification 62
3.9 SOM for net reservoir discrimination 65
3.10 Rock typing analysis 67
3.11 SOM-derived petrophysical flow units 77
3.12 Discussion 86
3.13 Conclusions 90
4 UNSUPERVISED MACHINE LEARNING FOR TIME-LAPSE SEISMIC STUDIES AND RESERVOIR MONITORING 91
4.1 Summary 91
4.2 Introduction 92
4.3 Field history 95
4.4 Dataset 96
4.5 Methodology 98
4.6 4D Modeling and interpretation 102
4.7 Seismic attribute selection 110
4.8 Unsupervised machine learning (SOM) for 4D seismic studies 116
4.9 SOM for reservoir monitoring 119
4.10 Geobody extraction and volumetric calculations 134
4.11 Discussion 138
4.12 Conclusions 141
5 CONCLUSIONS 142
6 FUTURE WORK 145
BIBLIOGRAPHY 147
APPENDICES 164
A. Seismic data conditioning 164
B. **Mathematical background of seismic attributes used 168**

LIST OF TABLES

3. 1 Petrophysical properties summaries of C1 reservoir for four Maui wells. 56

3. 2 R35 rock type classification of the C1 Sand reservoir based on Martin et al., 1997 R35 classification scheme and Winland crossplot. 67

3. 3 FZI rock type classification of the C1 Sand reservoir based on Sritongthae 2016 classification scheme. 71

4. 1 Fluid properties of C1 Sand reservoir..... 103

4. 2 Dry frame rock properties of C1 Sand reservoir..... 103

4. 3 C1U reservoir properties and recoverable gas volumes calculated from the baseline and monitor SOM classification geobodies. The gas expansion factor (GEF) used in the computation is 230 136

LIST OF FIGURES

2. 1 Location map of Taranaki basin, offshore west North Island, New Zealand. (modified from Google Earth). (a) Map of Maui hydrocarbon field, seismic survey coverage and wells (modified from Haque et al., 2016; Baur et al., 2010; Franzel, 2019). CEF – Cape Egmont Fault; WF - Whitiki Fault; PF - Pungawerewere Fault; IF - Ihi Fault; AF - Alpine Fault; MPA & MPB - Maui A and Maui B platforms. (b) Paleogene stratigraphic column of Maui field (modified from Pannett et al., 2004 and Reilly et al., 2016). 13

2. 2 Maui field subsurface geologic context shown by: (a) Seismic-to-well tie for MB-11 well shows the C Shale, C Sand and D Sand seismic events. The tracks from left to right are Gamma ray (GR), Compressional velocity (Vp), Density (DENS) and Resistivity(RESD, RESS) logs, composite seismic trace, zero-phase synthetic seismic trace and seismic trace extracted along the well and overlie seismic line; (b) Time structure map of the top C Sand reservoir showing two anticlinal features separated by a saddle. Circles with crosses show vertical wells that penetrated the interval of interest; (c) C Shale to D Sand isochron map shows the time thickness variation during the deposition of C Shale and C Sand reservoir. It aids in defining the syn-deposition faults affecting the C Sand reservoir and shows a half-graben-like basin structure; (d) A-A' seismic line (location shown by red line in b)) crosses the Maui A region. The area is affected by a set of normal faults that forms graben to half-graben-like structures. IF - Ihi fault; (e) B-B' seismic line (the blue line in b)) across the Maui B region showing the Whitiki fault (WF) bounding the west side of the Maui B anticline. 16

2. 3 Workflow to select useful attributes for machine learning analysis and a human interpreter. PSDM - prestack depth migrated; PC-SOF - principal component structure-oriented filtering;

GLCM - gray-level co-occurrence matrices; SOM – self-organizing map; PCA - principal component analysis. 19

2. 4 Comparison between horizon-based attributes and geometric attributes. (a) High spatial residual map. Horizon slices extracted along the top of C1 Sand reservoir from (b) Seismic amplitude, (c) Inline dip, (d) Crossline (Xline) dip, (e) Dip magnitude, (f) Multispectral similarity, (g) Broadband similarity, (h) Co-rendered spectral similarity, (i) Inline RMS amplitude gradient and (j) Crossline (Xline) RMS amplitude gradient volumes. White arrows show faults with clear offset. The red arrow shows noise. 21

2. 5 Horizon slices extracted along the top of the C1 Sand reservoir from (a) Long-wavelength most positive principal curvature (K1 long), (b) Long-wavelength most negative principal curvature (K2 long), (c) Short-wavelength most negative principal curvature (K2 short), (d) Long-wavelength amplitude curvature (e_pos_long), (e) Curvedness, (f) Shape index, (g) Long-wavelength reflector rotation (Krot long), (h) Euler curvature at zero degree (Ke-0 deg), (i) Euler curvature at 150-deg (Ke-150 deg). 24

2. 6 Horizon slices extracted along the top of the C1 Sand reservoir from (a) Total aberrancy magnitude (Tot_Ab_mag), (b) Maximum aberrancy magnitude (Max-Ab_mag), (c) Intermediate aberrancy magnitude (Int-Ab_mag) and (d) Minimum aberrancy magnitude (Min-Ab_mag) volumes. 25

2. 7 Horizon slices extracted along the top of the C1 Sand reservoir from (a) Dip azimuth, (b) Strike of long-wavelength most positive principal curvature (Strike of K1 long) and (c) Total aberrancy azimuth (Tot_Ab_azm) volumes. 25

2. 8 Horizon slices extracted along the top of the C1 Sand reservoir from (a) GLCM entropy (GLCM_Ent), (b) GLCM homogeneity (GLCM_Hom), (c) GLCM dissimilarity (GLCM_Dis) and (d) GLCM continuity (GLCM_Con) volumes. 26

2. 9 Multiattribute horizon slices extracted along the top of the C Sand reservoir from (a) Dip magnitude modulated by dip azimuth, (b) Co-rendered long-wavelength most positive (K1 long), most negative principal (K2 long) curvatures and multispectral energy ratio attributes, (c) Co-rendered short-wavelength most positive (K1 short), most negative (K2 short) principal curvatures and multispectral energy ratio similarity attributes, (d) Long-wavelength most positive principal curvature modulated by its strike, (e) Long-wavelength most negative principal curvature modulated by its strike, (f) Co-rendered reflector rotation (Krot long), curvedness and multispectral energy ratio similarity, (g) Shape index modulated with curvedness, (h) Co-rendered multispectral energy ratio similarity with total aberrancy magnitude and azimuth. Note multispectral energy ratio similarity and reflector rotation show the en-echelon faults (purple arrow) affecting Maui north whereas curvature and dip attributes show two continuous intersecting faults. Dip and curvature attributes show lineaments associated with Ihi fault (cyan arrow) and faults affecting the eastern and southern part of the field (white and green arrows) whereas energy ratio similarity shows segmented or no anomalies associated with those faults. The Whitiki fault (red arrow) can be detected on all attributes. . 28

2. 10 Arbitrary seismic line A-A' (location shown by green line in Fig. 5b) across the northern part of the Maui field extracted from (a) a preconditioned seismic volume, (b) co-rendered preconditioned seismic, dip magnitude, dip azimuth and broadband energy ratio similarity, (c) co-rendered preconditioned seismic amplitude, dip magnitude, dip azimuth and multispectral energy ratio similarity, (d) co-rendered preconditioned seismic amplitude, long-wavelength most positive and most negative principal curvature attributes. The red arrow refers to the top of the C Sand seismic event. The cyan, purple, and green arrows denote different kinds of faults affecting Maui north. The orange arrow refers to similarity anomalies that could be interpreted as channelized features. Vertical exaggeration is 7.5:1. 31

2. 11 Arbitrary seismic line B-B' (location shown by yellow line in Fig. 5b) that crosses the Ihi fault, extracted from (a) a preconditioned seismic volume, (b) co-rendered preconditioned seismic, dip magnitude, dip azimuth and broadband energy ratio similarity, (c) co-rendered preconditioned seismic amplitude, dip magnitude, dip azimuth and multispectral energy ratio similarity attributes, (d) co-rendered preconditioned seismic amplitude, long-wavelength most positive and most negative principal curvature attributes. The red arrows refer to the C Sand seismic event. The purple, green, and blue arrows denote different faults affecting Maui A region. The cyan and orange arrows indicate low energy ratio similarity anomalies that suggest deformation within the shales overlying the C Sand reservoir and small channelized features, respectively. Vertical exaggeration is 7.5:1. 34

2. 12 Proposed workflow from this study for clustering and combining data from six geometric seismic attributes by using PCAs and SOMs. GLCM - Gray-level co-occurrence matrix; PCA - principal component analysis; SOM - self-organizing map. 38

2. 13 Comparison between the preferred workflow from this study (left side) and a SOM generated by following a previous workflow of Lauden et al., (2019) (right side). (a) Horizon slice extracted along the top of the C Sand reservoir from our preferred SOM classification volume by using six weighted geometric attributes based on the proposed workflow in this study. (b) Expanded image of the far northern part of the field from a). (c) Expanded image of Ihi fault from a). (d) Horizon slice extracted along the top of the C Sand reservoir by using four geometric attributes as described by Lauden et al. (2019). (e) Expanded image of the far northern part of the field from d). (f) Expanded image of Ihi fault from d). (g) Horizon slice follows a) but only has the fault-related SOM neurons turned on. (h) Horizon slice follows d) but only has the fault-related SOM neurons turned on. This study SOM shows sharper fault edges (compare arrows in a) and b) and expanded images b), c), e) and f)). Horizon slice g) shows cleaner and sharper fault edges compared to slice h). 39

3. 1 Seismic-to-well tie for Maui-7 well shows C1U, C1M and C1L seismic events. Tracks from left to right display Gamma-ray (GR), Density-Neutron (DENS-NEUT), Compressional sonic velocity (Vp), Deep resistivity (RESD), Shale volume (VSH), Effective porosity (PHIE), Water saturation (SW) and Hydrocarbon saturation (SH) logs. 49

3. 2 A - B seismic line (location shown by black line in top C1 Sand time structure map) crosses Maui structure and pass through Maui-7, Maui-5 and Maui-3 wells. The black traces show synthetic traces genetrated for the three wells. This seismic line shows a thin shale layer (C1M) in Maui B area that is correlatable to carbonate cemented sand layer in Maui A that divides the C1U and C1L. 50

3. 3 Workflow for net reservoir discrimination and rock types identifications from well logs, core data, and 3D full stack seismic data. RQI - rock quality index; FZI - flow zone indicator; SMLP - stratigraphic modified Lorenz plot; SFP - stratigraphic flow profile; MLP - modified Lorenz plot; PSDM - prestack depth migrated; CWT - continuous wavelet transform; PCA - principal component analysis; SOM - self-organizing maps. 54

3. 4 Horizon slices along the top of the C1U reservoir extracted from spectral magnitude components volumes. Note, the reservoir tune in spectral slices b) to d). 58

3. 5 Comparison between horizon slices extracted along the C1U reservoir seismic amplitude and instantaneous attributes calculated from the preconditioned broadband seismic volume (a to c) and amplitude and instantaneous attributes computed from 38 Hz spectral voice (d to f). White and red arrows indicate channelized features and sheet-like facies which are better imaged by spectral sweetness compared to broadband sweetness slice. Circles with crosses show the vertical wells used in this study. The lines shown in a) display the locations of vertical sections of Figures 3.11, 3.12, 3.13 and 3.17. 60

3. 6 Proposed workflow to cluster and integrate data from eight spectral instantaneous seismic attributes by using PCAs and SOMs for net reservoir discrimination and rock types

identification. PSDM - prestack depth-migrated seismic; PCA - principal component analysis; SOM - self-organizing maps. 64

3. 7 Enlarged SW-NE arbitrary line of Figure 3.2 shows the SOM classification results co-rendered with seismic amplitude data (wiggle traces) and net reservoir discrete logs at the Maui wells. The neurons in circled in black in the SOM 2D colored legend indicate clusters correlated to net sand reservoir whereas the ones circled in red indicate clusters that are correlated to shales. The sold black horizon indicates the top of the C1 Sand reservoir, the top and bottom dash-horizons indicate 10 ms and 70 ms shifted horizons from the top of C1 Sand reservoir. 66

3. 8 Rock typing crossplots used in this study. (a) Winland crossplot of porosity vs. permeability colored by R35. (b) Porosity vs. permeability crossplot colored by FZI. Squares, triangles and circles indicate core data measured for the C1 Sand reservoir penetrated by Maui-7, Maui-5, and Maui-6 wells, respectively. Red, orange, green, light blue, and dark gray colored data points refer to rock types RT1, RT2, RT3, RT4, and RT5 respectively. (c) Box and whisker plot summaries the core porosity and core permeability data for the different rock types defined by FZI/RQI classification method for all cored wells included in this study. 70

3. 9 Graphical rock typing plots for the C1 Sand reservoir. Stratigraphic Modified Lorenz plot (SMLP; left) and Modified Lorenz Plot (MLP) established for Maui-7 (a, b), Maui-5 (c, d) and Maui-3 (e, f). The SMLP indicate the flow behavoir of the C1 Sand reservoir and show the various flows units of the reservoir. MLP is used to refine the preliminary flow units defined on SMLP. 73

3. 10 Stratigraphic flow profile (SFP) for the C1 Sand reservoir penetrated by (a) Maui-7, (b) Maui-5 and (c) Maui-3 wells. Tracks from left to right display measured depth (MD), Gamma ray (GR), Caliber (CALI), Bit size (BS), Core porosity (CPHI), Effective porosity (PHIE), Core permeability (CKair), Predicted permeability (K_pred), Pore throat radius (R35), Rock quality

index (RQI), Flow zone indicator (FZI), Storage capacity (%PHIH), Flow capacity (%KH), Reservoir process speed (K/PHI), Net reservoir flag (FLAG) and Flow units (FU). 75

3. 11 NW-SE vertical SOM sections co-rendered with seismic amplitude (wiggle traces) and crosses Maui-7 well, which display net reservoir and flow units discrete logs. The locations of vertical section is shown in Figure 3.5a. The black and orange circles in the SOM 2D map indicate SOM neurons correlate to high speed and normal reservoir flow units defined in the C1U and C1L whereas black circles indicate baffles defined in the C1M interval. The solid horizon indicates the top of the C1 Sand reservoir and the dotted horizons indicate 10 ms and 70 ms analysis window used in the SOM analysis. FU - flow unit; SOM - self-organizing maps; RES - net reservoir; NO_RES - non-reservoir interval. The location of this section is shown in Figure 3.5a. 78

3. 12 W-E vertical SOM sections co-rendered with seismic amplitude (wiggle traces) and crosses Maui-5 well, which display net reservoir and flow units discrete logs. The locations of vertical section is shown in Figure 3.5a. The black and orange circles in the SOM 2D map indicate SOM neurons correlate to high speed and normal reservoir flow units defined in the C1U and C1L whereas black circles indicate baffles defined in the C1M interval. The solid horizon indicates the top of the C1 Sand reservoir and the dotted horizons indicate 10 ms and 70 ms analysis window used in the SOM analysis. FU - flow unit; SOM - self-organizing maps; RES - net reservoir; NO_RES - non-reservoir interval. The location of this section is shown in Figure 3.5a. 79

3. 13 Nearly W-E vertical SOM sections co-rendered with seismic amplitude (wiggle traces) and crosses Maui-3 well, which display net reservoir and flow units discrete logs. The locations of vertical section is shown in Figure 3.5a. The black and orange circles in the SOM 2D map indicate SOM neurons correlate to high speed and normal reservoir flow units defined in the C1U and C1L whereas black circles indicate baffles defined in the C1M interval. The solid

horizon indicates the top of the C1 Sand reservoir and the dotted horizons indicate 10 ms and 70 ms analysis window used in the SOM analysis. FU - flow unit; SOM - self-organizing maps; RES - net reservoir; NO_RES - non-reservoir interval. The location of this section is shown in Figure 3.5a. 80

3. 14 3D views of SOM-derived flow units for (a) C1U clusters, high speed and normal reservoir SOM-derived flow units in C1U and penetrated by (b) Maui-7, (c) Maui-5, (d) Maui-3, and (e) Three previously mentioned Maui wells. M-3 - Maui-3; M-5 - Maui-5; M-6 - Maui-6; M-7 - Maui-7. 82

3. 15 3D views of SOM-derived flow units for (a) C1M clusters, baffle SOM-derived flow units in C1M and penetrated by (b) Maui-7, (c) Maui-5, (d) Maui-3 and (e) Three Maui wells. M-3 - Maui-3; M-5 - Maui-5; M-6 - Maui-6; M-7 - Maui-7. 84

3. 16 3D views of SOM-derived flow units for (a) C1L clusters, high speed to normal reservoir SOM-derived flow units in C1L and penetrated by (b) Maui-7, (c) Maui-5, (d) Maui-3 and (e) Three Maui wells. M-3 - Maui-3; M-5 - Maui-5; M-6 - Maui-6; M-7 - Maui-7. 85

3. 17 SOM-to-well validation of closely-spaced wells (1 km apart). NE- SW arbitrary vertical section extracted from SOM classification volume co-rendered with seismic amplitude data (wiggle display) and crosses Maui-7 and MB-11 wells penetrated the C1 Sand reservoir at Maui B region. The location of the vertical section is shown in Figure 3.5a). In SOM 2D color map, the neurons in black circles correlate to net reservoir and those circled in red correlate to shale or silty shale intervals. The location of this section is shown in Figure 3.5a. 87

3. 18 A pitfall in Gunter et al., 1997 rock typing graphical approach for shaley sand reservoir to silty shale intervals. (a) Stratigraphic Modified Lorenz Plot (SMLP), (b) Modified Loren Plot (MLP), (c) Stratigraphic Flow Profile (SFP) of C1 Sand reservoir at Maui-6. Flow units written in red indicate high speed reservoir flow units, the ones written in orange indicate normal reservoir flow units and those written in black indicate baffles. Note that the high speed and normal

reservoir flow units are correlated to non-reservoirs so, these flow units cannot be validated by SFP..... 89

4. 1 Location map of Maui field in Offshore Taranaki basin, New Zealand (modified from Google Earth, Pannett et al., 2004 and Van der Veeken, 2016). MA - Maui A wells; MB - Maui B wells; MPA & MPB - Maui A & B production platforms. M - Maui vertical wells..... 97

4. 2 Workflow for 4D modeling, interpretation and, attribute selection for unsupervised machine learning analysis. SOM - self-organizing map; PCA - principal component analysis. 100

4. 3 Normalized root mean square slice extracted from 250 ms above the C Shale horizon. In the NRMS color bar, purple, and blue refer to low NRMS whereas red indicates high NRMS values. 101

4. 4 Gassmann crossplots for water replacing gas calculated for the C1 Sand reservoir. (a) Acoustic impedance versus water saturation. (b) Percent change versus water saturation. Swirr - irreducible water saturation; Srgw - residual gas saturation. 103

4. 5 Simple wedge models for C1 Sand reservoir under (a) Preproduction or baseline conditions and (b) Water-swept monitor condition. The reservoir properties for both conditions are written figures a) and b). Green and blue wedges indicate gas-filled and water swept of the C1 Sand reservoir respectively. Zero-offset synthetics using zero-phase 38 Hz Ricker wavelet for baseline (c), monitor (d) and difference (e). Zero-offset quadrature phase difference synthetics (f). The orange lines in the synthetics are the top and base of the wedge model, converted in two-way time. The difference synthetics are magnified by a factor of 3.7..... 105

4. 6 Qualitative Interpretation of 4D Maui data. Vertical sections extracted from (a) zero-phase baseline, (b) zero-phase monitor, (c) quadrature difference, (d) time-shifts volumes. (e) reservoir-interval root mean square (RMS) extracted from amplitude difference volume shows the water sweep (cyan to orange colors) in Maui field. Contour lines indicate time structure map of the top of the C1U Sand reservoir. Yellow line in e) shows the location of the vertical sections

(a to d). The black line in c) and the deviated black line in e) represents the location of MB-12 production well penetrated the C1 Sand reservoir. The deviated lines in e) display the production wells that were producing from the C1U between 1991 and 2002. White polygons in Maui A and Maui B regions show the gap zones underneath the production platforms. FW - flank water override; GWC - gas-water contact. The time shifts vary from -1 ms to +1 ms. In the RMS difference color bar, purple refers to low RMS difference values whereas yellow, and orange indicate high RMS difference (i.e., impedance hardening). 107

4. 7 MB-12 C1 Sand reservoir TDT/RST history. Saturation plot colours are: Gas - Green, Oil - Red, Water - Blue. TDT - Thermal decay tool; RST - Reservoir saturation tool. The log tracks from left to right are Gamma-ray (GR), Density (DENS), Neutron (NEU), Resistivity (RESD, RESM, RESS), Porosity (PHI), Permeability (PERM), Hydrocarbon saturation (HC) computed from original 1993 logs, Hydrocarbon saturation calculated from 1999 TDT, 2001 RST and 2003 RST logs (modified from Pannett et al., 2004, used by permission). 108

4. 8 Production history analysis of three of Maui wells. Production profile of (a) C1U Sand reservoir penetrated by MB-09 well at Maui B region, (b) C1L Sand reservoir penetrated by MB-12 at Maui B region and (c) C1 Sand reservoir at MA-05 well at Maui A region. (d) Well time lines of the three wells that summarizes the activities of the wells with respect to the timing of acquiring the baseline and monitor seismic data. 109

4. 9 Quadrature phase difference calculated the from broadband 4D difference amplitude (a), the difference calculated from the baseline and monitor spectral voices volumes (b, c, e and f) and 38 Hz quadrature difference (d) calculated from the broadband difference amplitude a). (g) Reservoir-interval RMS amplitude map of the C1U calculated from the 38 Hz spectral voice difference of the monitor and baseline d). Orange arrow shows the 4D changes at the C1 Sand reservoir. The deviated lines show the production wells produced from the C1U sand reservoir

between 1991 and 2002. MNTR - monitor; MBSE - baseline. White polygons in Maui A and Maui B regions show the gap zones underneath the production platforms. 112

4. 10 Reservoir-interval slices extracted from broadband instantaneous attributes (a to f) and 38 Hz spectral instantaneous attributes (g to l) for the C1U Sand reservoir. White polygons indicate data gap zones underneath the Maui A and Maui B regions. Orange arrow indicate areas with reduced amplitude observed in the monitor slices that might have been caused by water replaced gas due to production from C1U between 1991 and 2002. Yellow, white and cyan arrows refer to enhancements in illuminating detailed sandy facies in the spectral instantaneous slices compared to those attributes calculated on the broadband data. Pink arrows refer to reservoir facies that is better imaged on the monitor data compared to baseline data. RAI - Relative acoustic impedance. 114

4. 11 Attribute selection and SOM cluster analysis workflow implemented to integrate data from eight 4D spectral instantaneous attributes for reservoir monitoring studies. PSDM – pre-stack depth migrated seismic; PCA - principal component analysis; SOM - self-organizing map. 118

4. 12 Well section display of three vertical Maui wells show wireline logs, petrophysical logs, flow units and SOM classifications extracted from the baseline and monitor SOM classification volumes at the well locations. TVD – True vertical depth; GR - Gamma-ray; NEU - Neutron; RD - Deep resistivity; PHIT - Total porosity; SH - Hydrocarbon saturation; Pay - Net pay; Res - Net reservoir; NR - Non-reservoir; FU - flow units; SOM - self-organizing map; SB - SOM baseline; SM - SOM monitor. The numbers in FU track shows the flow unit numbers defined in Chapter 3 whereas the numbers in SB and SM tracks indicate the neurons numbers of the SOM classification volume. The flow units colored in yellow and orange indicate high speed and normal reservoir flow units whereas the ones colored in cyan indicate baffles. 120

4. 13 Vertical sections extracted from SOM classification co-rendered with the quadrature phase components of (a) baseline and (b) monitor volumes and cross Maui-7 well, which display net

pay and net reservoir discrete log. The red and black circles indicate SOM clusters of C1U and C1L that are correlated to gas-charged sand reservoir at the Maui-7 well. Orange circles in SOM legend indicate C1U to the east of Maui-7 well. The white bar in 2b) shows the Maui-7 well location. OHWC – approximate original hydrocarbon water contact. The OHWC is drawn as a flat line but in reality it is likely not be a flat in TWT. The inset slice is RMS amplitude map for the C1U reservoir extracted from the difference amplitude volume. 124

4. 14 3D view of SOM clusters for the upper C1U Sand reservoir (C1U). (a) All SOM clusters are turned on. SOM clusters correlated to gas-charged flow units at Maui-7 well. (b) Neuron N32 correlated to poor quality reservoir within baffle (FU1), (c) N61 correlated to poor quality reservoir within baffle (FU5) and (d) N40 correlated to reservoir flow unit. Red, cyan and yellow arrows show changes in the cluster patterns (smaller pattern observed in the monitor SOM compared to the baseline) that might indicate swept areas of the reservoir. Orange arrow indicates slightly larger reservoir cluster in the monitor SOM compared to the baseline SOM slice. The light gray gaps in the baseline and monitor volumes in a) show exclusion areas underneath the Maui A and Maui B production platforms. The deviated lines shows the production wells that were producing mainly gas from the C1U Sand reservoir between 1991 and 2002 whereas the vertical line in Maui B region shows Maui-7 well..... 126

4. 15 3D view of SOM clusters for the upper C1U Sand reservoir (C1U) with gas-charged reservoir penetrated by Maui-7 well clusters turned on. (a) N48 correlates to high speed and normal reservoir flow units. Gas-charged SOM clusters penetrated by (b) Maui-7 and MA-09B wells and (c) Maui-7, MA-02A and MA-09B. (d) SOM clusters shown in c) and clusters N57 and N55 that displays smaller patterns across Maui A south in the monitor SOM compared to the baseline SOM. The vertical line in Maui B region shows Maui-7 well whereas the deviated lines plotted in Maui A and Maui B regions shows the production wells from the C1U Sand reservoir. All the production wells were producing between 1991 and 2002 except MA-02A and MA-09B

wells, which penetrated the C1U Sand reservoir in the Maui A west in 2008 and 2015, respectively. Pink arrows shows slightly larger reservoir portions clustered by SOM that agrees with the attribute slices displayed in Figure 4.8. Cyan arrow shows MA-09B well penetrated Maui-7 gas-charged sand SOM clusters. 127

4. 16 Vertical sections extracted from SOM classification co-rendered with the quadrature phase components of (a) baseline and (b) monitor volumes. These sections cross the MA-09B, MA-02A and Maui-3 wells, which display net pay and net reservoir discrete logs. Black and white deviated lines in the RMS map indicate the MA-09B and MA-02A well paths. Orange and red circles indicate gas-charged sand reservoir penetrated by MA-09B and MA-02A wells, respectively. Cyan circles refer to the C1U Sand reservoir penetrated by Maui-3 well. The gray bars to the left of a) and b) show the location of MA-09B. No well logs are available for MA-09B. OHWC – approximate original hydrocarbon water contact. The OHWC is drawn as a flat line but in reality it is likely not be a flat in TWT. The inset slice is RMS amplitude map for the C1U reservoir extracted from the difference amplitude volume. 130

4. 17 Vertical sections extracted from SOM classification co-rendered with the quadrature phase of (a) base-line and (b) monitor volumes. These sections cross the MB-12 well, which display net pay and net reservoir discrete logs. HWC - hydrocarbon water contact; C1U and C1L - Upper and Lower C1 Sand reservoir. The orange and black circles in the SOM cluster legend (inset) indicate clusters correlate to the C1U and C1L reservoir. The white bar in 2b) shows MB-12 location. OHWC – approximate original hydrocarbon water contact. The OHWC is drawn as a flat line but in reality it is likely not be a flat in TWT. The inset slice is the RMS amplitude for the C1L reservoir extracted from the difference amplitude volume. 133

4. 18 3D view of SOM classification for the lower C1 Sand reservoir (C1L). (a) All SOM clusters are turned on. (b) SOM clusters correlated to gas-charged sand at Maui-7 and MB-12. Orange and cyan arrows refer to SOM clusters disappeared or cover smaller area in the monitor SOM

compared to the baseline SOM. Yellow arrow denote SOM clusters that cover larger area in the monitor compared to the baseline SOM slice. 134

4. 19 3D view of geobodies extracted for the C1U Sand reservoir from the baseline (left) and monitor (right) SOM classification volumes. The red arrows refer to water swept areas of the reservoir. The monitor geobodies cover smaller areas and may suggest the undrained parts of the C1U reservoir. The deviated lines indicate the production wells that were producing from the C1U sand reservoir. Vertical line (yellow arrow) refers to Maui-7 well. (c) 3D view of geobodies extracted for the C1U Sand reservoir from the quadrature component volume. 137

A. 1 Amplitude spectrum of 2006 processed merged seismic volume around the reservoir interval; 2000-2500 ms. 165

A. 2 PC SOF workflow (modified from Marfurt, 2018) 166

A. 3 Vertical seismic lines extracted from a) original seismic amplitude, b) seismic data after applying 1st iteration of principal component structure-oriented filter (PC-SOF), c) seismic data after 2nd iteration of PC-SOF, d) rejected noise after 1st iteration of PC-SOF and rejected noise after 2nd iteration of PC-SOF. 167

LIST OF ACRONYMS

AF	Alpine fault
BCF	Billion cubic feet
BS	Bit size
C1L	Lower C1 Sand reservoir
C1U	Upper C1 Sand reservoir
CALI	Caliber
CEF	Cape Egmont fault
CKair	Core permeability
CNN	Convolutional neural network
CPHI	Core porosity
CWT	Continuous wavelet transform
DENS	Density
DENSg	Gas density
DENSgrain	Grain density
DENSo	Oil density
DENSw	Water density
DNNA	Democratic neural network association
e_pos_long	Long wavelength amplitude curvature
FU	Flow units
FZI	Flow zone indicator
GLCM	Gray-level co-occurrence matrix (GLCM)
GOR	Gas-oil-ratio
GR	Gamma ray
IF	Ihi fault
K/PHI	Reservoir process speed
K_pred	Predicted permeability
K1	Most positive principal curvature
K2	Most negative principal curvature
K_{air}	Air permeability
Ke	Euler curvature
Kg	Gas bulk modulus

Kgrain	Grain bulk modulus
KH	Flow capacity
Krot	Reflector rotation
Kw	Water bulk modulus
MLP	Modified Lorenz plot
MPA	Maui A platform
MPB	Maui B platform
N	Neuron
N/G	Net pay-to-gross
Net Res/Gross	Net reservoir-to-gross
NO_RES	Non-reservoir
NRMS	Normalized root mean square
P	Pressure
PCA	Principal component analysis
PC-SOF	Principal component structure-oriented filtering
PF	Pungawerewere fault
PHI	Porosity
PHIE	Effective porosity
PHIH	Storage capacity
PSDM	Pre-stack depth migrated
R_{35}	Pore-throat radius (micron) at 35 % mercury saturation
RAI	Relative acoustic impedance
RES	Net reservoir
RESD, RESS	Resistivity logs
RG02	Recoverable gas estimated from the monitor (2002) geobodies
RG91	Recoverable gas estimated from the baseline (1991) geobodies
RGB	Red-green-blue
RMS	Root mean square
RQI	Rock quality index
SFP	Stratigraphic flow profile
SMLP	Stratigraphic modified Lorenz plot
SOM	Self-organizing maps
Srgw	Residual gas saturation

SW	Water saturation
T	Temperature
TWT	Two-way time
Vint	Interval velocity
Vp	Compressional wave velocity
Vs	Shear wave velocity
VSH	Shale volume
WF	Whitiki fault
ϕ_{CORE}	Core permeability

1 Introduction

1.1 Overview

Over the last few decades, there has been a wide interest in the application of machine learning to different geoscience disciplines. Supervised machine learning techniques are applied to well logs and seismic data for lithofacies classification (Baldwin et al., 1990; Dubois et al., 2007; Hami-Eddine et al., 2009, 2015; Hall, 2016) and reservoir properties predication (Hampson et al., 2001; Russell et al., 2003; Mohamed et al., 2014, 2019). Unsupervised and semi-supervised machine learning methods are applied to seismic data for facies classification (Matos et al., 2006, 2011; Roy, 2013; Roden et al., 2015; Zhao et al., 2015). More recently, deep neural networks are used for seismic facies classification (Zhao, 2018), impedance inversion (Das et al., 2018; Kim and Nakata, 2018; Russell, 2019) and fault detection (Wu et al., 2019; Zhao, 2019). Machine learning methods are applied to 4D seismic data to predict reservoir property changes (Cao and Roy, 2017; Xue et al., 2019). In this dissertation, I focus on the application of unsupervised machine learning to resolve some challenges related to reservoir characterization analysis and time-lapse seismic studies.

Reservoir characterization analysis depends on building and updating reservoir models through integration of all available data during different stages of a field lifecycle. Initially, a static 3D reservoir model is built by incorporating core, well logs and seismic data, usually by using geostatistical and/or stochastic methods (Doyen, 2007). This model is composed of the structural framework (horizons and faults) and physical properties (facies, porosity and permeability). However, accurate representation of the reservoir geometry, which includes structural framework and stratigraphic details remain a key challenge (Branets et al., 2008).

Small-throw faults, which I call subtle faults in this dissertation, can be easily overlooked in interpreting seismic amplitude data, and thus be missing in the 3D static model. Subtle faults can act as baffles or conduits that significantly control how a petroleum reservoir is swept. Seismic attributes aid in illuminating small faults, however, over the last decades, , many seismic attributes have been developed for fault interpretation but it has been challenging for interpreters to know which work best. Thus, selecting the best attribute to be used for subtle fault detection remains an open question.

Net reservoir delineation and rock type identification help to understand the reservoir quality, distribution and to identify stratigraphic baffles. At the well location, a geoscientist usually performs petrophysical and rock type analyses to define net reservoir intervals and understand the reservoir quality and heterogeneity (Guo et al., 2007). Extending this reservoir facies away from the well control is critical for building a reliable static model (Hami-Eddine and Furniss, 2011). Pre-stack seismic and stochastic inversion approaches uses the 2D or 3D inverted seismic data to define different geologic facies (Doyen, 2007; Avseth et al., 2010). Democratic neural networks can be applied to pre-stack seismic data to obtain geologic facies with uncertainty estimates away from well control (Hami-Eddine et al., 2009). Although, these methods are useful for lithological predications and associated fluid content through-out the field, they require good-quality angle-stack seismic volumes and large number of wells which might not be available in the initial exploration phases in some fields.

During the field production phase, dynamic data such as production and time-lapse (4D) seismic data are acquired to monitor fluid movements due to production. The 4D seismic data can be used to monitor reservoir property (water saturation and/or pressure) changes associated with production-related changes.

The 4D seismic data is usually used to constrain the reservoir flow simulation models through the 4D close-the-loop process (Gouveia et al., 2004; MacBeth et al., 2006). The flow simulation models use upscaled reservoir properties derived from the static reservoir model (Doyen, 2007). Thus, the simulation cannot capture detailed reservoir heterogeneity, which resulted in a mismatch between the synthetic seismic response and the actual 4D seismic data (Sengupta et al., 2003; Helgerud et al., 2011).

Similar to the 3D seismic data, the 4D data suffer from seismic interference and tuning effects (Johnston, 2013). Although, probabilistic inversion can be applied on 4D seismic data to quantify the dynamic reservoir properties' changes due to production (Buland and El Ouair, 2006; Kleemeyer et al., 2012; Xue, 2013). Bayesian inversion approaches may not be able to differentiate between shale and thin bedded sand-shale sequence due to the seismic resolution limitations. These thin sands usually do not have significant contribution to production however, incorporating those facies in the flow simulation models improves the synthetic seismic to actual 4D seismic mismatch and reduces the turn-around time (Nasser et al., 2017).

In this dissertation, I discuss various seismic attributes that aid in illuminating small faults and subtle changes in reservoir properties. I develop different machine learning workflows that enable seismic interpreters to better understand the reservoir characteristics, fluid movements and deal with the above-mentioned challenges. The main contributions of this research are:

1. I investigate typical horizon-based and geometric attributes that are sensitive to small faults and fractures and develop a workflow to select the best attributes for human interpreters and machine learning analysis. I then integrate the structural information from multiple geometric attributes by using multi-attribute displays and an unsupervised machine learning technique – Self-organizing maps (SOM).
2. I investigate typical seismic attributes that are sensitive to lithological changes and reservoir properties variations. I propose a machine learning workflow that enables us to combine geological information within eight spectral instantaneous attributes into one classification volume. This clustered volume highlights the reservoir distribution and illuminates thin stratigraphic baffles.
3. I investigate various full-stack 4D seismic attribute volumes and propose a workflow to select the best attributes that show 4D changes related to production effects. I then combine the reservoir information from eight 4D spectral instantaneous seismic attributes into clustered volumes, which show the reservoir heterogeneities with their associated 4D changes.

1.2 Dissertation outline

This dissertation consists of 6 chapters. Chapter 1 discusses my motivations for this research and provides an overview for the thesis.

In Chapter 2, I use a dataset from the Maui field, Offshore Taranaki basin of New Zealand to generate typical seismic attributes that are sensitive to faults and fractures. I analyze the individual seismic attributes and discuss the pros and cons of each attribute. I propose a workflow that enables seismic interpreters to select the best attributes for visual and machine learning analyses. I integrate the geological information from different attributes by using multi-attribute display and machine learning – the SOM method. I provide eight combinations of seismic attributes that could be useful by a human interpreter for fault interpretation. I then propose a machine learning workflow to integrate structural information of carefully selected six geometric attributes into one classification volume, which shows subtle faults affecting the field.

In Chapter 3, I focus on the C1 Sand reservoir of Maui field. I perform petrophysical and rock typing analyses to evaluate reservoir properties, define net reservoir intervals, understand the reservoir quality and divide the C1 Sand reservoir into different flow units. I generate the typical instantaneous and spectral decomposition seismic attributes for the C1 Sand reservoir. I find that the spectral instantaneous attributes provide better stratigraphic details compared to attributes derived from the broadband seismic data. I use visual analysis and principal component analysis (PCA) to carefully select seismic attributes to be used as input to SOM analysis. I propose a workflow to combine the geological information within eight spectral instantaneous attributes into one classification volume. Calibrating SOM clusters to net reservoir and flow units discrete logs enables us to discriminate net reservoir facies, understand reservoir quality and heterogeneity and define thin stratigraphic baffles across the whole field.

In Chapter 4, I use the 4D dataset of Maui field that includes baseline and monitor full-stack seismic volumes along with wells that penetrate the C1 Sand reservoir and lie within the 3D surveys. I start this chapter with a rock physics analysis and 4D modeling to understand the expected changes in the seismic amplitude and time-thickness as a result of water replacing gas as the reservoir is being swept under a strong water drive. I discuss the conventional interpretation of 4D seismic data. I generate typical instantaneous and spectral decomposition seismic attributes on the individual baseline and monitor 4D seismic volumes to investigate the sensitivity of full-stack attributes to 4D changes.

I propose a systematic machine learning workflow to carefully select eight 4D spectral instantaneous attributes, which show 4D changes at the reservoir level. I then integrate the preproduction and postproduction reservoir information of the baseline and monitor volumes into classification volumes. I correlate these clustered baseline and monitor volumes to well data, production data and 4D volumes to understand reservoir heterogeneity and illuminate water saturation changes within thin good and poor quality reservoirs, which are difficult to be imaged by the original 4D seismic volumes. I generate geobodies for meaningful clusters obtained for the baseline and monitor classification volumes. I calculate recoverable gas reserves for the baseline and monitor geobodies and then compare the result to production data. I then discuss uncertainities in this comparison that cannot be fully addressed by this dataset.

Chapter 5 is a summary of Chapters 2-4 and Chapter 6 discusses potential future research directions.

2 Which seismic attributes are best for subtle fault detection?

2.1 Summary

Subtle fault detection plays a vital role in reservoir development studies because faults may form baffles or conduits that significantly control how a petroleum reservoir is swept. Small-throw faults are often overlooked in interpreting seismic amplitude data. However, seismic attributes can aid in mapping small faults. Indeed, over the years, dozens of seismic attributes have been developed that offer additional features for interpreters with associated caveats. Using the Maui 3D seismic data acquired in the Offshore Taranaki Basin, New Zealand, I generate seismic attributes that are typically useful for fault detection. I find that multi-attribute analysis provides greater geological information than would be obtained by the analysis of individual attribute volumes. I extract the geological content of multiple attributes in two ways: interactive co-rendering of different seismic attributes and the unsupervised machine learning algorithm self-organizing maps (SOM). Co-rendering seismic attributes that are mathematically independent but geologically interrelated provides a well-integrated structural image. I suggest eight combinations of sixteen various attributes that are useful for a human interpreter with interests in fault and fracture detection. However, current interpretation display capabilities constrain co-rendering to no more than four attributes volumes.

Therefore, I use principal component analysis (PCA) and SOM techniques to efficiently integrate the geological information contained within many attributes. This approach gathers the data into one classification volume based on interrelationships between seismic attributes. The resulting SOM classification volume better highlights small faults that are difficult to image using conventional seismic interpretation techniques. I find SOM work best when a fault exhibits anomalous features for multiple attributes within the same voxel. On the other hand, human interpreters are more adept at recognizing spatial patterns within various attributes and can place them in an appropriate geologic context.

2.2 Introduction

Imaging of subtle faults plays a crucial role in reservoir characterization and reservoir modeling. Faults with small offsets (i.e., that produce subtle breaks in reflectors or even below the seismic tuning thickness), herein referred to as 'small faults', are important for identifying hydrocarbon migration pathways and bypassed oil accumulations, and can be overlooked in the conventional interpretation of seismic amplitude data (Al-Dossary and Marfurt, 2006; Li and Lu, 2014). Over the last few decades, geoscientists have devoted great efforts to develop seismic attributes to better map faults. The most prominent example is the development of coherence algorithms that quantify the lateral change in the seismic waveform, and/or amplitude (Bahorich and Farmer, 1995; Luo et al., 1996; Gersztenkorn and Marfurt, 1999; Randen et al., 2000) . However, coherence attributes show anomalies only if there are clear offsets of the seismic reflectors. This can result in segmented coherence anomalies if the reflectors' offsets are below the seismic resolution (Mai et al., 2009; Libak et al., 2017).

Partyka et al. (1999) and Henderson et al. (2008) emphasized that the spectral phase component and red-green-blue (RGB) blending of spectral magnitudes aid in detecting faults. Taking advantage of spectral decomposition analysis in enhancing the coherence image, Li and Lu (2014) and Honório et al. (2017) developed multispectral similarity methods that include the calculation of coherence for various spectral components which are then co-rendered to produce different spectral coherence images. Alternatively, a multispectral coherence volume can be computed by constructing a multispectral covariance matrix along structure dip calculated from the spectral voices (Marfurt, 2017; Li et al., 2018). Chopra and Marfurt (2019) extended the multispectral coherence concept to multi-offset and multi-azimuth coherence analysis, which showed superior results.

Despite these efforts, it is remains challenging to use coherence attributes to detect small faults and fractures that are offset below the seismic resolution (Gao, 2013). More advanced geometric attributes have been developed to quantify the lateral variation of seismic reflector geometry such as dip, curvature and aberrancy attributes, which aid in illuminating small faults and fractures (Roberts, 2001; Al-Dossary and Marfurt, 2006; Di and Gao, 2016; Qi and Marfurt, 2018) . The gray-level co-occurrence matrix (GLCM) is a popular texture attribute that measures how often various combinations of amplitude sample values occur within an analysis window (Gao, 2011; Matos et al., 2011) . For the human interpreter, GLCM attributes provide less useful images compared to other geometric attributes, which provide clear and easily understood geomorphic features such as channel edges, faults and folds. However, these texture attributes tend to work well for supervised and unsupervised classification machine learning algorithms (Marfurt, 2018).

With continuous advancements in computer capabilities and graphics, many computer-aided fault detection algorithms have been developed to enhance fault edges and interpret faults. For instance, Pedersen et al. (2002, 2003) introduced the application of the ant-tracking algorithm to variance volumes in order to enhance and sharpen fault edges. Barnes (2006) developed a discontinuity filter to enhance the steeply dipping discontinuities associated with faults and cancel all other discontinuities. Aqrawi and Boe (2011) compared application of the ant-colony optimization algorithm on variance and Sobel filter volumes. They found that the Sobel filter showed better results compared to the variance attribute. However, the ant-colony optimization is highly sensitive to noise. Dewett and Henza (2016) used a swarm intelligence algorithm for lineament connection and interpolation between discontinuous events within multiple frequency-based attributes and integrated the results by using normalization, addition and rescaling in addition to the SOM technique. They concluded that SOM has the ability to retain some information of the original frequency volumes. Laudon et al. (2019) presented a case study on the application of SOM to four geometric attributes in order to detect faults and fractures within the main reservoir intervals of the Denver-Julesburg Basin. They selected most positive curvature, energy ratio similarity, GLCM entropy and GLCM homogeneity based on a PCA analysis applied to various geometric attributes (Laudon et al., 2019).

In another approach, pattern recognition convolutional neural networks (CNN) are trained on synthetic seismic data and applied to seismic datasets for fault detection (Pochet et al., 2019; Wu et al., 2019; Zhao, 2019). The synthetic data generation include faults with random dip azimuth, dip magnitude, displacement along dip in addition to a certain degree of normal fault drags. Although the CNN showed sharp fault edges, it failed to detect extremely small-angle faults (Zhao, 2019). A limitation of Wu et al. (2019) CNN workflow is that the

synthetic data didn't include low-angle faults. Thus, the trained CNN may fail to detect thrust or listric faults. Also, when the CNN-trained model is applied to unfamiliar data with slightly different characteristics compared to the training data, the accuracy of the prediction drops dramatically (Lowell and Erdogan, 2019).

Laudon et al. (2019) showed that a less tedious and more efficient way to detect small faults is to incorporate multiple seismic attributes in a machine learning technique instead of using a single seismic amplitude volume. However, selection of the most suitable attributes to be used as inputs to machine learning algorithms is an open question and may highly controls the results.

In this study, I investigate most of the available seismic attributes for fault interpretation starting from simple high spatial resolution maps (e.g., horizon-based attributes) and moving to more advanced geometric seismic attributes such as dip, coherence, amplitude gradients, curvature, amplitude curvature, aberrancy and gray-level co-occurrence matrix (GLCM) attributes. I use a 3D seismic dataset from the Maui field in Offshore Taranaki Basin, New Zealand. I investigate the various seismic attribute volumes generated for the C Sand reservoir of the Maui field and discuss the most useful attributes that can be used qualitatively by a human interpreter and quantitatively by PCA and SOM techniques. I integrate the geological information derived from multiple seismic attributes using a multi-attribute display, and PCA and SOM techniques and compare the results to a previous study (Laudon et al., 2019). I suggest a workflow that enables interpreters to apply PCA and SOM on the most appropriate seismic attributes in order to obtain a single classification volume that best shows small faults.

2.3 Geologic Background

The Taranaki basin covers 200,000 km^2 and is considered the largest sedimentary basin and the only hydrocarbon producing basin of New Zealand (Reilly et al., 2016). It is located mostly offshore of New Zealand's west coast (Figure 2.1) (Baur et al., 2010; Strogen et al., 2015). The structural development of the Taranaki basin was highly influenced by Australian-Pacific plate divergence during the Late Cretaceous-Paleocene period. The structural history of the Taranaki basin is complex with various tectonic elements affecting the basin which include rift transform, platform subsidence, passive margin, subduction, convergent transform, volcanic-arc, fold-thrust, and back-arc rift (Haque et al., 2016).

This study focuses on the Maui field, which is one of the largest New Zealand gas fields. OMV New Zealand owns and operates the Maui field, having acquired it from Shell Exploration NZ at the end of 2018. Maui covers around 1000 km^2 and is located 40 km off of the West coast of the North Island at ~100 m water depth (Figure 2.1a) (Pannett et al., 2004) . Based on the latest reserve estimation report released by the Ministry of Business and Innovation & Employment (MBIE) in 2019, the estimated remaining gas reserves of Maui field are 104.4 petajoules (99 bcf) and estimated remaining oil reserves are 4.5 million barrels. The field produces gas from three main sand reservoirs called the Mangahewa, Kaimiro, and Farewell formations of the Kapuni groups (Figure 2.1b).

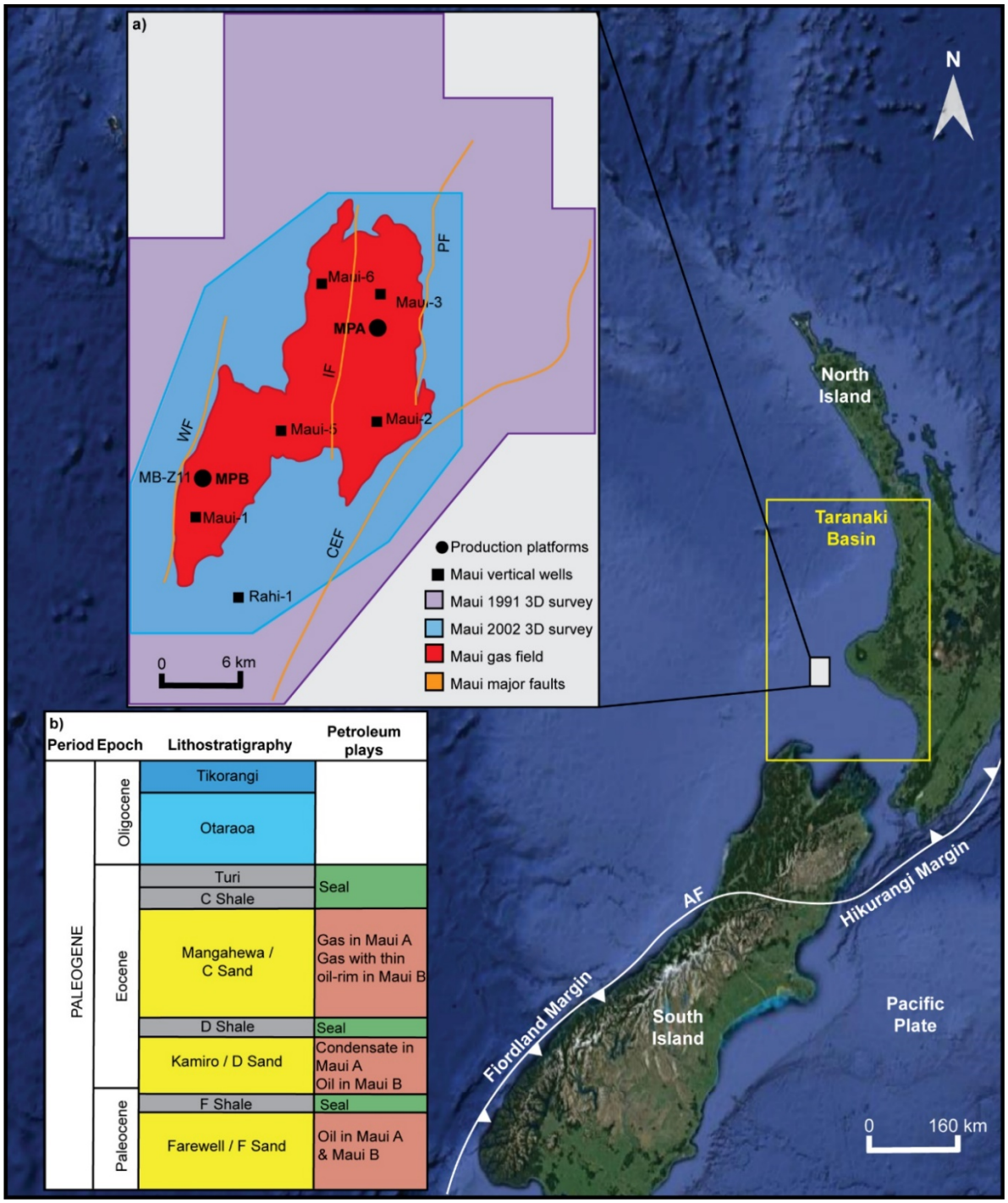

Figure 2. 1. Location map of Taranaki basin, offshore west North Island, New Zealand. (modified from Google Earth). (a) Map of Maui hydrocarbon field, seismic survey coverage and wells (modified from Haque et al., 2016; Baur et al., 2010; Franzel, 2019). CEF – Cape Egmont Fault; WF - Whitiki Fault; PF - Pungawerewere Fault; IF - Ihi Fault; AF - Alpine Fault; MPA & MPB - Maui A and Maui B platforms. (b) Paleogene stratigraphic column of Maui field (modified from Pannett et al., 2004 and Reilly et al., 2016).

In the Maui field, Eocene-age shore-face to marginal marine Mangahewa and Kaimiro reservoirs are named the C Sand and D Sand, respectively, while the Paleocene Farewell sand is named the F Sand. The C Sand reservoir, which is the focus of this research, contains a shallower and larger gas column compared to the D Sand. However, it has very thin oil-rim in the southwestern area of the Maui field. The Upper D Sand reservoir has a smaller gas accumulation. Oil is produced from the Lower D Sand and the F Sand reservoirs in the Maui B region (Pannett et al., 2004) . Figure 2.2a displays well logs and the seismic-to-well tie for one of Maui wells.

The Maui field consists of two gentle anticlinal features; the Maui A region in the northeast and the Maui B region in the southwest (Figures 2.2b) that form a closure of 150 km^2. The field is structurally-complex. The Maui A region is bounded to the east by the Plio-Pleistocene Cape Egmont normal fault (CEF), and the Pungawerewere normal fault (PF). The Maui B region is bounded to the south-west by the Late Miocene Whitiki reverse fault (WF) and is located within a hangingwall anticline caused by inversion of a Cretaceous normal fault (Figures 2.1a, 2.2b, 2.2c and 2.2e) (King and Thrasher, 1996).

Three main tectonic phases affected the Maui field and formed the present-day Maui structure. The Late Cretaceous to Paleocene rifting phase caused by the Australian-Pacific plate divergence formed graben and/or half-graben-like basins (Figure 2.2c) that are controlled by the Whitiki (WF) and Cape Egmont (CEF) faults (Haque et al., 2016). The Late Eocene to Miocene compressive tectonic phase resulted from the subduction of the Pacific plate underneath the Australian plate. The Plio-Pleistocene differentiation phase resulted in extensional forces in Maui North and compressive forces in Maui South (Holt and Stern, 1994; Haque et al., 2016). These later tectonic movements led to the activation of pre-existing structural fabrics and formed new faults. The Maui structural closure commenced in the Late Miocene due to the WF contraction movement and continues to develop at the present-day because of the normal faulting activity (Nodder, 1993; Nicol et al., 2005).

A seismic line extracted from seismic volume over the Maui A region shows the reservoir is mainly influenced by normal faults (Figure 2.2d). These faults have a NE-SW structural trend with a few faults having a NW-SE structural trend. The reservoir layers dip gently (10-15 deg.) dip toward the east and west. A seismic line crossing the Maui B region shows slightly different structural features caused by the influence of structural mechanisms (Figure 2.2e). Although this part of the field is highly affected by the regional reverse fault (WF), a folding mechanism seems to have formed stratigraphic monocline units that have 15 – 20 deg. dip angles to the west. This indicates that the northern part of the field has greater intensity of faulting compared to the southern part of the field. Some listric faults with rollover anticlines have been observed in the central part of the field (Haque et al., 2016).

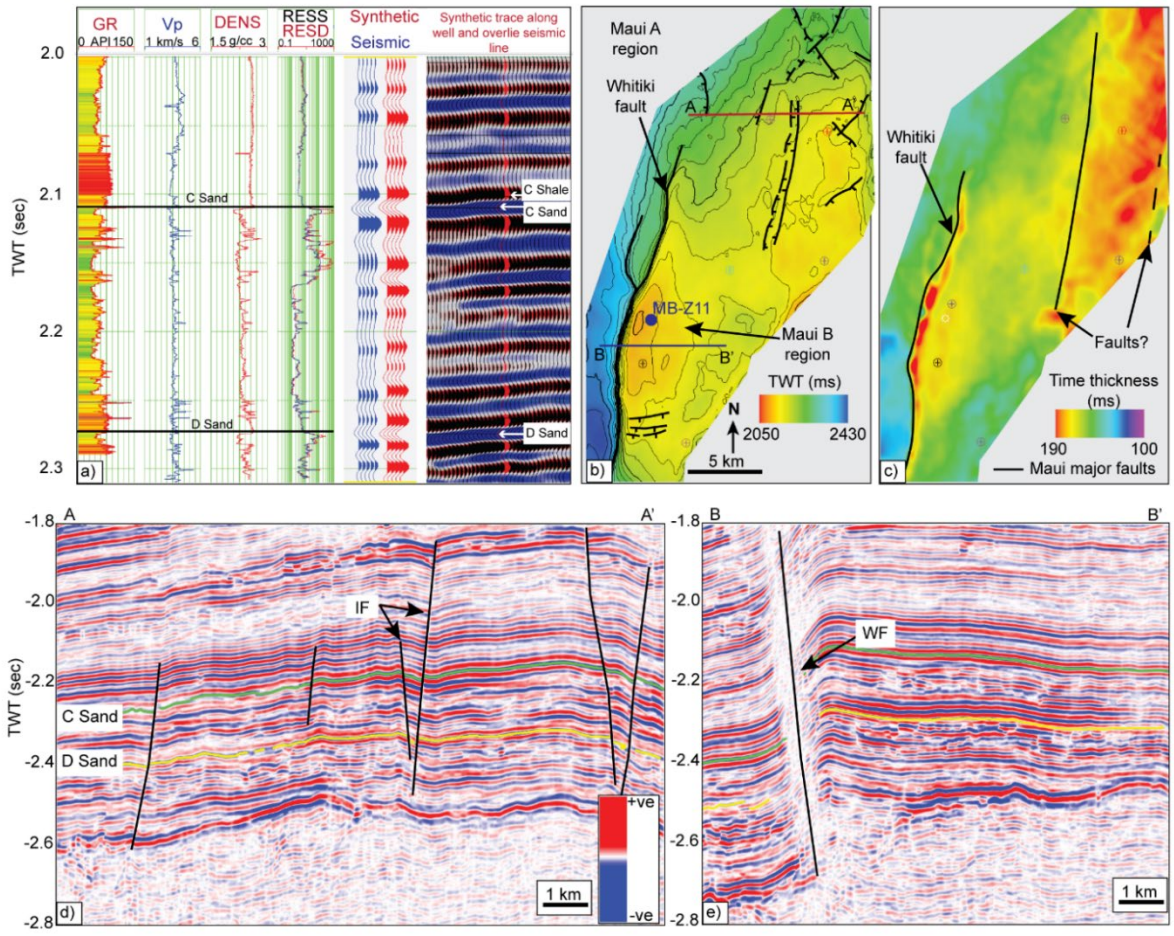

Figure 2. 2. Maui field subsurface geologic context shown by: (a) Seismic-to-well tie for MB-11 well shows the C Shale, C Sand and D Sand seismic events. The tracks from left to right are Gamma ray (GR), Compressional velocity (Vp), Density (DENS) and Resistivity(RESD, RESS) logs, composite seismic trace, zero-phase synthetic seismic trace and seismic trace extracted along the well and overlie seismic line; (b) Time structure map of the top C Sand reservoir showing two anticlinal features separated by a saddle. Circles with crosses show vertical wells that penetrated the interval of interest; (c) C Shale to D Sand isochron map shows the time thickness variation during the deposition of C Shale and C Sand reservoir. It aids in defining the syn-deposition faults affecting the C Sand reservoir and shows a half-graben-like basin structure; (d) A-A' seismic line (location shown by red line in b)) crosses the Maui A region. The area is affected by a set of normal faults that forms graben to half-graben-like structures. IF - Ihi fault; (e) B-B' seismic line (the blue line in b)) across the Maui B region showing the Whitiki fault (WF) bounding the west side of the Maui B anticline.

2.4 Dataset

Two 3D seismic surveys were acquired over the Maui field and made available for research purposes by the MBIE, New Zealand. The first 3D seismic survey was acquired in 1991 and covers 1000 km^2. The second 3D seismic survey, shot in 2002, covers 480 km^2 over just the Maui A and Maui B structures (Figure 2.1a). The 1991 survey was acquired using two vessels in a quad-quad manner with four streamers and two sources. The shot interval was 18.75 m and the receiver group interval was 25 m. The 2002 seismic data was acquired by a single vessel using two sources and six streamers with 18.75 m and 12.5 m shot and receiver group intervals, respectively. In 2006, both surveys were reprocessed and merged by Shell Geoscience Solutions in the Netherlands. The data were combined in the DMO (dip move-out) processing step and were migrated using prestack depth migration (PSDM) (van der Veeken and Lutz, 2008).

In this study, the final PSDM processed merged seismic volume is used for seismic interpretation and seismic attribute analysis. Eight vertical wells (Maui-1, Maui-2, Maui-3, Maui-5, Maui-6, Maui-7, MB-Z11, and Rahi-1) are located within the 3D seismic survey area. Each well has conventional well logs (gamma-ray, density, neutron, sonic) and completion reports. Some core reports and core photos are available for Maui-5, Maui-6 and Maui-7 wells.

2.5 Methodology

Figure 2.3 shows the workflow implemented in this study. The final processed PSDM merged seismic volume covers a total area of 1000 km2 and was recorded to 3.5 s two-way time (TWT) at a 4 ms sample interval. The data were cropped laterally to cover an area of 410 km2, and vertically to cover a time range of 1.8 to 2.8 s two-way time (TWT). I cropped the original seismic volume to a smaller one in order to focus on areas with diverse fault styles within the C Sand reservoir and to reduce computational time and hard drive space. The original seismic data were then resampled to 2 ms to provide more samples for the SOM analysis. The seismic data were spectrally balanced during the 1991 and 2001 seismic volume merge (van der Veeken and Lutz, 2008). However, the data are contaminated by random noise and acquisition artifacts. Thus, I followed Chopra and Marfurt's (2006) approach and applied a well-established principal component structure-oriented filtering (PC-SOF) along structural dip. This method enhances the signal that is aligned with the estimated dip and reduces the noise that crosses in other directions. A detailed description of the seismic data conditioning is available in Appendix A.

The seismic-to-well tie for the MB-11 well shows the C Shale, C Sand and D Sand seismic events (Figure 2.2a). I consider the time structure map, the horizon amplitude extraction and high spatial residual map, which is calculated by subtracting a high-precision manually picked seismic horizon from a smoothed seismic horizon (Brown, 2011), as horizon-based attributes.

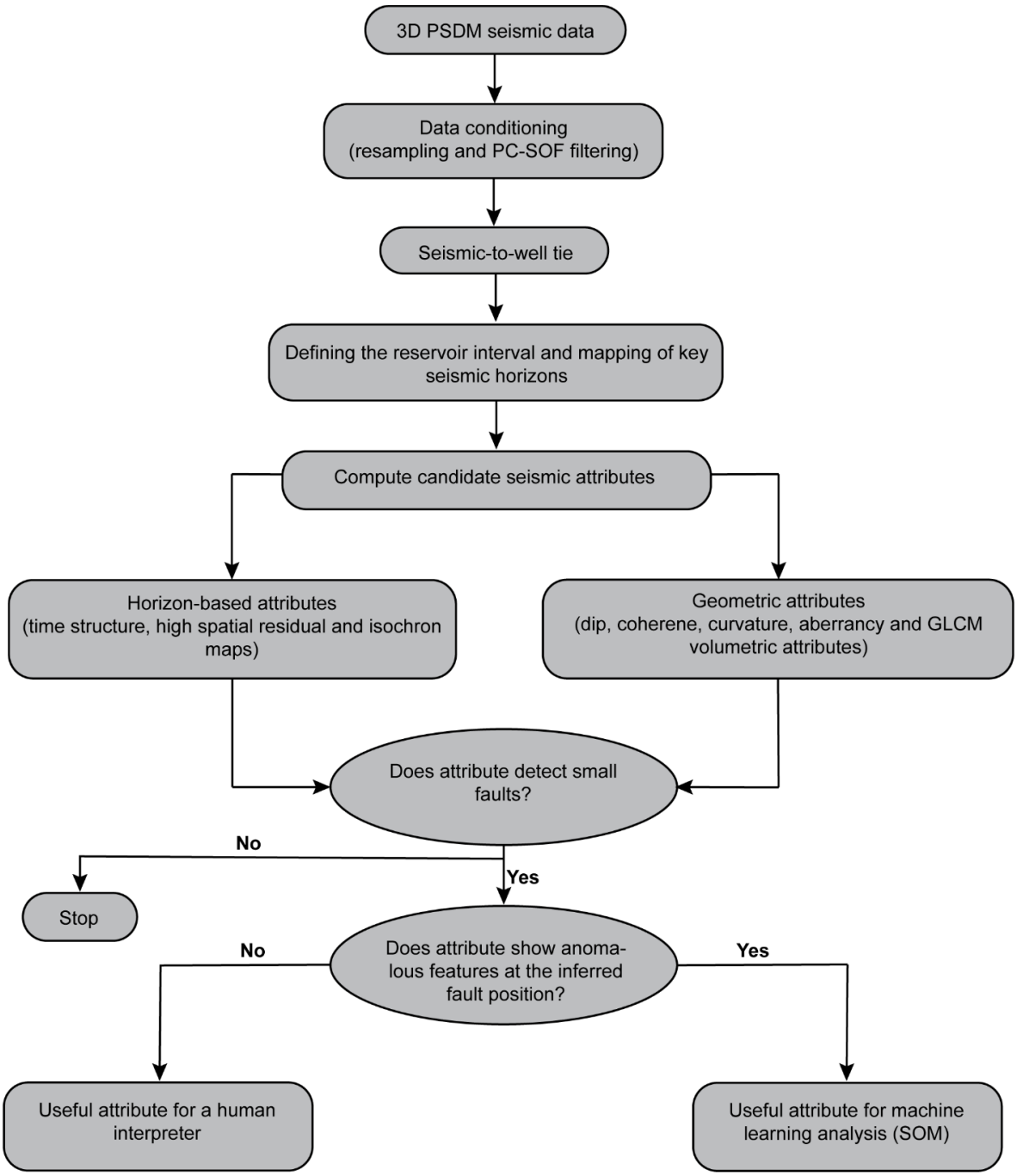

Figure 2. 3. Workflow to select useful attributes for machine learning analysis and a human interpreter. PSDM - prestack depth migrated; PC-SOF - principal component structure-oriented filtering; GLCM - gray-level co-occurrence matrices; SOM – self-organizing map; PCA - principal component analysis.

I calculated thirty typical geometric attributes available to a seismic interpreter that include volumetric dip, coherence, amplitude gradients, curvature, curvedness, shape index, reflector rotation, Euler curvature, aberrancy, and Gray-level co-occurrence matrices (GLCM) attributes. The mathematical background of all the attributes generated in this chapter are available in appendix B. I then use a workflow to analyze and to select the ones that are most useful for a human interpreter and those that work best for SOM analysis (Figure 2.3).

2.6 Seismic attribute analysis

I begin by analyzing thirty widely-used horizon-based and geometric attributes for fault delineation (Figure 2.4). The goal of this analysis was to compare relative strengths, weaknesses, and redundancies of the individual analyses to inform our later multiattribute analyses. The high spatial residual map and amplitude extraction (Figures 2.4a and 2.4b) along the C Sand reservoir show the Whitiki fault on the west side of the Maui B region. Some of the faults have clear seismic offsets (white arrows) but in some areas the attributes seem to be sensitive to noise (red arrow).

I evaluated the other twenty-eight geometric attributes by using horizon slices extracted along the top of the C Sand reservoir. The inline dip, crossline dip and dip magnitude attributes (Figures 2.4c, 2.4d and 2.4e) show similar edges. Thus, the dip magnitude can be used as an edge detection attribute and the inline and crossline dips can be used to generate other attributes such as coherence and curvature.

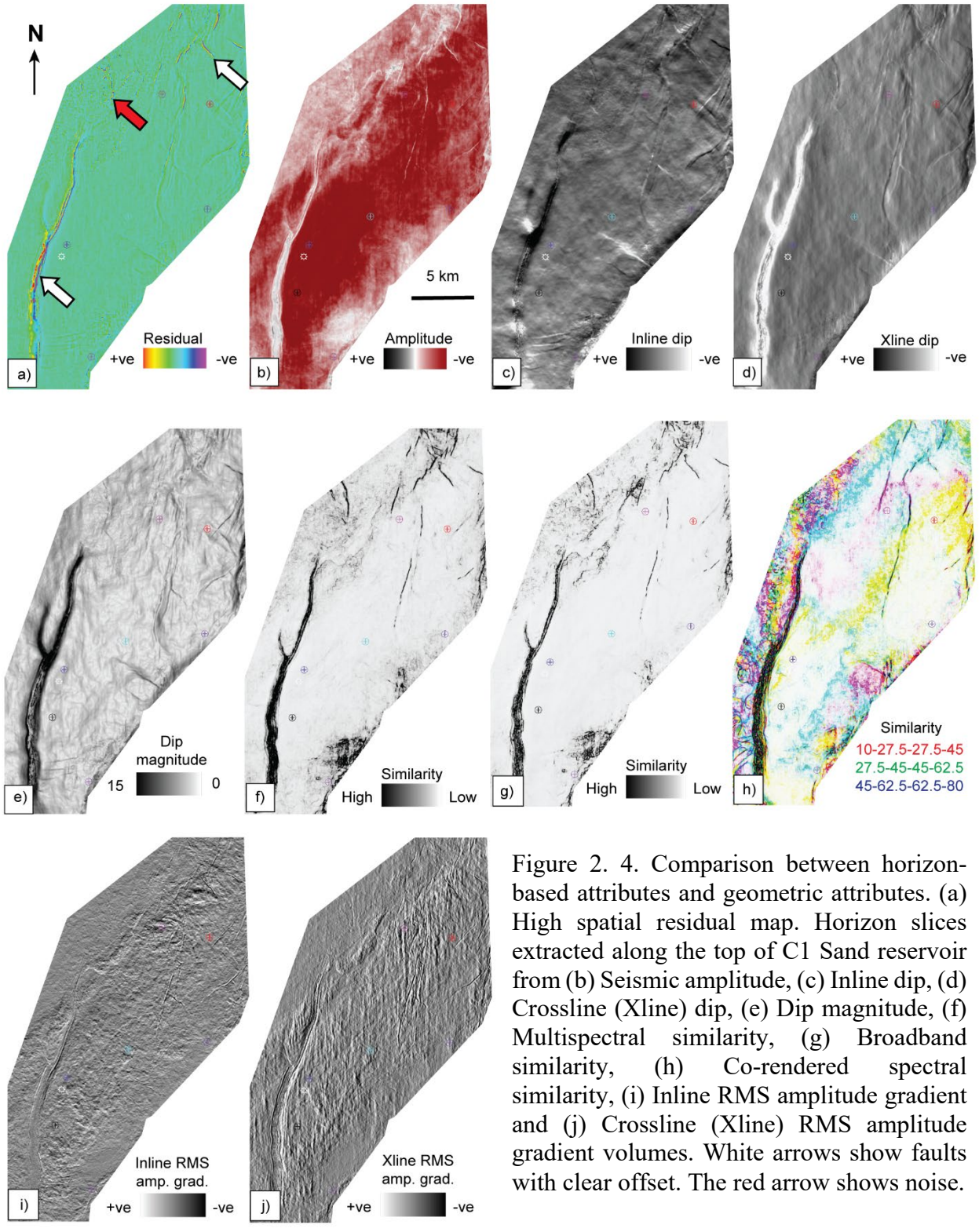

Figure 2. 4. Comparison between horizon-based attributes and geometric attributes. (a) High spatial residual map. Horizon slices extracted along the top of C1 Sand reservoir from (b) Seismic amplitude, (c) Inline dip, (d) Crossline (Xline) dip, (e) Dip magnitude, (f) Multispectral similarity, (g) Broadband similarity, (h) Co-rendered spectral similarity, (i) Inline RMS amplitude gradient and (j) Crossline (Xline) RMS amplitude gradient volumes. White arrows show faults with clear offset. The red arrow shows noise.

The multispectral energy ratio similarity (Figure 2.4f) shows a cleaner image and sharper edges associated with the small faults in the central and northern parts of the Maui field compared to the broadband (Figure 2.4g) and co-rendered spectral energy ratio similarity (Figure 2.4h) images. On the other hand, the broadband energy ratio similarity and the co-rendered spectral energy ratio attributes clearly show the fault terminations of the WF zone where the multispectral energy ratio similarity image is blurred. Inline and crossline RMS amplitude gradients (Figures 2.4i and 2.4j) show similar edges. However, the crossline RMS amplitude gradient is highly affected by acquisition artifacts associated with the north-south shooting orientation. As a result, these attributes do not provide additional geological information compared to other attributes.

The long- and short-wavelength most positive and most negative principal curvature attributes are useful for mapping faults at Maui (Figures 2.5a, 2.5b and 2.5c). However, the most negative principal curvature attributes show better lineaments compared to those imaged by the most positive principal curvature. The amplitude curvature (Figure 2.5d) shows acquisition artifacts that mask the geology. These N-S trending artifacts might have been resulted from the differences in the acquisition geometries between the 1991 and 2002 seismic surveys. As a result, this attribute was not as useful for fault detection in this study, however, it can be used to check the seismic data quality.

The most positive and most negative principal curvatures were combined to calculate the curvedness attribute (which describes the total deformation of a seismic event) and the shape index (which describes the shape of the seismic reflector) (Figures 2.5e and 2.5f). Reflector rotation (Figure 2.5g) is one of the curvature attributes that shows the rotation of the faulted blocks at the faults' tips. Euler curvature attributes (Figures 2.5h and 2.5j) show similar fault trends as seen in other attributes; thus, I consider these attributes redundant in this study.

The total aberrancy magnitude (Figure 2.6a) shows edges similar to those imaged by the maximum aberrancy magnitude (Figure 2.6b). The intermediate and minimum aberrancy magnitudes (Figures 2.6c and 2.6d) do not provide useful information. As a result, I use the total aberrancy in further analyses and neglect the rest of aberrancy attributes. Visual evaluation of the individual cyclic color-based attributes such as dip azimuth (Figure 2.7a), the strike of curvature (Figure 2.7b) and total aberrancy azimuth (Figure 2.7c) suggest these are not useful. Later, I will show the value of these attributes when they are co-rendered with other attributes.

GLCM attributes (Figure 2.8) showed the same faults seen in other attributes and do not add much additional geological information on their own. On the other hand, the GLCM attributes work well with classification machine learning algorithms, as I will show later. In summary, some individual attributes (e.g., dip magnitude, multispectral energy ratio similarity, broadband energy ratio similarity, and others) seem more useful for detecting small faults whereas other attributes seem redundant or have limited value. In the next section, I will show that combining the structural information from multiple seismic attribute volumes can further enhance the subtle fault detection.

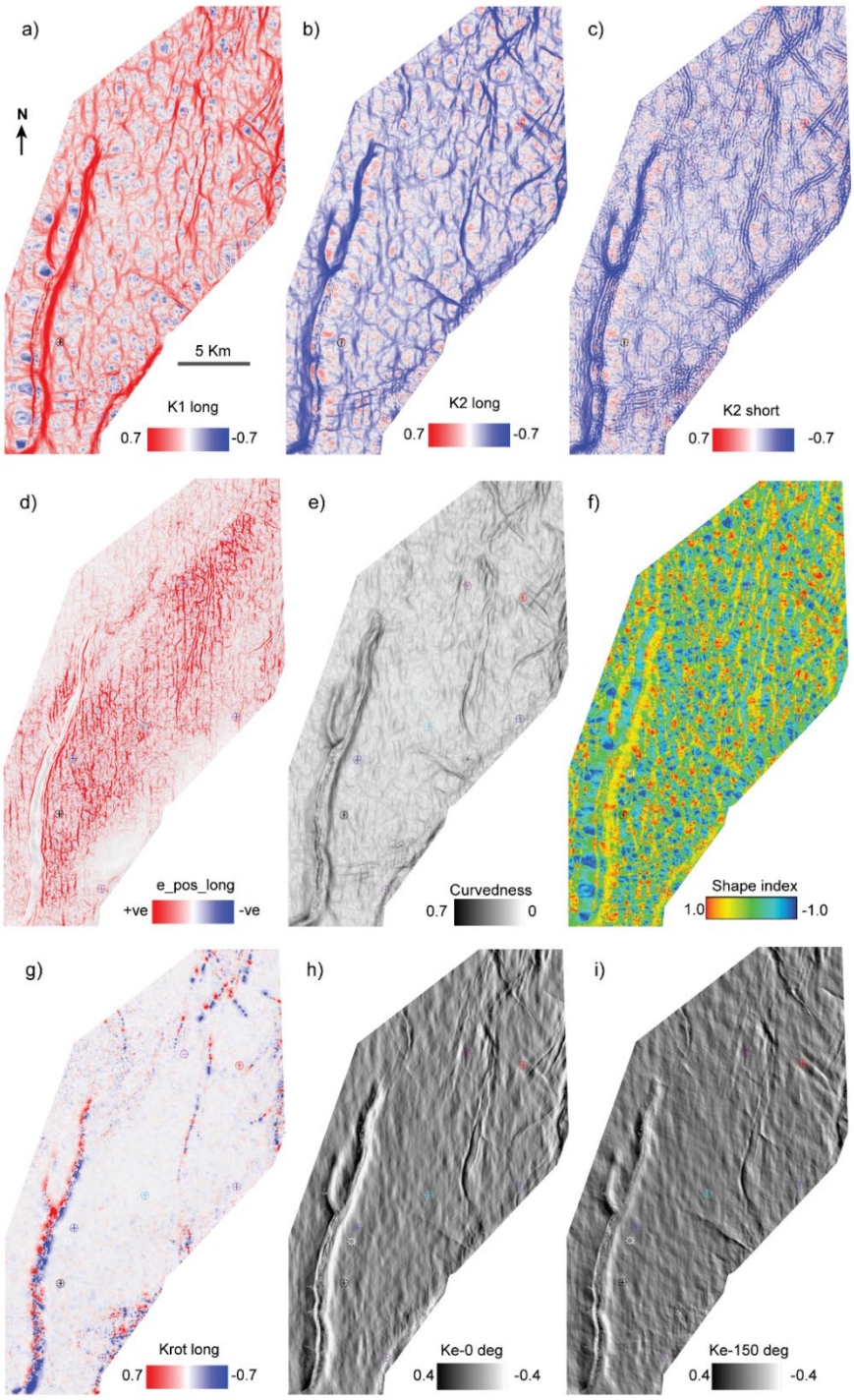

Figure 2. 5. Horizon slices extracted along the top of the C1 Sand reservoir from (a) Long-wavelength most positive principal curvature (K1 long), (b) Long-wavelength most negative principal curvature (K2 long), (c) Short-wavelength most negative principal curvature (K2 short), (d) Long-wavelength amplitude curvature (e_pos_long), (e) Curvedness, (f) Shape index, (g) Long-wavelength reflector rotation (Krot long), (h) Euler curvature at zero degree (Ke-0 deg), (i) Euler curvature at 150-deg (Ke-150 deg).

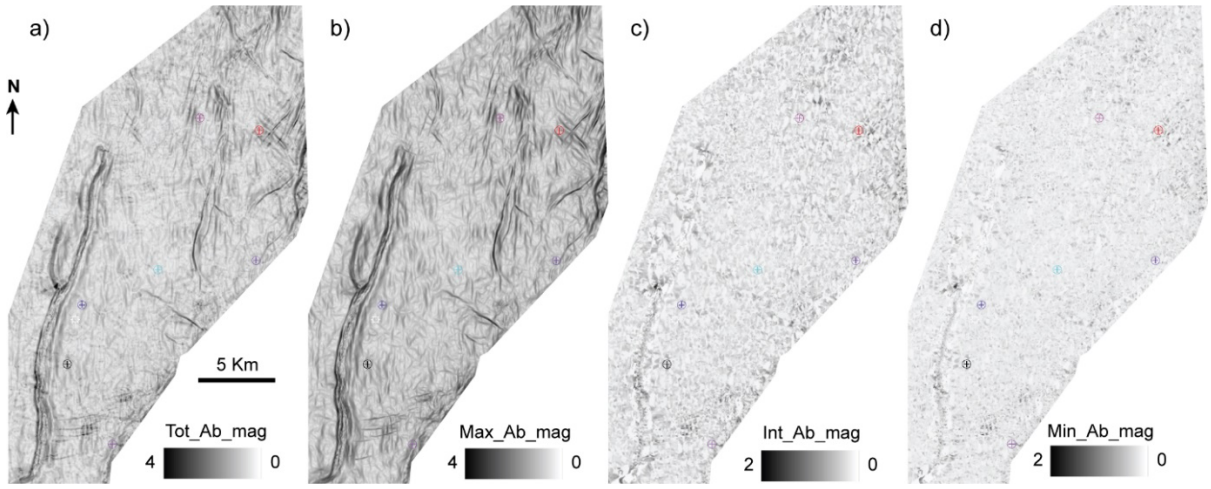

Figure 2. 6. Horizon slices extracted along the top of the C1 Sand reservoir from (a) Total aberrancy magnitude (Tot_Ab_mag), (b) Maximum aberrancy magnitude (Max-Ab_mag), (c) Intermediate aberrancy magnitude (Int-Ab_mag) and (d) Minimum aberrancy magnitude (Min-Ab_mag) volumes.

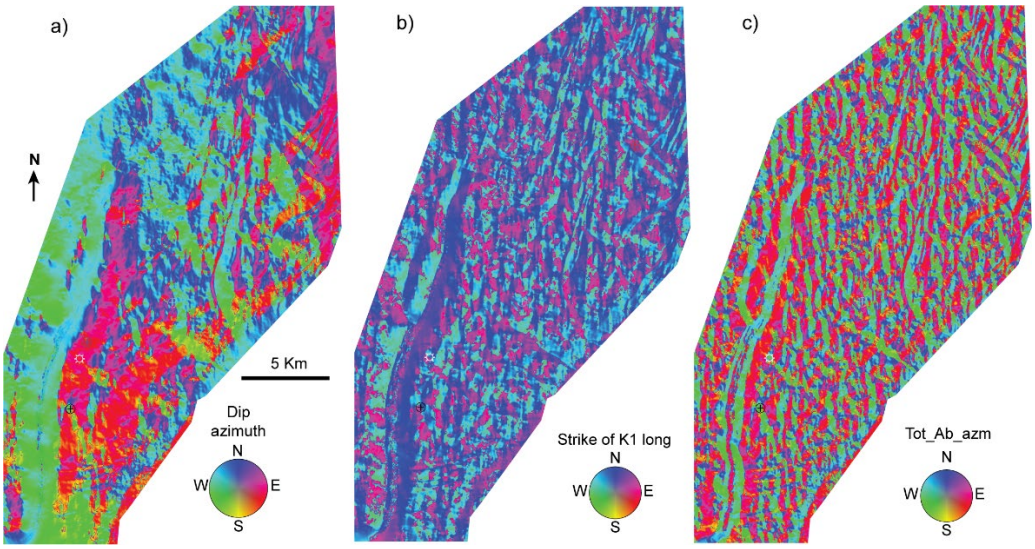

Figure 2. 7. Horizon slices extracted along the top of the C1 Sand reservoir from (a) Dip azimuth, (b) Strike of long-wavelength most positive principal curvature (Strike of K1 long) and (c) Total aberrancy azimuth (Tot_Ab_azm) volumes.

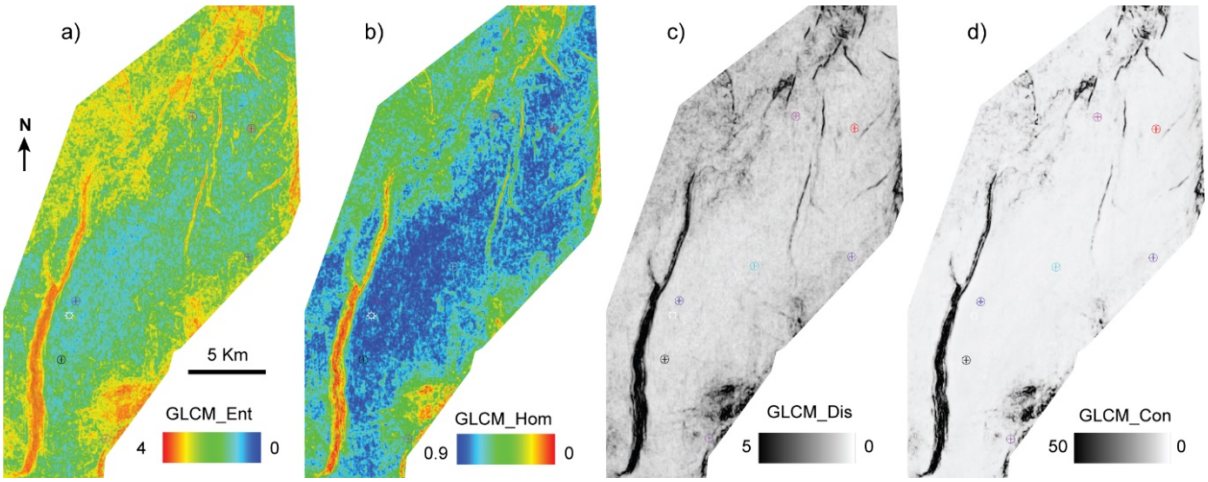

Figure 2. 8. Horizon slices extracted along the top of the C1 Sand reservoir from (a) GLCM entropy (GLCM_Ent), (b) GLCM homogeneity (GLCM_Hom), (c) GLCM dissimilarity (GLCM_Dis) and (d) GLCM continuity (GLCM_Con) volumes.

2.7 Interactive seismic attribute interpretation

Based on the visual analysis of the different seismic attributes (Figures 2.4 to 2.8), I select the individual attributes of dip magnitude, dip azimuth, multispectral energy ratio similarity, broadband energy ratio similarity, long- and short-wavelength most positive and most negative principal curvatures, curvedness, shape index, reflector rotation, and total aberrancy attributes for further study. Here I attempt to combine attributes to extract more information from the data. I combine the attributes in two ways. Firstly, I use multiattribute display capabilities available in seismic interpretation systems that allow us to co-render the geological images captured from a maximum of four seismic attribute volumes. Secondly, I use unsupervised machine learning algorithms.

2.7.1 Attribute selection for a human interpreter

Co-rendering the dip magnitude and dip azimuth (Figure 2.9a) showed the edges of the main faults affecting the reservoir and the changes in dip of the seismic events that resulted from tectonic deformation. Co-rendering the long- and short-wavelength principal structure curvatures with multispectral energy ratio similarity (Figures 2.9b and 2.9c) showed the main faults affecting the area. The short-wavelength curvature attributes show a localized intense zone of fractures close to the main faults (Figure 2.9c). These fractures are below the seismic resolution with 19 m tuning thickness and cannot be imaged by the long-wavelength curvature attributes (Figure 2.9b). The most positive and most negative principal curvature attributes show positive and negative curvature anomalies that bracket the multispectral energy ratio similarity anomalies of the reverse fault WF (red arrow) on the west side of Maui B (Figure 2.9b).

The lineaments seen in the most positive and most negative curvature attributes occur where there are no observed multispectral energy ratio similarity anomalies (the green arrows in Figure 2.9b). This indicates that there may be small faults with no clear offsets in this part of the field. In the central and eastern parts of the Maui A region, the multispectral energy ratio similarity attribute shows segmented anomalous associated with Ihi faults (cyan arrow in Figure 2.9b) and small faults shown by the white arrow. However, the most positive and most negative principal curvatures and the co-rendered dip azimuth and dip magnitude illuminate continuous fault alignments of the Ihi fault and intersecting faults in the eastern part of Maui A region (Figures 2.9a and 2.9b). In the far northern part of the Maui field, the multispectral energy ratio similarity attribute shows a set of en-echelon faults (purple arrow in Figure 2.9b). In contrast, the curvature and dip attributes show two intersecting continuous faults.

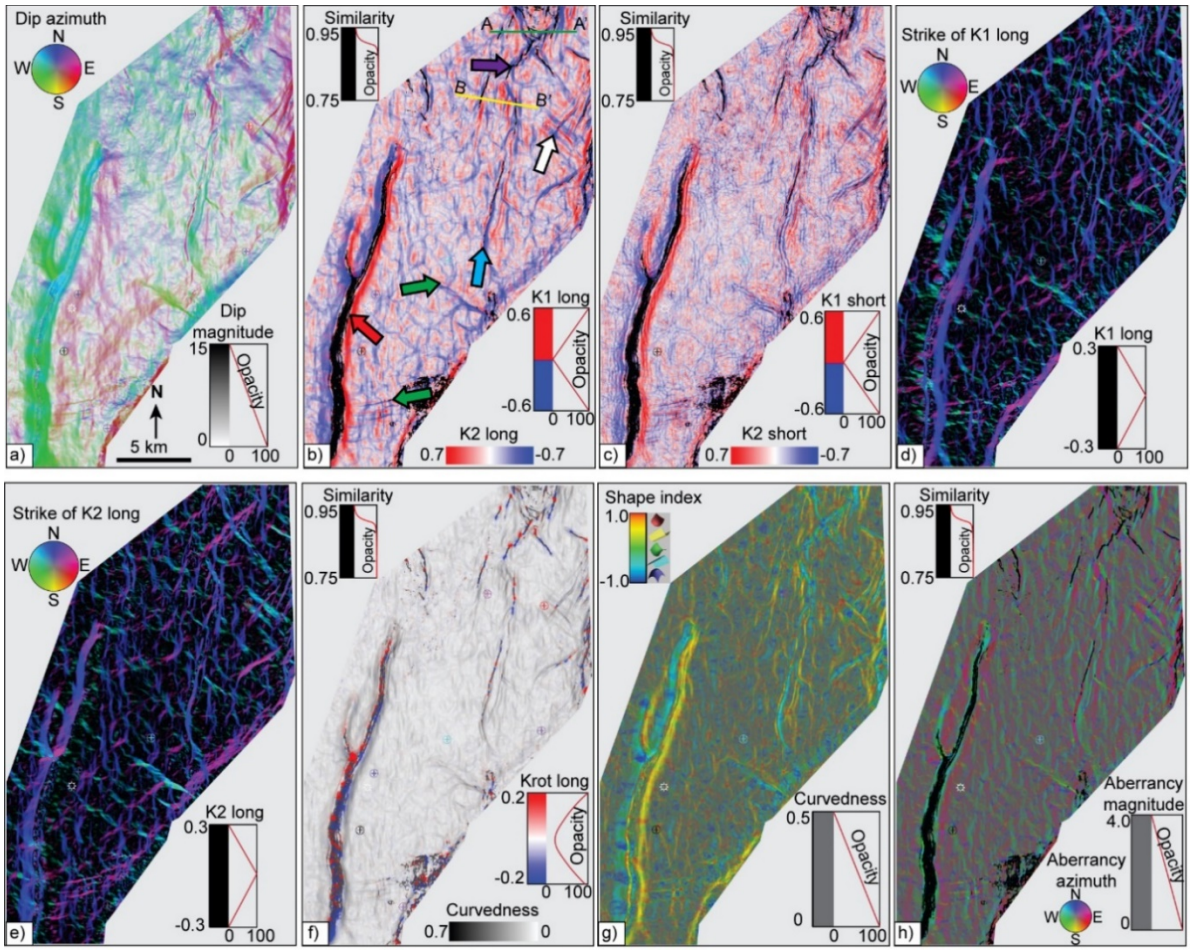

Figure 2. 9. Multiattribute horizon slices extracted along the top of the C Sand reservoir from (a) Dip magnitude modulated by dip azimuth, (b) Co-rendered long-wavelength most positive (K1 long), most negative principal (K2 long) curvatures and multispectral energy ratio attributes, (c) Co-rendered short-wavelength most positive (K1 short), most negative (K2 short) principal curvatures and multispectral energy ratio similarity attributes, (d) Long-wavelength most positive principal curvature modulated by its strike, (e) Long-wavelength most negative principal curvature modulated by its strike, (f) Co-rendered reflector rotation (Krot long), curvedness and multispectral energy ratio similarity, (g) Shape index modulated with curvedness, (h) Co-rendered multispectral energy ratio similarity with total aberrancy magnitude and azimuth. Note multispectral energy ratio similarity and reflector rotation show the en-echelon faults (purple arrow) affecting Maui north whereas curvature and dip attributes show two continuous intersecting faults. Dip and curvature attributes show lineaments associated with Ihi fault (cyan arrow) and faults affecting the eastern and southern part of the field (white and green arrows) whereas energy ratio similarity shows segmented or no anomalies associated with those faults. The Whitiki fault (red arrow) can be detected on all attributes.

Most positive and most negative principal curvatures modulated by their strikes (Figures 2.9d and 2.9e) show lineaments that can be interpreted as small faults or fractures that are below the seismic resolution. These small faults are not well-illuminated by similarity or dip attributes. Co-rendered reflector rotation with multispectral energy ratio similarity and curvedness (Figure 2.9f) show the faults along with the relative rotation of the faulted blocks about the faults' tips in the central and northern parts of the field. This display indicates that the northern part of the area is affected by a set of en-echelon normal faults, not simply two faults intersecting each other. The shape index modulated with curvedness (Figure 2.9g) shows the total deformation of the seismic events and illuminates not only the main faults affecting in the reservoir but also the fractures that are below the seismic resolution. Being mathematically independent of each other, the curvature and dip attributes seem to complement the energy ratio similarity attribute.

Total aberrancy modulated with multispectral energy ratio similarity (Figure 2.9h) shows sharp aberrancy anomalies at the same spatial position as the multispectral energy ratio similarity anomalies, illuminating the main faults affecting in the area. Aberrancy also shows continuous anomalies that clearly images the Ihi fault and the faults in Maui south and east. In addition, aberrancy shows some small-scale lineaments that could indicate either flexures that are below the seismic resolution or are acquisition artifacts. For verification, these small-scale lineaments could be correlated to image logs if those were to become available. The aberrancy attribute complements the dip, coherence and curvature attributes.

I now discuss vertical slices extracted from the seismic attribute volumes. Vertical slices A-A' (the green line in Figure 2.9b) cross the far northern part of Maui and are extracted from the preconditioned seismic amplitude (Figure 2.10a), the co-rendered preconditioned seismic amplitude, broadband energy ratio similarity, dip magnitude and dip azimuth volumes (Figure 2.10b), the co-rendered preconditioned seismic amplitude, multispectral energy ratio similarity, dip magnitude and dip azimuth volumes (Figure 2.10c) and the co-rendered preconditioned seismic amplitude, long-wavelength most positive and most negative principal curvature attributes (Figure 2.10d). Faults that show clear offset on seismic amplitude data can be imaged by energy ratio similarity attributes (Figures 2.10b and 1.10c). However, the multispectral energy ratio similarity shows sharper and more continuous faults (the cyan arrow in Figure 2.10a) compared to those imaged by broadband energy ratio similarity attributes. I notice a fault with clear offset (purple arrow in Figure 2.10a) and deformation of the seismic event on the hanging wall as evidenced by changes in the dip azimuth and bent reflectors. This fault exhibits a similarity anomaly at the inferred fault position whereas dip and negative curvature anomalies occur on the hanging wall of the fault.

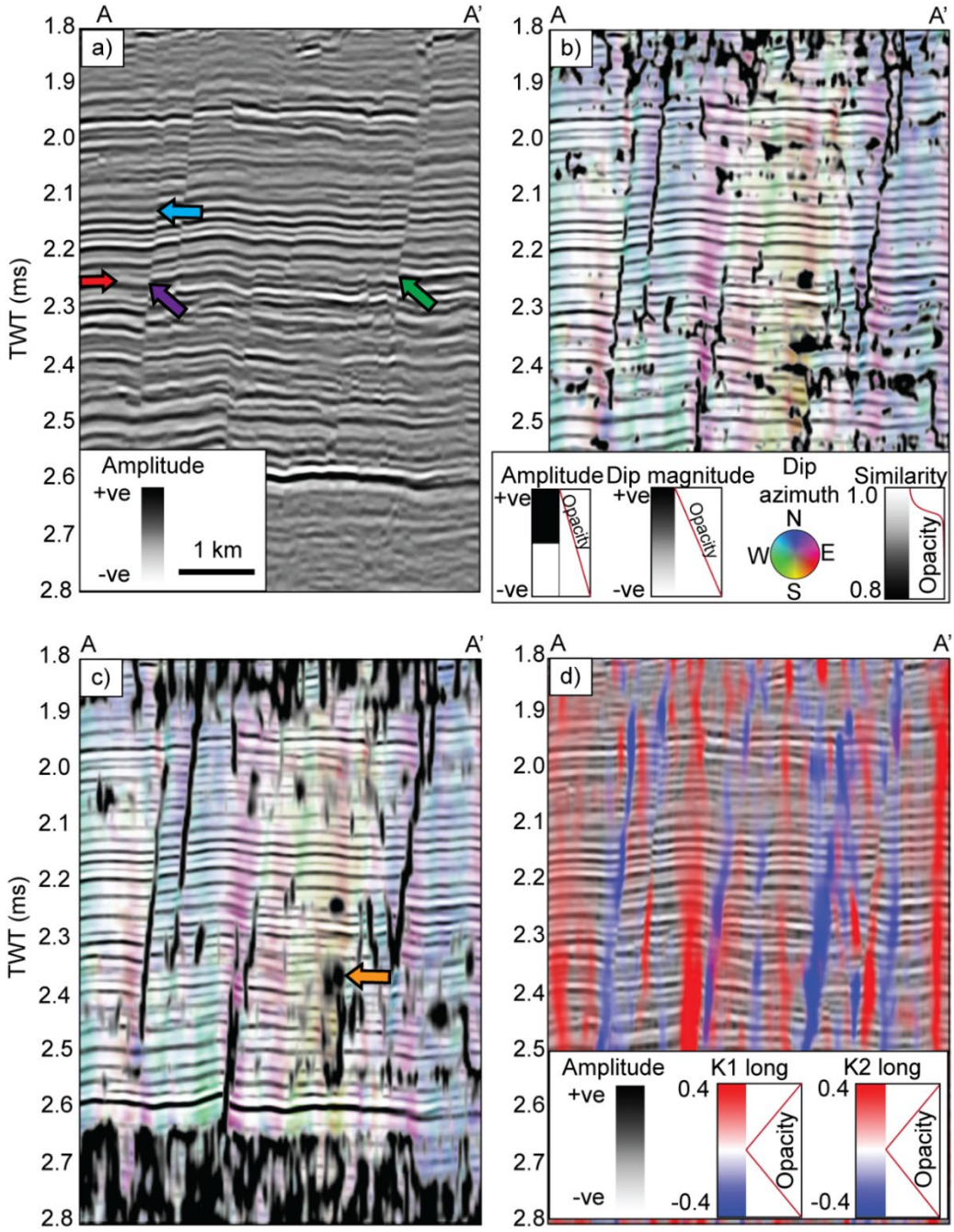

Figure 2. 10. Arbitrary seismic line A-A' (location shown by green line in Fig. 5b) across the northern part of the Maui field extracted from (a) a preconditioned seismic volume, (b) co-rendered preconditioned seismic, dip magnitude, dip azimuth and broadband energy ratio similarity, (c) co-rendered preconditioned seismic amplitude, dip magnitude, dip azimuth and multispectral energy ratio similarity, (d) co-rendered preconditioned seismic amplitude, long-wavelength most positive and most negative principal curvature attributes. The red arrow refers to the top of the C Sand seismic event. The cyan, purple, and green arrows denote different kinds of faults affecting Maui north. The orange arrow refers to similarity anomalies that could be interpreted as channelized features. Vertical exaggeration is 7.5:1.

The green arrow in Figure 2.10a indicates one of the en-echelon faults interpreted on the multispectral energy ratio data (Figure 2.10b). There is a clear offset but no change in the dip of the seismic reflectors on either side of the fault and little upward bend in the footwall reflectors. This give rise to a similarity anomaly at the inferred fault position and a positive curvature anomaly on the footwall of the fault (Figure 2.10d). Therefore, I prefer to use the multispectral energy ratio similarity attribute to map these faults as it provides sharper and more continuous similarity anomalies at the fault planes (Figure 2.10c) compared to those illuminated by the curvature and dip attributes. I also observed some low similarity anomalies (orange arrow in Figure 2.10c) across the line that might indicate channelized features.

Vertical slice B-B' (the yellow line in Figure 2.9b) crosses the Ihi fault and is extracted from the preconditioned seismic volume (Figure 2.11a), the co-rendered preconditioned seismic amplitude, broadband energy ratio similarity, dip magnitude, and dip azimuth (Figure 2.11b), the co-rendered preconditioned seismic amplitude, multispectral energy ratio similarity, dip magnitude, and dip azimuth (Figure 2.11c), and the co-rendered preconditioned seismic, long-wavelength most positive and most negative principal curvature attributes (Figure 2.11d). In Figure 2.11a, the fault denoted by the purple arrow has clear offset and no change in the dip of the seismic reflectors on either side of the fault. However, these reflectors appear slightly folded near the fault (red dash line in Figure 2.11a). This fault shows clear energy ratio similarity anomalies (Figure 2.11b and 2.11c). The most positive and most negative curvature attributes show anomalies on the footwall and hanging wall of this normal fault (Figure 2.11d). One fault (the green arrow of Figure 2.11a) of the Ihi fault system does not display clear offsets but there are changes in the dip of the faulted blocks on each side of the fault that show a dip anomaly. Also, the seismic reflectors on each side of this fault are bent and display positive and negative

anomalies on both sides of the fault (Figure 2.11d). As a result, this fault is not well-illuminated by energy ratio similarity attributes. The other Ihi fault (blue arrow) displays clear offset and changes in the dip of the seismic reflectors on each side of the fault in addition to bent reflectors along the hanging wall of the fault. This fault exhibits clear energy ratio similarity anomalies (Figures 2.11b and 2.11c), a small dip anomaly and small negative curvature anomalies on the hanging wall of this fault. Thus, horizon slices extracted from the dip and curvature attributes show continuous images of the Ihi fault (Figures 2.9a, 2.9b, and 2.9c) compared to the energy ratio similarity images. The arrows in Figure 2.11c show low energy ratio similarity features that might indicate deformation within the shales overlying the C Sand reservoir (cyan arrow) and small channelized features (orange arrow).

In this section, I have shown how the visual analysis of geometric attributes can aid in imaging faults and fractures. I have discussed the eight most useful combinations of sixteen different geometric attributes used to map faults and fractures in the Maui field. Given the large data volumes inherent in most 3D seismic surveys, delineation of small faults and fractures for reservoir development in a timely manner can be challenging. Co-rendering multiple attributes is useful but is limited to only four attributes using RGB (red-green-blue), CMY (cyan-magenta-yellow) or HLS (hue-lightness-saturation). As a result, I seek methods to combine large numbers of attributes that are also less reliant on visual interpretation. In the next section, I explore other ways to combine attributes using unsupervised machine learning.

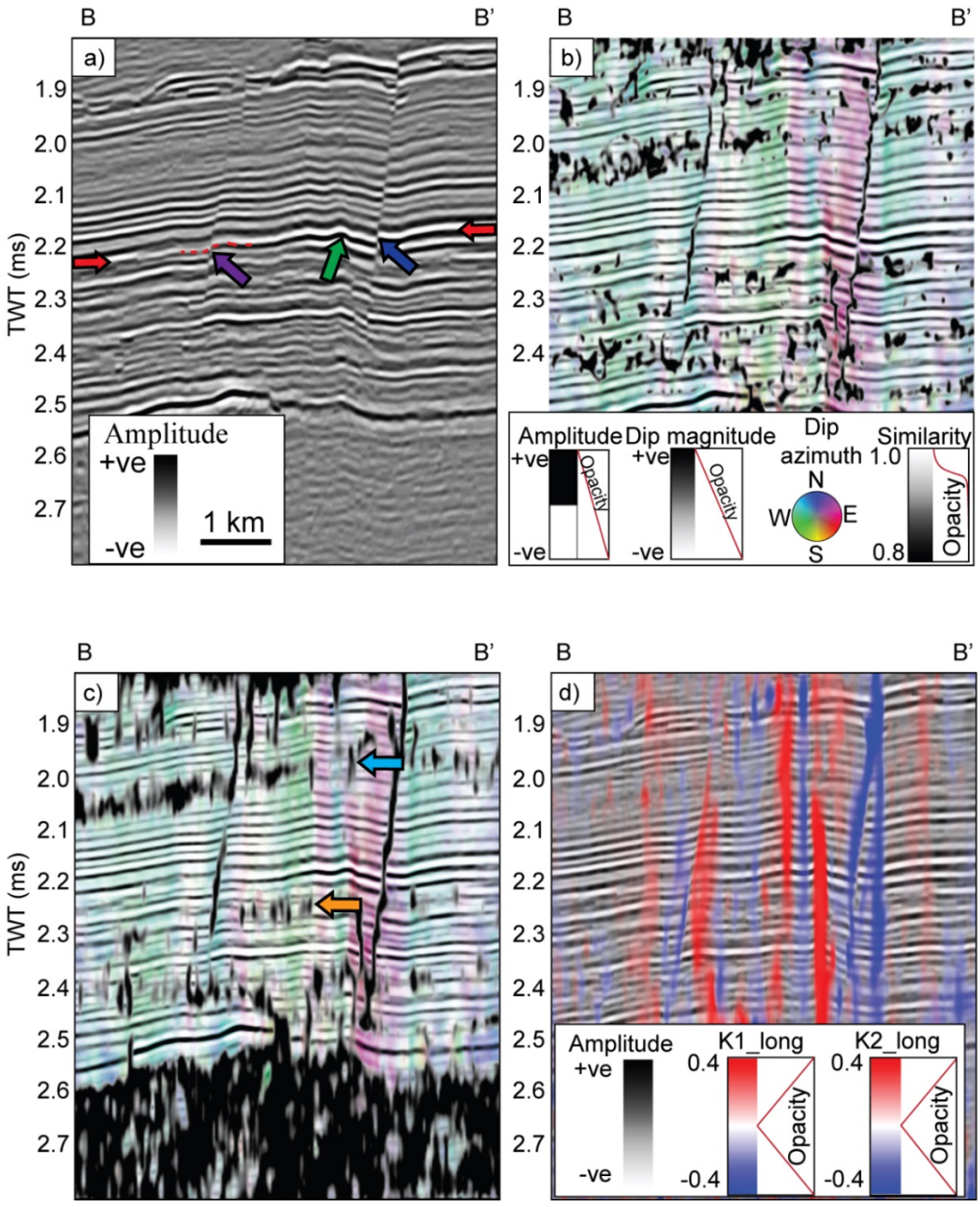

Figure 2. 11. Arbitrary seismic line B-B' (location shown by yellow line in Fig. 5b) that crosses the Ihi fault, extracted from (a) a preconditioned seismic volume, (b) co-rendered preconditioned seismic, dip magnitude, dip azimuth and broadband energy ratio similarity, (c) co-rendered preconditioned seismic amplitude, dip magnitude, dip azimuth and multispectral energy ratio similarity attributes, (d) co-rendered preconditioned seismic amplitude, long-wavelength most positive and most negative principal curvature attributes. The red arrows refer to the C Sand seismic event. The purple, green, and blue arrows denote different faults affecting Maui A region. The cyan and orange arrows indicate low energy ratio similarity anomalies that suggest deformation within the shales overlying the C Sand reservoir and small channelized features, respectively. Vertical exaggeration is 7.5:1.

2.7.2 Attribute selection for SOM analysis

Computer-aided clustering techniques are useful for integrating the geological content of more than three seismic attributes (Zhao et al., 2015; Marfurt, 2018). Unsupervised machine learning algorithms such as self-organizing maps (SOM) apply non-linear neural networks to multiple seismic attribute volumes in order to understand how these attributes relate to each other and to reduce the dimensionality of the data (Kohonen, 1982). A SOM groups similar data and uses a 2D topology map to display these groups or clusters. The number of clusters or classes is controlled by a user-defined number of neurons (called prototype vectors in other publications) within the 2D map. These clusters gather the information from the seismic attribute volumes into one classification volume that can facilitate geological interpretation (Coléou et al., 2003; Roy, 2013).

Selecting the right attributes to be used as inputs to a SOM significantly influences the classification results (Barnes and Laughlin, 2002). Principal component analysis (PCA) is a linear mathematical technique that aids in distilling a library of seismic attributes into a small set of attributes, which contain the largest variations within the dataset (Roden et al., 2015). However, PCA does not provide any information about the spatial positions of anomalous zones within the seismic attribute volumes.

In general, machine learning algorithms are more quantitative and can perform repeated tasks with as many voxels as needed more quickly compared to humans. However, humans can recognize larger-scale patterns and put them in a geologic context. For instance, a human interpreter can infer the presence of a fault by observing that the most positive and most negative curvature anomalies bracket a coherence anomaly. The computer algorithms cannot understand this spatial pattern (Infante-Paez and Marfurt, 2019). Therefore, not all the attributes that human interpreters use for fault interpretation can be used as inputs to machine learning algorithms. Machine learning is best applied to attributes that highlight a feature of interest lie within the same seismic voxel. Based on our previous discussion, the dip magnitude, coherence, curvedness, total aberrancy magnitude, and GLCM attributes show anomalies at the inferred fault planes. Thus, these attributes are considered as candidates for SOM analysis.

Zhao et al. (2018) highlight the importance of selecting suitable weights of seismic attributes used as inputs to SOM based on human experience and the preference of the unsupervised machine learning algorithm. To emphasize the importance of an attribute in the SOM classification process, a larger weight should be applied to this attribute. Zhao et al. (2018) define a weight matrix based on the distance between multiattribute data in the SOM space and a histogram analysis of the individual attributes.

In this study, I select the seismic attributes based on our interpretation experience (Figures 2.4 to 2.11) and then input these attributes to a PCA analysis to obtain the weights of each attribute depending on its contribution to the data within the interval of interest. The SOM workflow used in this study is shown in Figure 2.12. I use the multispectral energy ratio similarity, dip magnitude, curvedness, total aberrancy magnitude, GLCM homogeneity and GLCM entropy as inputs to PCA. I feed these six attributes with their associated weights obtained from the first four PCA eigenvectors to the SOM analysis. The PCA and SOM analyses are performed on the seismic samples (voxels) within the interval of interest which is from the C Shale horizon to D Sand horizon. The SOM classification uses an 8x8 topology.

A horizon slice extracted from the SOM classification volume along the top of the C Sand reservoir (Figure 2.13a) clearly shows all of the small faults in the reservoir. In the northern part of the field, the horizon slice shows the sharp edges of a NW-SE fault (white arrow in Figure 2.13a; F1 in Figure 2.13b) that are cross-cut by a set of en-echelon normal faults (F2 in Figure 2.13b). Imaging such fault patterns and understanding the fault mechanism is important for advanced structure and reservoir analyses.

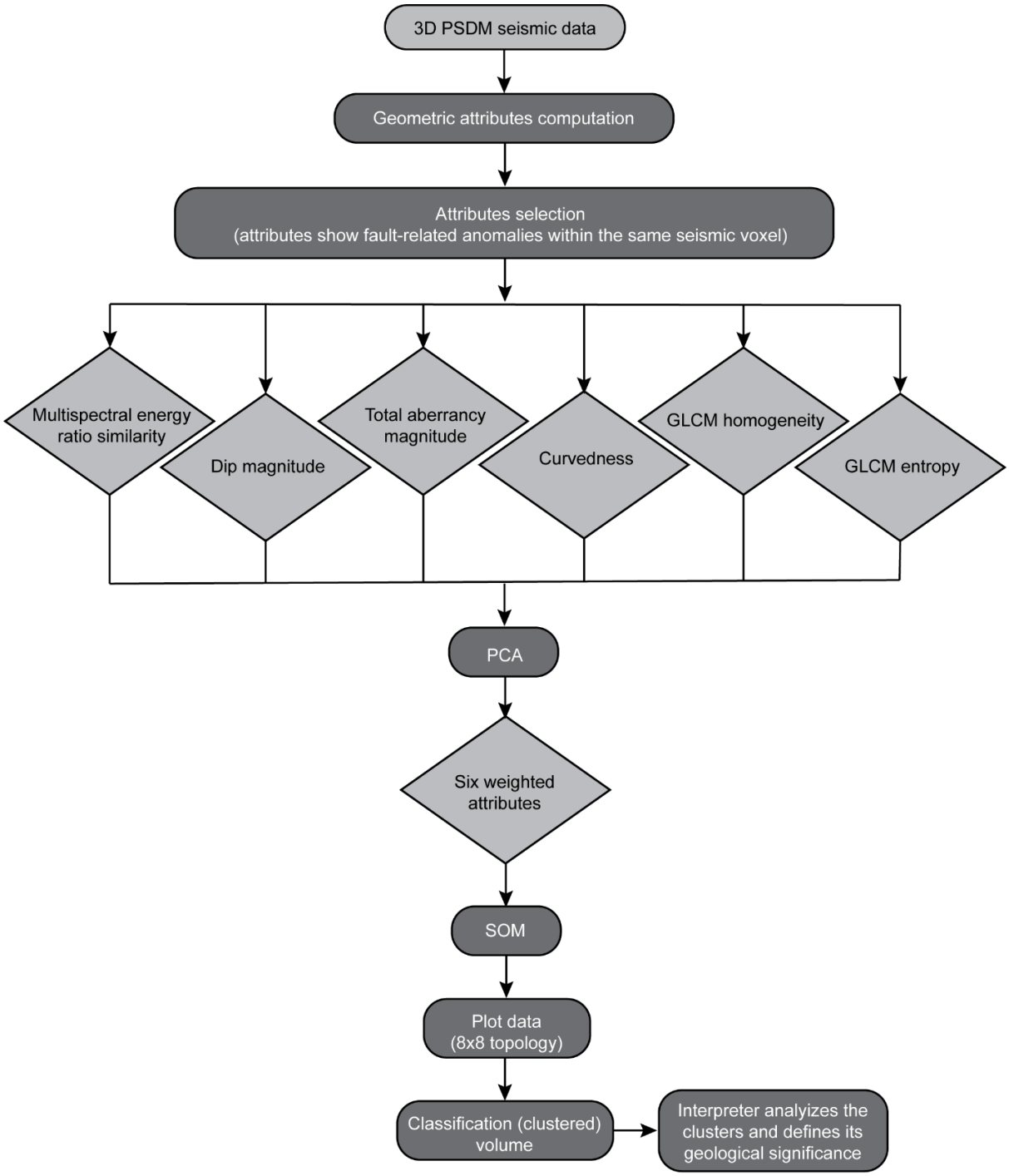

Figure 2. 12. Proposed workflow from this study for clustering and combining data from six geometric seismic attributes by using PCAs and SOMs. GLCM - Gray-level co-occurrence matrix; PCA - principal component analysis; SOM - self-organizing map.

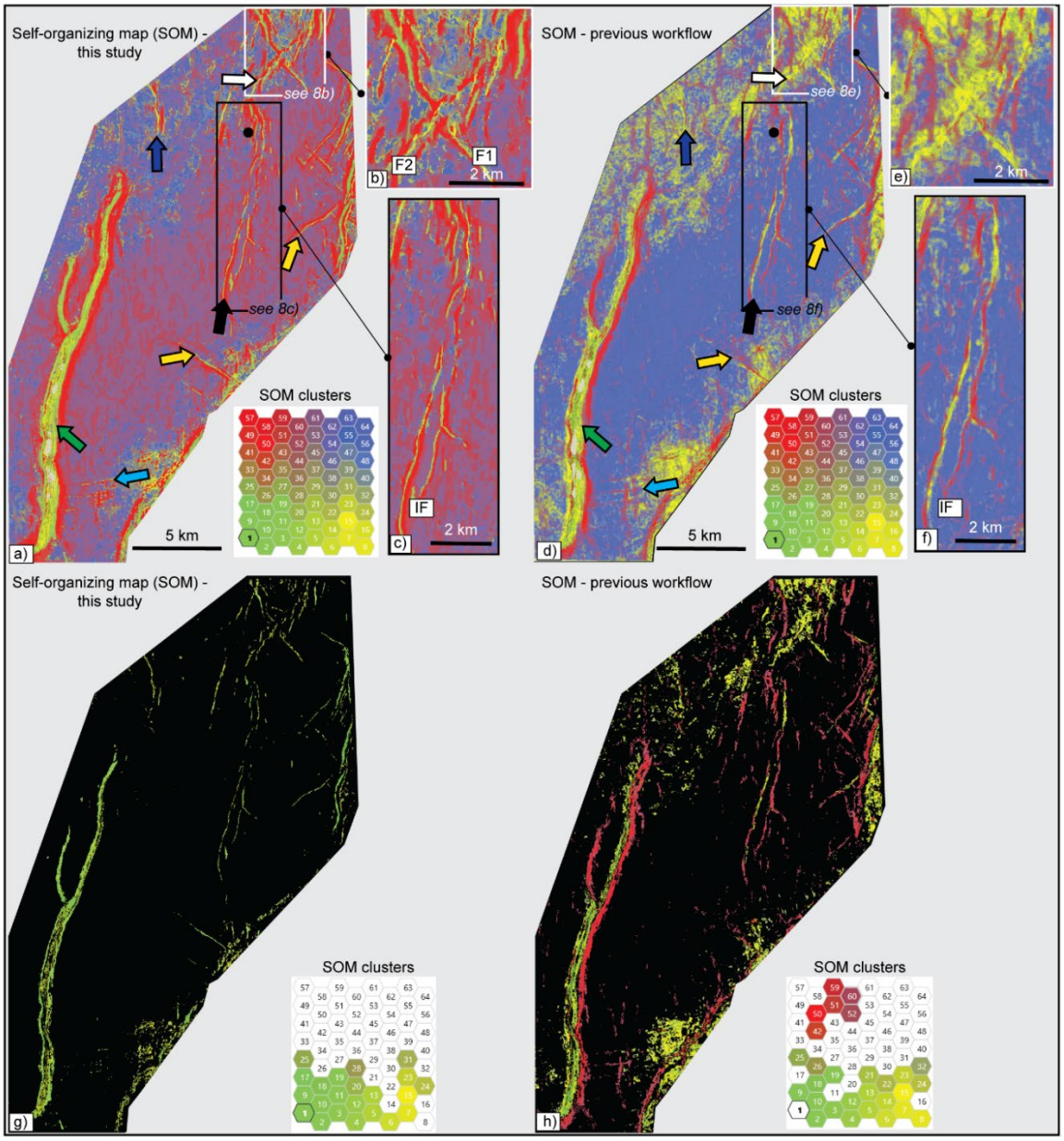

Figure 2. 13. Comparison between the preferred workflow from this study (left side) and a SOM generated by following a previous workflow of Lauden et al., (2019) (right side). (a) Horizon slice extracted along the top of the C Sand reservoir from our preferred SOM classification volume by using six weighted geometric attributes based on the proposed workflow in this study. (b) Expanded image of the far northern part of the field from a). (c) Expanded image of Ihi fault from a). (d) Horizon slice extracted along the top of the C Sand reservoir by using four geometric attributes as described by Lauden et al. (2019). (e) Expanded image of the far northern part of the field from d). (f) Expanded image of Ihi fault from d). (g) Horizon slice follows a) but only has the fault-related SOM neurons turned on. (h) Horizon slice follows d) but only has the fault-related SOM neurons turned on. This study SOM shows sharper fault edges (compare arrows in a) and b) and expanded images b), c), e) and f)). Horizon slice g) shows cleaner and sharper fault edges compared to slice h).

The horizon slice (Figure 2.13a) also shows clear and sharp edges for faults in the Maui east (yellow arrows), Maui west (blue arrow), and Maui south (cyan arrow) areas. Mapping small faults and obtaining the sharpest fault edges is critical for reservoir development studies. In the Maui field, the SOM result shows the sharpest image of the conjugate Ihi faults (black arrow) compared to other attributes (Figures 2.4 and 2.11). These faults consist of small segments that seem to touch each other at their tips (Figure 2.13c). Understanding this fault pattern enabled the operator (Shell in 2006) to drill the MA-02A well on the west side of the Ihi fault. The field was producing from the C Sand reservoir on the east side of Ihi fault for 29 years. In 2006, the MA-02A well (the black circle in Figure 2.13a) penetrated the same reservoir on the west side of Ihi fault and encountered gas with the original gas-water contact depth (i.e., unswept reservoir) (Telford and Murray, 2008).

2.8 Discussion

Although many case studies have been published regarding the application of SOM to facies classification in different geologic settings (e.g., Roy et al., 2010; Matos et al., 2011; Zhao et al., 2015, 2018; Infante-Paez and Marfurt, 2019), there has been less focus on the application of SOM to fault detection (Dewett and Henza, 2016; Laudon et al., 2019).

In order to demonstrate the importance of selecting the appropriate weighted attributes for detecting small faults, I tested Laudon et al.'s (2019) workflow on Maui dataset (Figure 2.13). Following Laudon et al.'s approach, I use most positive curvature, energy ratio similarity, GLCM entropy and GLCM homogeneity attributes as inputs to SOM analysis (right side of Figure 2.13). I assigned all attributes to have the same weights within the SOM analysis. I combined geological information from most positive curvature attribute, which shows anomalous features at different spatial positions with respect to the inferred fault locations, with similarity and GLCM attributes that display anomalous features at the inferred fault planes.

A horizon extraction along the top of the C Sand reservoir from the produced previous SOM (Figure 2.13d) showed that the faults in the Maui east (yellow arrow) and south (cyan arrow) areas of the field are illuminated but appear blurred compared to the SOM slice obtained using PCA-derived weighted attributes (compare Figures 2.13a and 2.13d). Laudon et al.'s approach (Figure 2.13d) does not clearly detect the faults affecting the far northern (white arrow) and northwest parts of the field (blue arrow). In these areas, the SOM result using equally weighted attributes seems to be noisy. Comparing Figures 2.13b and 2.13e, this study's SOM approach more clearly shows the en-echelon faults affecting Maui north (Figure 2.13b) while the results obtained using equal weights look noisy (Figure 2.13e). Also, the SOM classification volume obtained using equally weighted attributes (black arrow in Figure 2.13d) failed to image the segmented faults within the Ihi faults.

Comparing Figures 2.13c and 2.13f, I noted that the proposed method (Figure 2.13c) clearly shows sharper segmented faults within Ihi fault whereas the Loudon et al. approach shows more blurred image of the Ihi faults (Figure 2.13f). a closer investigation of the SOM results is obtained by turning on the neurons that are related only to the faults for this study (Figure 2.13g) and for the Laudon et al. (Figure 2.13h). This study SOM produces cleaner and sharper faults compared to the previous workflow result. Therefore, the results presented here provide alternative seismic attributes for application to further SOM studies and further demonstrates the advantage of weighted attributes.

2.9 Conclusions

Small faults overlooked on seismic amplitude data can form important seals or conduits that dramatically control hydrocarbon migration and trapping within a petroleum reservoir. I find that seismic attributes are useful for detecting subtle faults in the Maui field of New Zealand. However, the interpretation of individual attributes can be a tedious and time-consuming task. Multiple attribute analyses, such as co-rendering and principal component analysis (PCA) and self-organizing maps (SOM) algorithms, help to extract more insightful geological information compared to individual volumetric attribute analyses. However, unlike human interpreters, who are capable of recognizing spatial patterns within data and assign geological context, the SOM technique is a sample-based algorithm that works best when the multiple seismic attribute volumes exhibit anomalous features within the same seismic voxel. From my investigation, I found that incorporating appropriate seismic attributes that exhibit anomalous features at the same seismic voxel to PCA and SOM analyses aids in combining the geological context from six seismic attributes into one enhanced classification volume. This clustered volume enables me to better detect subtle faults within the C Sand reservoir of the Maui Field that were not easily revealed from conventional seismic interpretation techniques. In the future, given sufficient amounts of labelled data and selecting the appropriate attributes, I anticipate that supervised machine learning algorithms such as convolutional neural networks may be able to mimic the ability of a human interpreter to delineate small faults within hydrocarbon reservoirs.

3 Machine learning for reservoir evaluation and rock type identification from seismic data

3.1 Summary

Net reservoir discrimination and rock type identification play vital roles in determining reservoir quality, distribution, and identification of stratigraphic baffles for optimizing drilling plans and economic petroleum recovery. Although it is challenging to discriminate small changes in reservoir properties or identify thin stratigraphic barriers below seismic resolution from conventional seismic amplitude data, I find seismic attributes aid in defining reservoir architecture, properties, and stratigraphic baffles. However, analyzing numerous individual attributes is a time-consuming process and may have limitations for revealing small petrophysical changes within a reservoir. Using the Maui 3D seismic data acquired in offshore Taranaki Basin, New Zealand, I generated typical instantaneous and spectral decomposition seismic attributes that are sensitive to lithological variations and changes in reservoir properties. I found that integrating the geological content of a combination of eight spectral instantaneous attribute volumes using an unsupervised machine learning algorithm (self-organizing maps - SOM) results in a classification volume that can highlight reservoir distribution and identify stratigraphic baffles. I found that SOM classification of natural clusters of multi-attribute samples in attribute space are sensitive to subtle changes of the reservoir petrophysical properties. Thus, this approach helps to understand reservoir quality and heterogeneity in addition to illuminating thin reservoirs and stratigraphic baffles. I found that SOM clusters appear to be more sensitive to porosity variations compared to lithological changes within the reservoir.

3.2 Introduction

Understanding the distribution of desirable reservoir qualities, flow behavior, and stratigraphic baffles remain challenging tasks for geoscientists and reservoir engineers. Poorly described reservoir characteristics can negatively impact reservoir performance prediction and well drilling plans (Sritongthae, 2016). At a well location, a geoscientist can perform petrophysical analyses to quantify reservoir properties and identify net reservoir and net pay intervals. In addition, rock typing analysis can be performed on core data and/or wireline logs to classify the reservoir rocks into distinct rock types and flow units, each of which has undergone similar geologic and diagenetic processes (Guo et al., 2007). Extending these rock types and flow units away from well control is critical to understand the lateral and vertical heterogeneity within the reservoir – essential for reservoir characterization and field management studies (Hami-Eddine and Furniss, 2013).

A fundamental task of 3D reservoir modeling is to interpolate and extrapolate the reservoir facies and properties away from well control. However, the accurate representation of reservoir geometry including the structural framework and stratigraphic details from well data, remains a key challenge (Branets et al., 2008). It is, therefore, necessary to integrate 3D seismic data and well-derived lithofacies and reservoir properties to build reliable 3D reservoir models.

Conventional approaches using pre-stack seismic and stochastic inversion (Doyen, 2007; Avseth et al., 2010) depend on the analysis of inverted 2D or 3D seismic data in the elastic property domain which may then be related to various geological facies (Hami-Eddine et al., 2015). However, seismic inversion can be a challenging process that requires data conditioning, precise wavelet estimation, and an accurate initial low-frequency model. These can be difficult to obtain (Marfurt and Kirlin, 2001; Sams and Carter, 2017). This approach also requires high quality pre-stack seismic data which are not always available. In addition, calibration of elastic inversion results to geologic facies is strengthened by high-quality shear logs that are expensive to acquire and may not be available.

With the advancement in the computing capability and machine learning algorithms, new approaches to reservoir characterization have been developed. For example, a democratic neural network association (DNNA) can be trained on pre-stack seismic data to predict discrete geologic facies logs at the well locations. The DNNA model uses a probabilistic approach, which finds patterns within the angle gathers that predict the lithologic distribution and their associated fluid content. Once trained, the DNNA model is applied throughout the field to obtain geologic facies along with uncertainty estimates (Hami-Eddine et al., 2009, 2013, 2015; Hami-Eddine and Furniss, 2011).

Using a different approach, Zhang et al. (2019) proposed a machine learning workflow that trains a random forest algorithm on labeled facies logs and angle stack seismic data to build facies probability cubes. This method can show intermediate-scale stratigraphic features such as oil-charged channels but it fails to illuminate fine-scale heterogeneity within the reservoir (Zhang et al., 2018). Although these machine learning approaches can be powerful tools to capture reservoir heterogeneity, like any other supervised machine learning algorithm, they require a large number of training wells to avoid bias and to generalize (Johnston, 1993).

With limited well control, supervised machine learning techniques cannot fully discriminate reservoir facies and identify rock types. An alternative approach is to use unsupervised clustering machine learning techniques that integrate the reservoir information from multiple seismic attributes on a sample-by-sample basis and classify separate groups of similar data together to obtain one classification volume. A human interpreter then ties these clusters to the available well control to identify reservoir facies and stratigraphic baffles. I demonstrate this approach using a 3D seismic data set with six vertical well penetrations in the C1 Sand reservoir of the Maui field in the offshore Taranaki Basin of New Zealand. I start with a discussion of the petrophysical properties of the reservoir. I next generated typical instantaneous and spectral decomposition attributes that are sensitive to lithological changes, reservoir properties, and thicknesses.

I propose a workflow to carefully select a combination of seismic attributes that can be input to an unsupervised self-organizing map (SOM) to integrate the geological content of those attributes into one classification volume. This classification volume shows various distinct attribute clusters that enable a discrimination between net reservoir and non-reservoir intervals. I perform rock typing analysis for the C1 Sand reservoir to identify the reservoir and baffle flow units then tie those flow units to the SOM classification results. The SOM-derived flow units can be viewed in 3D, which enables us to better understand reservoir quality and heterogeneity distribution throughout the field.

3.3 Depositional characteristics of C Sand reservoir

The Mangahewa formation, which is called C Sand in the Maui field, is 400 – 830 m thick with the thickest deposition in the Taranaki Peninsula region. It is considered one of the main producing reservoir and source rocks in Taranaki basin. The Mangahewa fairway consists of a broadly NE-SW trend of Middle to Upper Eocene-aged terrestrial to marginal marine and coastal lithofacies (Higgs et al., 2012). It consists mainly of interbedded sandstone, siltstone, mudstone, carbonaceous sandstone, and thin coal (King and Thrasher, 1996). Over the last decade, commercial hydrocarbon have been discovered within the Mangahewa formation in the Maui, Kapuni, Mangahewa, Cardiff/Radnor, Turangi/Ohanga, and Pohokura fields (Higgs et al., 2012).

The Maui field produces from northeast-southwest trending fairways of Paleocene to Eocene-aged stacked marginal marine-terrestrial sandstone reservoirs called the Maui F, D and C Sands (Bryant et al., 1994, 1995) (Figure 3.1). The gas compositions of the sand reservoirs in the Maui B region are richer in condensate compared to Maui A gas reservoirs and the reservoirs contain relatively thicker oil-rims (Seybold et al., 1996). Over this time period, the east-west to northeast-southwest oriented paleocoastline fluctuated from a position about 30 km north of the Maui field to the southern areas within the field (Haskell, 1991). These paleo-shoreline fluctuations back and forth within the Maui area resulted in a strong vertical layering sequence of sediments that allows geological subdivision of the productive interval and resulted in spatial variations of reservoir properties within the field (Bryant et al., 1995).

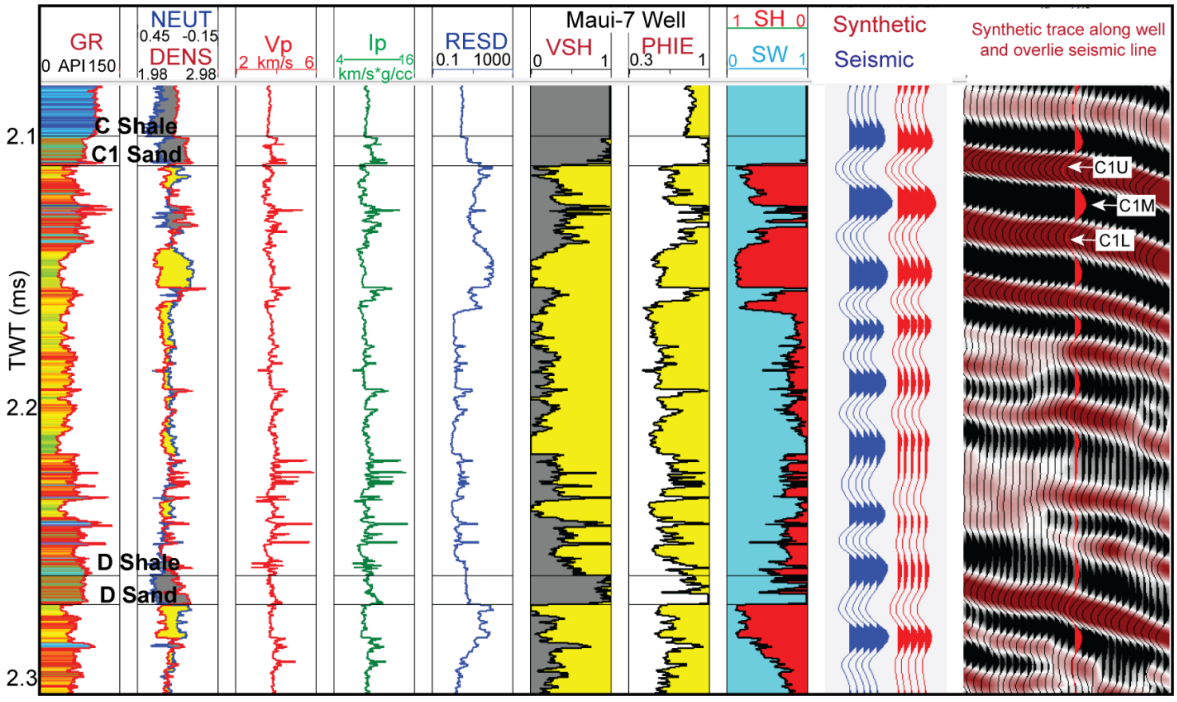

Figure 3. 1. Seismic-to-well tie for Maui-7 well shows C1U, C1M and C1L seismic events. Tracks from left to right display Gamma-ray (GR), Density-Neutron (DENS-NEUT), Compressional sonic velocity (Vp), Deep resistivity (RESD), Shale volume (VSH), Effective porosity (PHIE), Water saturation (SW) and Hydrocarbon saturation (SH) logs.

The sandstones deposited in the Maui field are arkosic arenites (i.e., rich in potassium feldspar) and have been linked to erosion of the Karamea granite outcrops in the northwest of the South Island (Chatellier and Hichings, 1987). The C Sand reservoir was deposited over the thick D Shale and is capped by the laterally extensive and thick C Shale (Figures 3.1 and 3.2). The C Sand reservoir can be divided into the C1, C2, and C3 intervals, although most of the gas-condensate reserves in Maui field are in the C1 Sand (Bryant et al., 1995; Pannett et al., 2004). This study focuses on the C1 Sand reservoir that is composed of middle Eocene-aged lower coastal plain to inner shelf sediments and forms a laterally continuous, high net-to-gross reservoir interval in the Maui field. However, a thin shale unit in the Maui B region, which is correlated to a carbonate-cemented unit in the Maui A region (Figures 3.1 and 3.2), serves to subdivide the C1 Sand reservoir into C1U (i.e. C1 upper) and C1L (C1 lower) (Bryant et al., 1994, 1995). In this study, I name the unit that divides the C1 Sand reservoir into an upper C1U and lower C1L as the middle C1M (C1 middle).

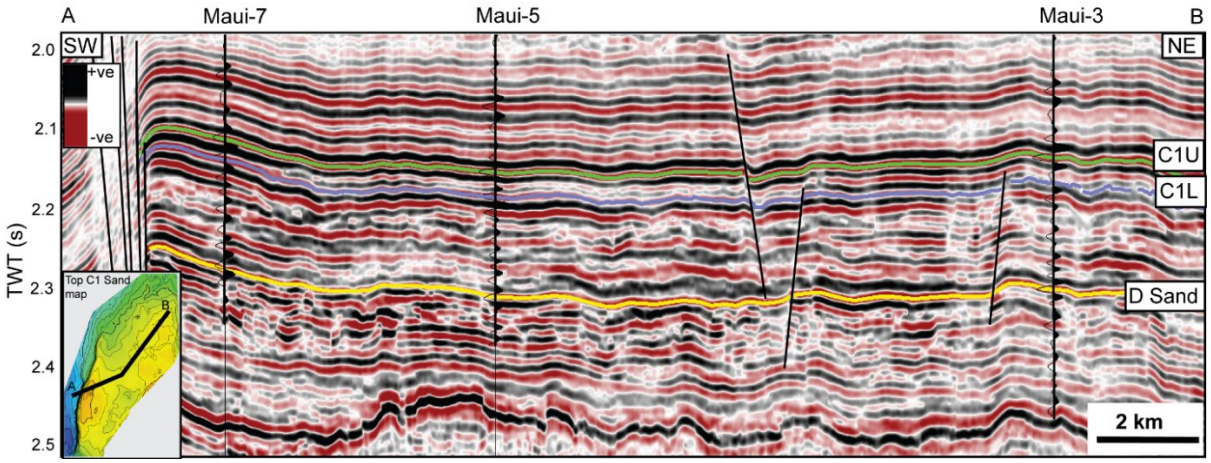

Figure 3. 2. A - B seismic line (location shown by black line in top C1 Sand time structure map) crosses Maui structure and pass through Maui-7, Maui-5 and Maui-3 wells. The black traces show synthetic traces genetrated for the three wells. This seismic line shows a thin shale layer (C1M) in Maui B area that is correlatable to carbonate cemented sand layer in Maui A that divides the C1U and C1L.

3.4 Dataset

A 3D pre-stack depth-migrated (PSDM) full-stack seismic volume, which is a merge of two seismic surveys, was made available for research purposes by the MBIE, New Zealand. The first 3D seismic survey covers 1000 km^2 and was acquired in 1991. The second seismic survey was acquired 2002 to cover 450 km^2 over the Maui A and Maui B regions (van der Veeken and Lutz, 2008). This study uses the 3D PSDM full-stack seismic volume in the seismic interpretation, attribute analysis, and machine learning analysis. The seismic data were processed by Shell Geoscience Solutions in the Netherlands. The depth migrated seismic volume was converted to time in the processing center then released by MBIE.

Eight vertical wells (Maui-1, Maui-2, Maui-3, Maui-5, Maui-6, Maui-7, Rahi-1, and MB-Z11) are located within the 3D survey. Each well has conventional logs (gamma-ray, density, neutron, sonic, and resistivity). Some core descriptions (Higgs et al., 2010), core photos and core measurements (Van Benten, 1986, 1987) are available for the Maui-5, Maui-6 and Maui-7 wells. The well logs of Maui-1 are compromised (highly washed out) and Rahi-1 has a missing logged interval close to the top of the C Sand reservoir. As a result, these wells were excluded from this study.

3.5 Methodology

Figure 3.3 shows the workflow used in this study. I perform petrophysical analysis for the Maui-2, Maui-3, Maui-5, Maui-6, Maui-7, and MB-11 wells to understand the reservoir properties and define the net reservoir intervals. To understand reservoir quality and divide the C1 Sand reservoir into distinct rock units, I performed rock typing analysis for four wells. In the rock typing analysis, I used core data from Maui-5, Maui-6 and Maui-7 and calculate effective porosity and predicted permeability for Maui-3. I used the Winland plot (Kolodzie, 1980) to divide the reservoir into different rock types. I used the rock quality index/flow zone indicator (RQI/FZI) approach developed by Amaefule et al. (1993) to classify the reservoir into different hydraulic units and then I followed the Gunter et al. (1997) graphical approach to upscale the various rock types to flow units.

The final processed PSDM merged seismic volume covers a total area of 1000 km^2 and was recorded to 3.5 s two-way time (TWT) at a 4 ms sample interval. However, the seismic data were interpolated to 2 ms to provide more samples for the SOM analysis. The data were then cropped laterally to cover an area of 410 km^2, and vertically to time range of 1.8 to 2.8 s TWT. I cropped the seismic volume to a smaller one in order to focus on the reservoir interval with in the Maui A and Maui B regions and to reduce computational time and space requirements. The seismic data were spectrally balanced during the 1991 and 2001 seismic volume merge (van der Veeken and Lutz, 2008).

However, the data are contaminated by random noise and acquisition artifacts. Thus, I followed Chopra and Marfurt's (2006) approach and applied a well-established principal component structure-oriented filtering (PC-SOF) along structural dip. This method enhances the signal aligned with the estimated dip and reduces the noise that crosses in other directions.

Obtaining accurate time/depth relationships for the wells in the interval of interest is fundamental for machine learning analysis of multiple seismic attributes at the sample level (Zhang et al., 2018; Sacrey and Sierra, 2020). I performed seismic-to-well ties for all six vertical wells included in this study. The seismic-to-well tie for Maui-7 well shows the low-impedance C1U and C1L sands along with their seismic picks (negative amplitude), which are separated by high-impedance C1M shale unit (positive amplitude) (Figures 3.1 and 3.2). The wavelet, extracted from the well log and seismic data is nearly zero phase. I used SEG standard display polarity where a decrease in impedance is negative.

I computed typical instantaneous and spectral decomposition attributes that are sensitive to reservoir properties and rock thickness in the C1 Sand reservoir level. These seismic attributes included the quadrature component, envelope, envelope slope, envelope second derivative, relative acoustic impedance, instantaneous frequency, thin bed, sweetness, instantaneous phase, normalized amplitude, and attenuation (Taner, 2001). Spectral decomposition attributes are computed using the continuous wavelet transform (Marfurt, 2018). As described later in this study, I used a visual analysis and principal component analysis (PCA) to select the best attributes for unsupervised self-organizing maps (SOM). The objective is to integrate the reservoir information from carefully selected seismic attributes into one clustered volume. This classification volume was calibrated to discrete net reservoir and flow units. The SOM-derived flow units can then be viewed in 3D (Figure 3.3).

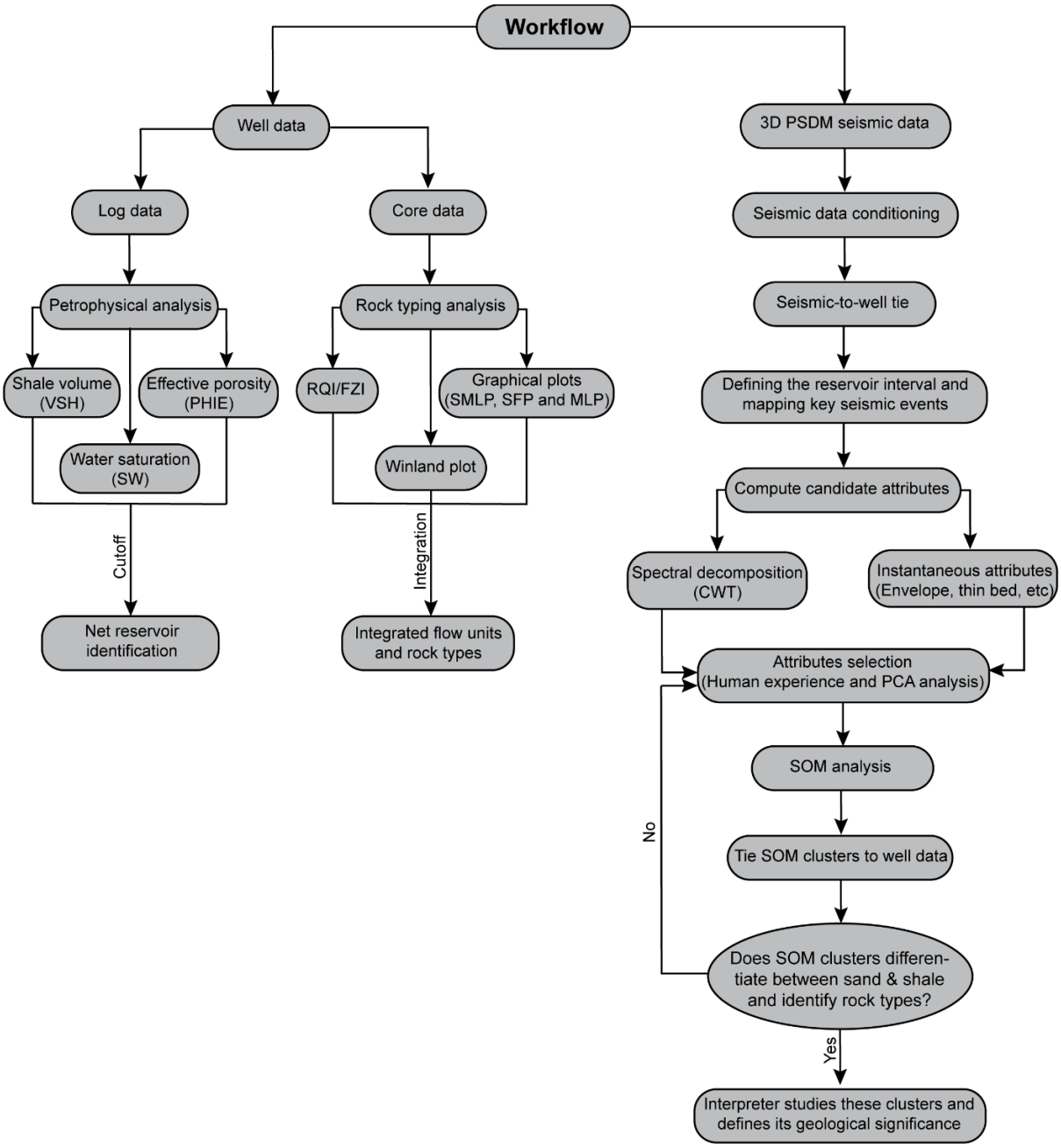

Figure 3. 3. Workflow for net reservoir discrimination and rock types identifications from well logs, core data, and 3D full stack seismic data. RQI - rock quality index; FZI - flow zone indicator; SMLP - stratigraphic modified Lorenz plot; SFP - stratigraphic flow profile; MLP - modified Lorenz plot; PSDM - prestack depth migrated; CWT - continuous wavelet transform; PCA - principal component analysis; SOM - self-organizing maps.

3.6 Petrophysical characteristics of the C sand reservoir

It is essential to calculated and analyze the basic petrophysical logs to understand the reservoir characteristics. I calculated the shale volume (VSH) log from the gamma ray (GR) and effective porosity (PHIE) from the density log for the entire reservoir except for the gas-charged interval. To avoid the gas effect, the effective porosity was calculated from the density-neutron logs in the hydrocarbon-charged reservoir zones and then the calculated PHIE was calibrated to the core-measured porosity (CORE PHI). The water saturation (SW) was calculated using the Indonesia saturation model. To determine the net reservoir intervals, petrophysical cut-offs of 0.45 and 0.1 are used for VSH and PHIE, respectively.

As an example, Figure 3.1 shows the petrophysical logs calculated for the Maui-7 well, which penetrated the Maui B region. Table 1 summaries the petrophysical properties of the C1 sand based on the analyses performed at Maui-3, Maui-5, Maui-6, and Maui-7 wells. Maui-3 is located in the northern part of the Maui A region. Maui-3 encountered more sandy intervals of the C1 reservoir compared to Maui-5, (which penetrated the saddle between the Maui A and Maui B regions), Maui-7 and Maui-6 (which drilled in the far distal part of the field). The C1U and C1L are considered the main producing units of the C1 Sand reservoir. The thickness of the C1U ranges between 15.7 and 27 m whereas the C1L's thickness varies between 20.1 and 31.7 m (Table 3.1).

Table 3. 1. Petrophysical properties summaries of C1 reservoir for four Maui wells

Well	Interval	Thickness (m)	Mean VSH (%)	Mean PHIE (%)	Net Res/Gross (%)
Maui-3	C1U	27	15.8	16.7	85.3
	C1M	18.6	16.6	17.1	63.1
	C1L	30.9	17.1	16	83.3
Maui-5	C1U	15.7	19.6	17.8	100
	C1M	42	32.4	16.8	56.7
	C1L	21.3	4.7	21.8	100
Maui-7	C1U	26.8	27.2	14.4	81.3
	C1M	24.7	40.1	11.6	21.1
	C1L	31.7	7.2	18.2	80.3
Maui-6	C1U	16.3	31.6	12.2	47.7
	C1M	13.1	36.5	4.8	0
	C1L	20.1	42.2	16.5	7.6

In Maui-3, the C1U seems to be more sandy (VSH = 15.8 %) and has slightly better porosity (PHIE = 16.7 %) compared to the C1L (VSH = 17.1 % and PHIE = 16 %). However, in the Maui-5 and Maui-7 wells, the C1L seems to be more sandy (VSH = 4.7 % and 7.2 % respectively) and shows higher porosity (PHIE = 21.8 % and 18.2 % respectively) compared to the C1U (VSH = 19.6 % and 27.2 % and PHIE = 17.8 % and 14.4 % respectively). The Maui-6 well penetrated a mostly shaley interval of the C1 reservoir with VSH = 13.6 for the C1U and 42.2 % for the C1L (Table 3.1). This suggests that the C1U has better quality reservoir properties (lower VSH and higher PHIE) compared to C1L in the Maui A region. In the saddle between the Maui A and Maui B regions and in Maui B, the C1L has better reservoir properties compared to C1U.

3.7 Seismic attribute selection

Unsupervised machine learning clustering techniques are useful for integrating the geological content of multiple seismic attributes. However, selecting the right attributes to be used as inputs to clustering algorithms significantly controls the classification results (Barnes and Laughlin, 2002; Zhao et al., 2015). In this study, I focus on seismic attributes that are sensitive to reservoir thickness and rock properties such as instantaneous attributes and spectral decomposition attributes. Instantaneous attributes are defined as time-frequency attributes, which are computed sample by sample on the real and quadrature components of the analytic seismic trace (Taner, 2001; Chopra and Marfurt, 2007). Spectral decomposition attributes measure time-varying spectral properties of the seismic data. These spectral properties include spectral magnitude components, spectral voice components, peak frequency, peak magnitude, tuning frequency, and spectral bandwidth (Barnes, 2016; Marfurt, 2018).

Initially, I generated fifteen instantaneous attributes and performed spectral decomposition analysis using the continuous wavelet transform (CWT) algorithm at the reservoir interval for a frequency range of 20 Hz to 70 Hz with a 5 Hz interval. Visual analysis of the individual attributes indicates that the reservoir tuning frequency lies in 30-to-50 Hz range (Figure 3.4). Thus, I run the spectral decomposition analysis again for a 30-to-50 Hz range with a 2 Hz interval. However, visually analyzing the resultant spectral components to determine which spectral bands contain the most information about the reservoir is challenging. Thus, I turn to statistical algorithms to enable the selection of the spectral frequency that best represents the reservoir tuning frequency.

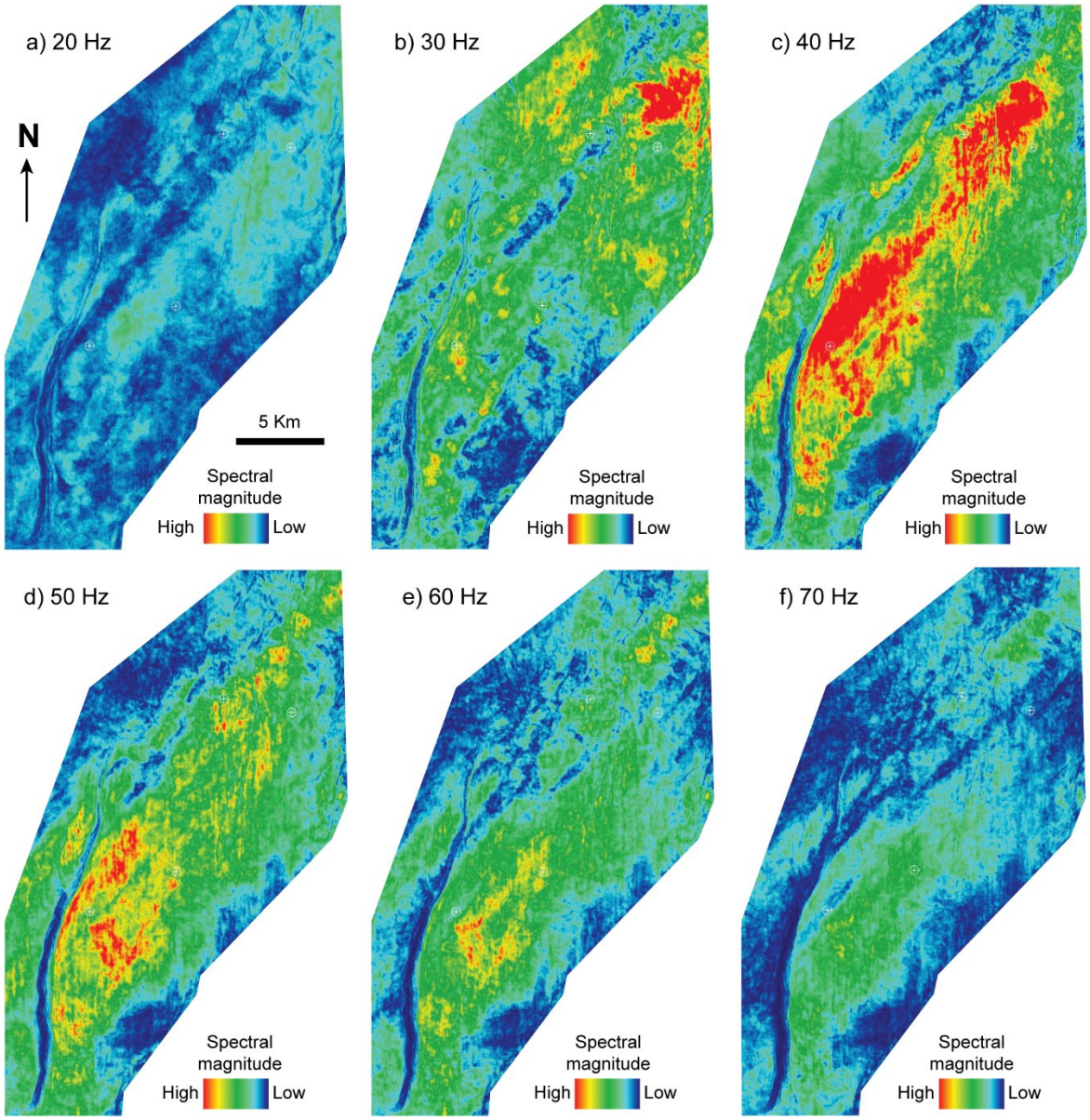

Figure 3. 4. Horizon slices along the top of the C1U reservoir extracted from spectral magnitude components volumes. Note, the reservoir tune in spectral slices b) to d).

Principal component analysis (PCA) is a linear statistical technique that can distill a large library of seismic attributes into a smaller set of seismic attributes based on the relative variance of the attributes within the interval of interest (Roden et al., 2015). I conduct PCA analysis on 11 spectral voices (frequency bands), which are generated using spectral decomposition from 30-to-50 Hz in a window 10 ms above to 70 ms below the mapped C1U reservoir horizon. Investigating the PCA results, I found that the 38 Hz spectral voice is the top ranked attribute in the 1st eigenvector with a 9.34% percent contribution. This indicates that the 38 Hz spectral voice accounts for most of the variance within the data and is close to the tuning frequency of the reservoir. Thus, I compute 15 instantaneous attributes from the 38 Hz spectral voice and in Figure 3.5, compare three of those attributes with the ones calculated from the original preconditioned broadband seismic volume using horizon slices extracted along the top C1U reservoir.

The amplitude slice (Figure 3.5a) extracted from the broadband seismic volume shows a high continuous negative amplitude event that might be interpreted as a continuous sandy facies. The sweetness attribute is defined as the ratio of the trace envelope to the square root of the instantaneous frequency. It helps to differentiate between sand and shale and highlights sweet spots associated with hydrocarbon-charged sand (Oliveros and Radovich, 1997; Hart, 2008). The sweetness slice (Figure 3.5b) shows high, sweetness values across the central parts of Maui A and Maui B that indicate a sandy facies. Low, sweetness values at the margins of Maui A and Maui B likely indicate a more shaley lithology.

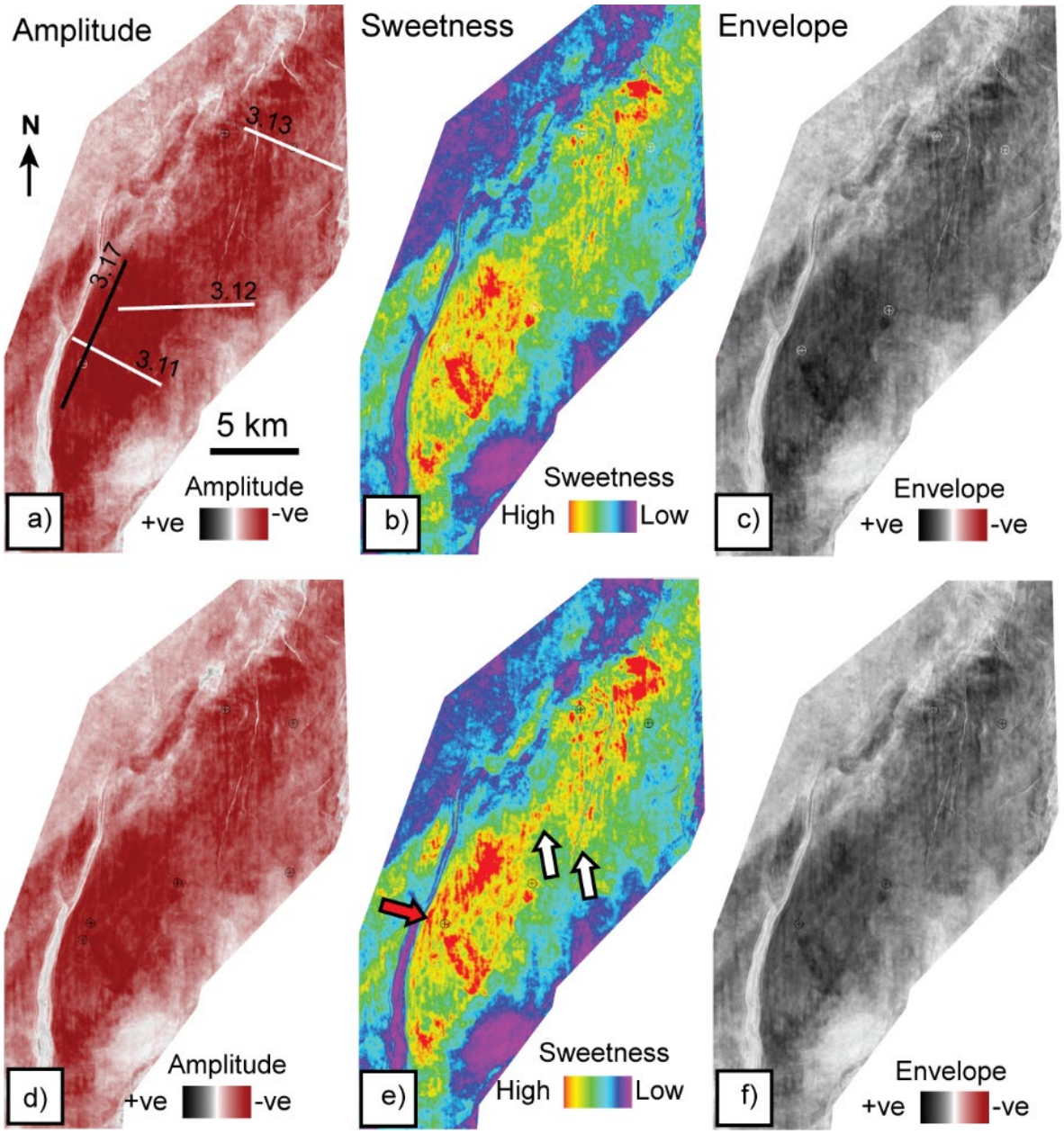

Figure 3. 5. Comparison between horizon slices extracted along the C1U reservoir seismic amplitude and instantaneous attributes calculated from the preconditioned broadband seismic volume (a to c) and amplitude and instantaneous attributes computed from 38 Hz spectral voice (d to f). White and red arrows indicate channelized features and sheet-like facies which are better imaged by spectral sweetness compared to broadband sweetness slice. Circles with crosses show the vertical wells used in this study. The lines shown in a) display the locations of vertical sections of Figures 3.11, 3.12, 3.13 and 3.17.

The envelope (called instantaneous amplitude and reflection strength in other publications) describes the vector length of the real and imaginary parts of the seismic trace (Taner, 2001). The envelope slice (Figure 3.5c) shows a continuous positive amplitude with larger amplitude values observed in the Maui A and Maui B regions that might indicate porous sands. Low-envelope values were observed in the northwest and southeast parts of the field that could be interpreted as shelfal mudstones.

I now compare the amplitude (Figure 3.5a) and instantaneous attribute slices (Figures 3.5b to 3.5c) computed from the broadband seismic volume to those same attributes (Figures 3.5d to 3.5f) calculated from the 38 Hz spectral voice volume. In general, the attributes produced from the 38 Hz spectral voice data show more detail than those calculated from the broadband data. The 38 Hz spectral voice amplitude slice (Figure 3.5d) showed subtle lateral changes in amplitude that might indicate changing seismic facies. In contrast, the broadband amplitude slice (Figure 3.5a) showed little change in seismic amplitude between Maui A and Maui B, suggesting relatively homogeneous seismic facies.

The spectral sweetness slice (Figure 3.5e) did a better job showing the channelized sand-filled features observed in the Maui A region and the saddle area (white arrows). Sheet-like sandy facies in Maui B (red arrow in Figure 3.5e) were better illuminated in the spectral data compared to the broadband sweetness slice (Figure 3.5b). Similarly, a slight improvement was observed in the spectral envelope attribute (Figure 3.5f) which showed small changes in the envelope values within the Maui A and Maui B regions suggesting subtle facies changes. These small changes were less obvious on the broadband envelope image (Figure 3.5c). Therefore, spectral instantaneous attributes are considered useful candidate attributes for machine learning analysis.

3.8 SOM for net reservoir discrimination and rock type identification

The Self-Organizing Map (SOM) is a powerful unsupervised machine learning technique that can efficiently combine the geological information from multiple seismic attribute volumes and thus, reduces the data dimensionality (Zhao et al., 2015; Marfurt, 2018). SOM uses a nonlinear unsupervised neural network, which is sensitive to subtle changes within the data. SOM performs a sample-based investigation of the various input seismic attributes in a multi-dimensional-attribute space (Coléou et al., 2003; Roy, 2013). The data points in multi-dimensional attribute space are normalized to the same scale and neurons adapt to the data identifying natural patterns and clusters. Using a 2D topology map, SOM groups or clusters similar data together into one clustered volume. The user can control the number of natural clusters based on the predefined number of neurons within the 2D map (Kohonen, 1982; Matos et al., 2006). SOM clusters can be related to changes in the subsurface geology or stratigraphy within the interval of interest (Roy et al., 2011).

The attribute selection and SOM workflow used in this study are shown Figure 3.6. To select the attributes for SOM analysis, I visually analyzed the 15 spectral instantaneous attributes. I also applied a PCA analysis for the reservoir interval and select those attributes that are prominent in the first three eigenvectors. Combining the two analyses, I selected instantaneous frequency, thin bed, quadrature component, relative acoustic impedance, sweetness, envelope, attenuation, and cosine of instantaneous phase attributes as input for unsupervised machine learning analysis.

The SOM analysis was applied to these attributes within the interval of interest – 10 ms above to 70 ms below the top of the C1 Sand reservoir. First, the SOM neurons (called prototype vectors in other publications) were trained at the seismic sample scale to gather similar data within the eight-dimensional attribute space into distinct natural clusters. Then, the trained winning neurons classified all the multi-attribute seismic samples within the area of interest and project those natural SOM clusters into one classification volume.

One of the challenges of this SOM approach is that the appropriate number of natural clusters within the interval of interest is unknown. Thus, instead of forcing the SOM analysis to consider a fixed number of clusters or classes, I allowed the data to identify the numbers of clusters using different SOM classifications with various topologies such as 5x5, 6x6, 7x7, 8x8, 9x9, 10x10, and 12x12. The SOM classification volumes are then correlated to the well data to select the SOM volume that was best tied to the well logs. I found that coarse-grid topologies like 5x5 tend to amalgamate different natural clusters that correlated to various lithological facies. Very fine-grid topologies such as 12x12 tend to break down natural clusters into smaller pieces which were difficult to interpret. Based on our well ties to SOM classifications volumes, I found that the 8x8 topological SOM with 64 winning neurons best correlates to log data at the well locations.

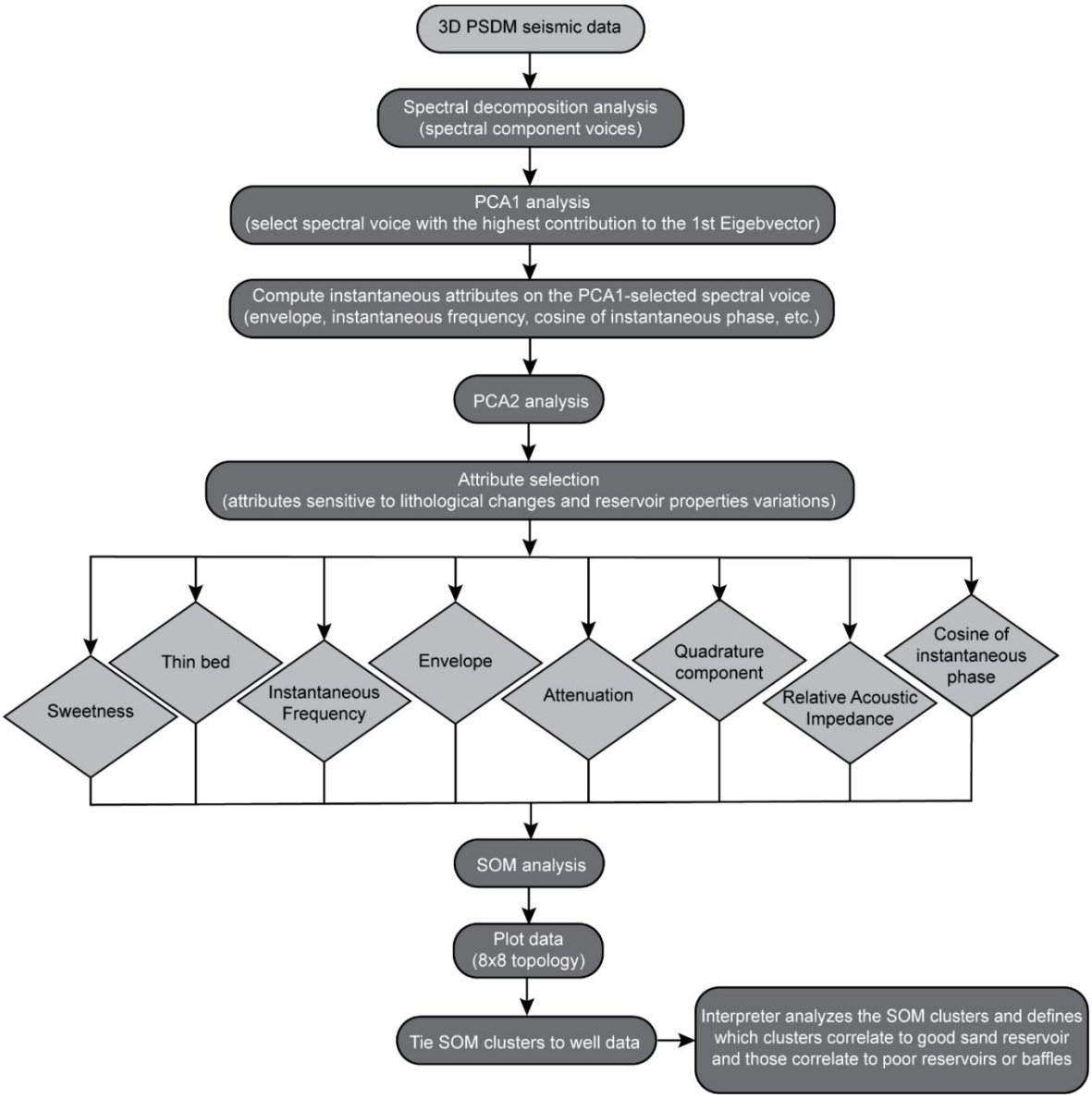

Figure 3. 6. Proposed workflow to cluster and integrate data from eight spectral instantaneous seismic attributes by using PCAs and SOMs for net reservoir discrimination and rock types identification. PSDM - prestack depth-migrated seismic; PCA - principal component analysis; SOM - self-organizing maps.

3.9 SOM for net reservoir discrimination

Similar to wiggle displays of seismic amplitude, SOM natural clusters of seismic attributes do not have explicit geological meaning on their own. They simply show patterns within the input seismic attribute volumes that can be correlated to geology. Therefore, I assigned geological meaning to SOM clusters by correlating those SOM clusters to well data. As previously noted, this requires accurate time/depth relationships, which were calibrated with synthetic seismograms and the seismic-to-well tie process.

Figure 3.7 shows an enlargement of the SW-NE arbitrary line shown in Figure 3.2 with the SOM classification results co-rendered with seismic amplitude data (wiggle traces). Also shown are net reservoir logs for three of the Maui wells as defined from the petrophysical analysis. The SOM classification results tie with the net reservoir logs and show more detailed variations compared to the original seismic data.

As I mentioned previously, the C1M in Maui B is composed of a thin shale layer (i.e., seismic peak) that divides the C1 sand reservoir into C1U and C1L. In Maui A, the C1M is composed of carbonate cemented sand. In the saddle area between Maui A and Maui B, the C1M consists of silty shale. Note that the SOM clusters at the Maui-7 well location are different than the clusters at Maui-5 which are different than those at Maui-3. This suggests the reservoir is heterogeneous and that the reservoir sands and shales deposited in Maui A and Maui B might be different.

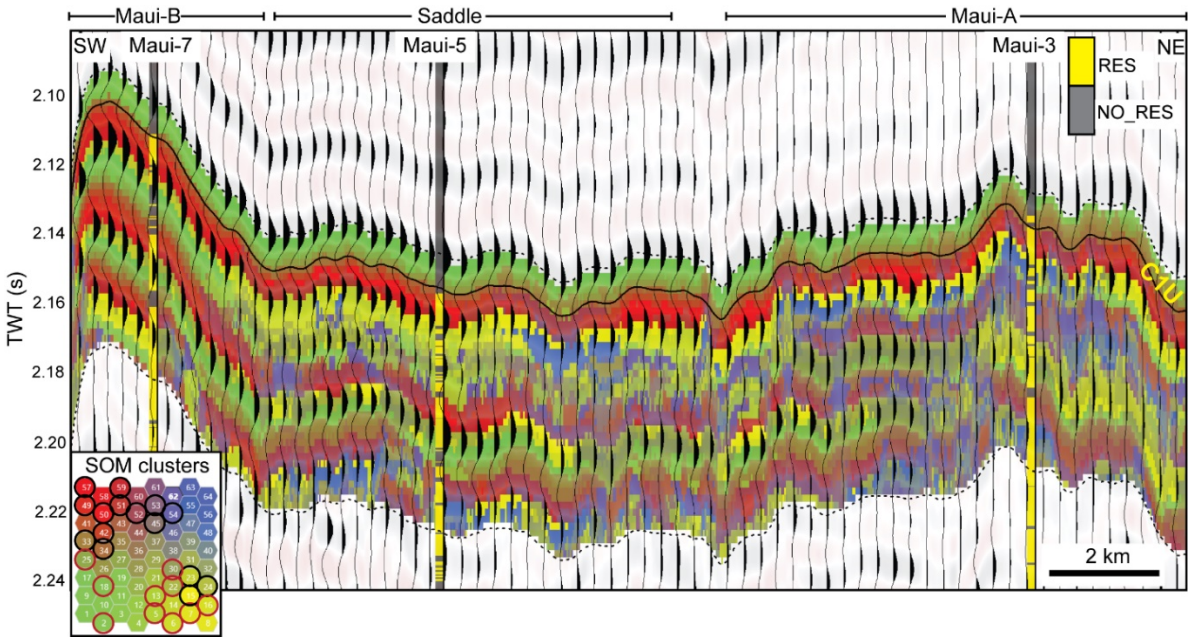

Figure 3. 7. Enlarged SW-NE arbitrary line of Figure 3.2 shows the SOM classification results co-rendered with seismic amplitude data (wiggle traces) and net reservoir discrete logs at the Maui wells. The neurons in circled in black in the SOM 2D colored legend indicate clusters correlated to net sand reservoir whereas the ones circled in red indicate clusters that are correlated to shales. The sold black horizon indicates the top of the C1 Sand reservoir, the top and bottom dash-horizons indicate 10 ms and 70 ms shifted horizons from the top of C1 Sand reservoir.

Visually comparing the SOM clusters to the well data in Figure 3.7 shows that some clusters/neurons (namely N15, N23, N24, N33, N34, N42, N45, N49, N50, N51, N52, N53, N54, N57 and N59) are correlated to net reservoir sands and other clusters (N2, N5, N6, N7, N13, N16, N18, N22, N25, and N30) are correlated to shales and silty shale (Figure 3.7). Also, the clusters correlated to the net reservoir sand in Maui A (the Maui-3 well) are different from those clusters defined in Maui B (Maui-7 well) and the saddle (Maui-5 well) (Figure 3.7). This suggests that the SOM classification may be sensitive to rock properties within the sand that the usual petrophysical analysis is not able to identify.

To better understand reservoir heterogeneity and subdivide the C1 reservoir into distinct petrophysical flow units, I applied advanced rock typing analysis on core and wireline log data. This allows us to interpret the SOM clusters and results in the definition of good quality reservoir versus baffles in 3D instead of being bound to the 1D analysis at the well locations.

3.10 Rock typing analysis

Rock typing describes the process of assigning reservoir properties to depositional facies (Tavakoli, 2018). Over the years, many rock typing approaches have been developed with different degrees of complexity (Winland, 1972; Kolodzie, 1980; Amaefule et al., 1993; Gunter et al., 1997; Stolz and Graves, 2003; Francesconi et al., 2009; Kharrat et al., 2009; Tavakoli, 2018). For this study, I choose the widely used rock typing methods developed by Winland (1972), Amaefule et al. (1993) and Gunter et al. (1997).

Table 3. 2. R35 rock type classification of the C1 Sand reservoir based on Martin et al., 1997 R35 classification scheme and Winland crossplot

Rock type (RT)	**R35 (µm)**	**Mean R35**	**Pore system**
RT1	R35 >10	39.8	Mega-porous
RT2	2.5 < R35 ≤ 10	4.8	Macro-porous
RT3	0.5 < R35 ≤ 2.5	1.3	Meso-porous
RT4	0.2 < R35 ≤ 0.5	0.35	Micro-porous
RT5	R35 ≤ 0.2	0.09	Nano-porous

Based on the regression analyses of 322 sandstone samples and 35 % mercury saturation, Winland (1972) developed an empirical relationship between the pore-throat size and porosity and permeability. The Winland equation was published by Kolodzie (1980):

$$\text{Log R35} = 0.732 + 0.588 * \text{Log } K_{air} - 0.864 * \text{Log } \phi_{CORE}, \quad (1)$$

where R35 represents the calculated pore-throat radius (micron) at 35 % mercury saturation in a mercury injection test, Kair is the air permeability (mD) and ϕCORE is the core porosity (%). I used the Winland semi-log plot of permeability versus porosity with R35 isopore throat size (Figure 3.8a) for the cored wells (Maui-5, Maui-6, and Maui-7) and follow the Martin et al. (1997) R35 classification scheme. The C1 Sand reservoir can be divided into 5 rock types (RT), which change from mega-porous to nano-porous facies with pore throat radii (R35) varying from means of 39.8 to 0.09 μm (Table 3.2).

Amaefule et al. (1993) introduced a classification method by modifying the Kozeny-Carman equation. Their experiments show that the ratio of permeability to effective porosity can express the reservoir hydraulic behavior. They defined the rock quality index (RQI) and flow zone indicator (FZI) as follows:

$$\text{RQI } (\mu m) = 0.0324 * (K / \Phi)^{0.5}, \quad (2)$$

$$\text{FZI} = \text{RQI} / \phi_z;\ \phi_z = \phi / (1 - \phi), \quad (3)$$

where K is permeability (mD), ϕ is porosity (fraction) and ϕz is the ratio of pore volume to grain volume (fraction).

Following the Amaefule et al. (1993) approach and the Sritongthae (2016) FZI classification scheme, the C1 Sand reservoir can be divided into five hydraulic flow units or rock types (RT) (Figure 3.8b), which change from very good to very poor reservoir quality facies with mean values of FZI ranging from 16.3 to 0.28 (Table 3.3). A box and whisker plot (Figure 3.8c) summarizes the core porosity and permeability statistics for the FZI/RQI-based rock types using all of the cored wells available for this study. The plot displays a wide range of porosity and permeability for the five defined RTs. The median core porosity is above 15 % for all of the RTs except RT5, but the permeability varies significantly. RT1 has the best reservoir quality with a mean porosity of 20.6% and a permeability of 4034 mD. RT5 is the worst reservoir quality rock type with a mean porosity of 9.7 % and a permeability of 0.22 mD. Although the R35 and RQI/FZI methods are useful for defining the rock types and understand the reservoir quality, these approaches result in very thin units that are not easily correlated to SOM classification results or used in the reservoir simulation work.

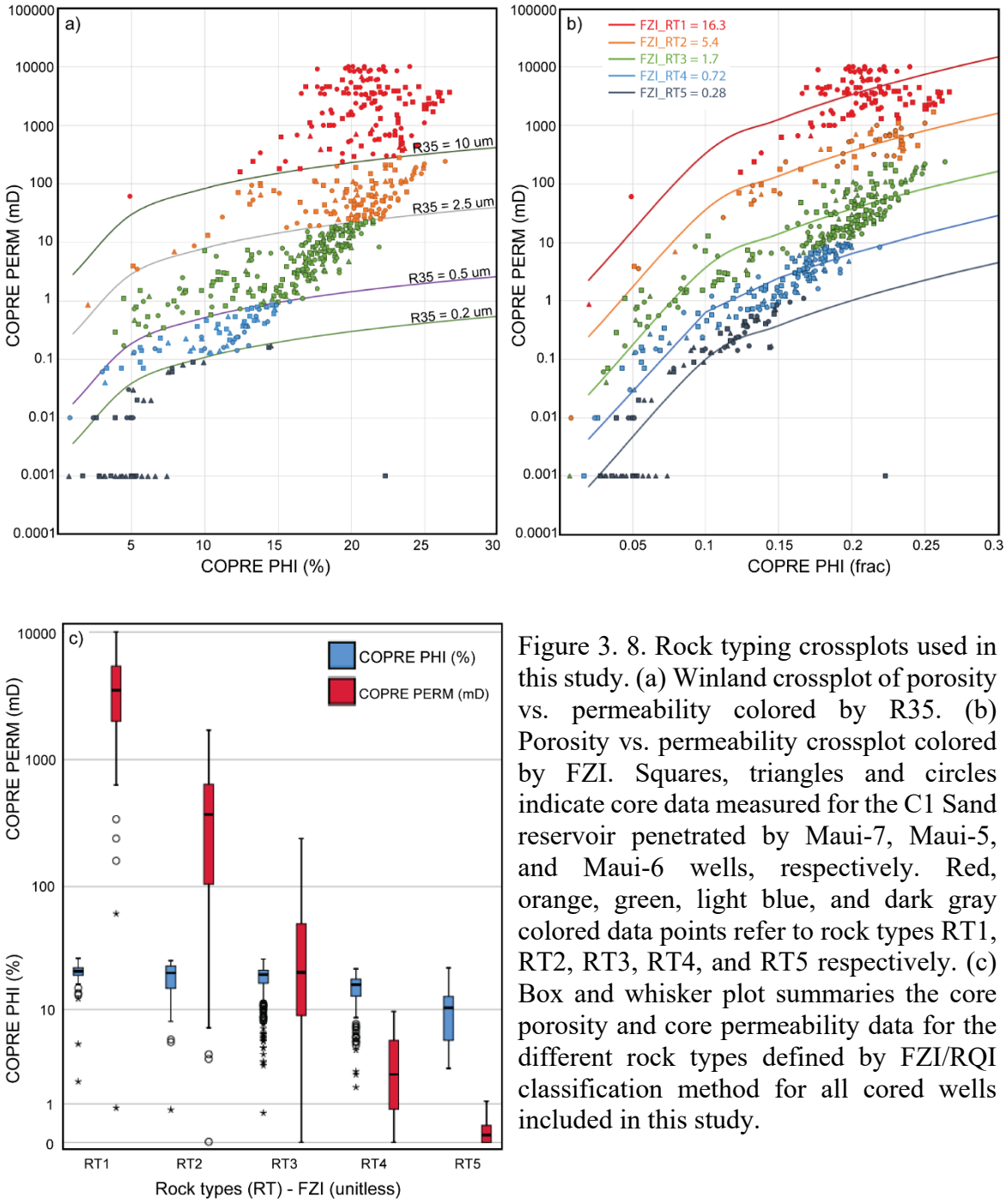

Figure 3. 8. Rock typing crossplots used in this study. (a) Winland crossplot of porosity vs. permeability colored by R35. (b) Porosity vs. permeability crossplot colored by FZI. Squares, triangles and circles indicate core data measured for the C1 Sand reservoir penetrated by Maui-7, Maui-5, and Maui-6 wells, respectively. Red, orange, green, light blue, and dark gray colored data points refer to rock types RT1, RT2, RT3, RT4, and RT5 respectively. (c) Box and whisker plot summaries the core porosity and core permeability data for the different rock types defined by FZI/RQI classification method for all cored wells included in this study.

Table 3. 3. FZI rock type classification of the C1 Sand reservoir based on Sritongthae 2016 classification scheme

Rock type (RT)	**FZI**	**Mean FZI**	**Reservoir quality**
RT1	FZI > 8.0	16.3	Very good
RT2	3.5 < FZI ≤ 8.0	5.4	Good
RT3	1.0 < FZI ≤ 3.5	1.7	Moderate
RT4	0.45 < FZI ≤ 1.0	0.72	Poor
RT5	FZI ≤ 0.45	0.28	Very poor

Gunter et al. (1997) developed a graphical workflow that aids in identifying the reservoir flow units according to the geologic framework, petrophysical rock types, storage capacity, flow capacity, and reservoir process speed (K/PHI). This approach allows us to upscale the R35 and RQI/FZI defined rock types to flow units, which can then be correlated to SOM classifications. This approach includes three main plots:

- Stratigraphic Modified Lorenz Plot (SMLP): percent flow capacity (permeability * thickness) versus percent storage capacity (porosity * thickness).
- Modified Lorenz Plot (MLP): percent flow capacity versus percent storage capacity that is calculated on a flow unit basis and preserves the stratigraphic positions.
- Stratigraphic Flow Profile (SFP): a well section display of wireline lithological or GR log, a generalized core description, porosity, permeability, R35, K/PHI, storage capacity and flow capacity.

I applied the Gunter et al. (1997) graphical approach to the core data of the Maui-7, Maui-6 and, Maui-5 wells. Unfortunately, no core data is available for Maui-3 well or any other well in the Maui A region. As a result, a porosity-permeability model derived from the cored wells was applied to the Maui-3 PHIE log to predict the permeability in that well.

Figure 3.9 shows the SMLP and MLP created for the Maui-7, Maui-5 and, Maui-3 wells. The shape of the SMLP for the C1 Sand is different for each of the wells. This suggests different reservoir performance characteristics and indicates that the C1 Sand reservoir is heterogeneous. Preliminary flow units (FU) are defined based on the deflection points from straight-line segments within the SMLP. These flow units are validated using SFP and MLP. Steep slope segments indicate intervals with larger flow capacity compared to storage capacity. Thus, these intervals suggest a high-reservoir process speed (high-speed flow units). Normal slope segments were defined as normal reservoir with high or equal values of storage capacity and flow capacity flow units. Flat segments were defined as baffles (intervals that throttle fluid movements) that have storage capacity but little flow capacity (Gunter et al., 1997; Rahimpour-Bonab et al., 2014; Riazi, 2018).

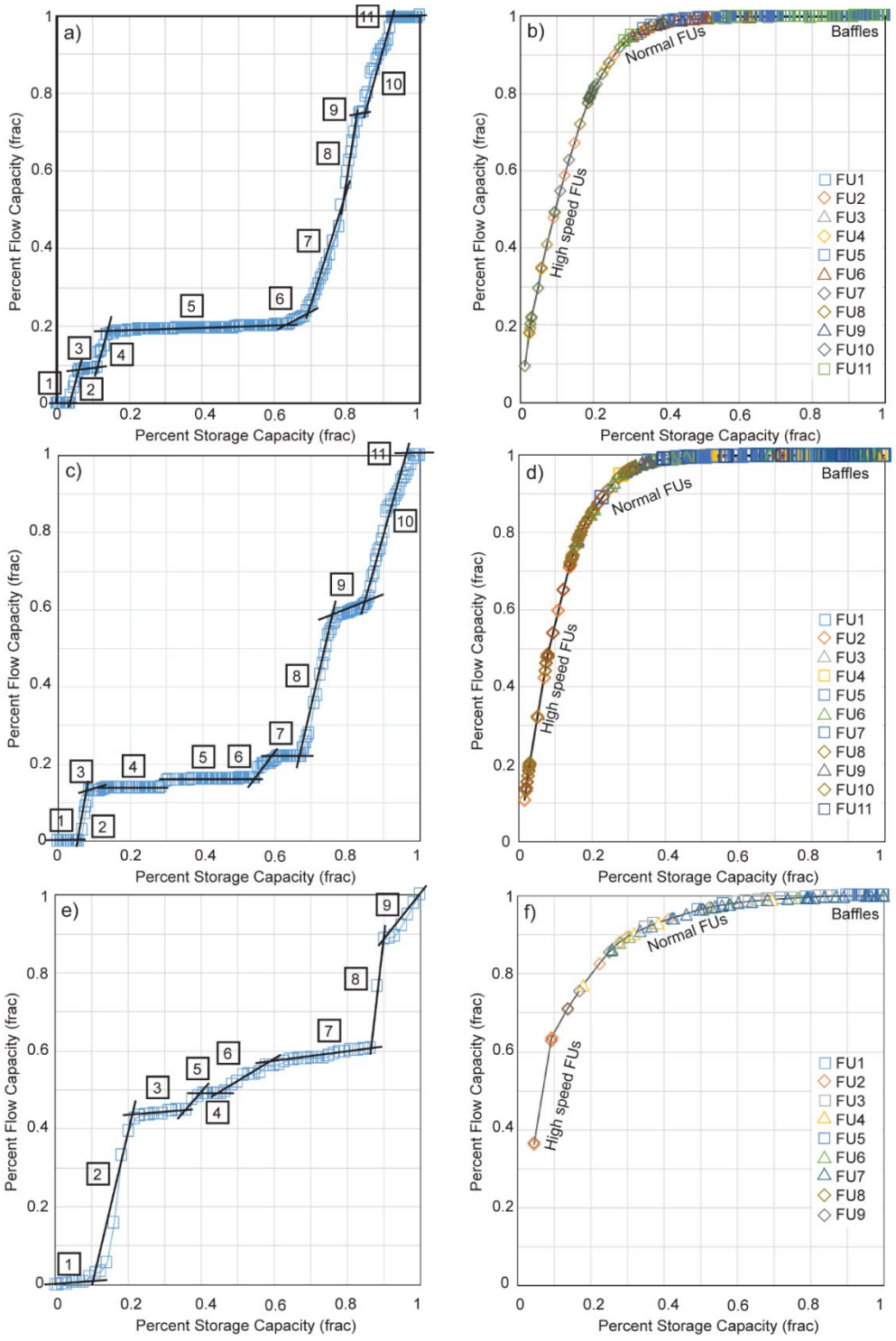

Figure 3. 9. Graphical rock typing plots for the C1 Sand reservoir. Stratigraphic Modified Lorenz plot (SMLP; left) and Modified Lorenz Plot (MLP) established for Maui-7 (a, b), Maui-5 (c, d) and Maui-3 (e, f). The SMLP indicate the flow behavoir of the C1 Sand reservoir and show the various flows units of the reservoir. MLP is used to refine the preliminary flow units defined on SMLP.

The SMLP for the Maui-7 well (Figure 3.9a) suggests that the C1 Sand reservoir is divided into 11 FUs. Validating these FUs using the MLP (Figure 3.9b) and SFP (Figure 3.10a) indicates that FUs 2, 4, 7, 8, and 10 are high-speed units that cumulatively account for 93% of the flow capacity and 35% of the storage capacity. These high permeability flow units are composed of estuarine/distributary channels with minor upper shoreface sands of RT1 as based on the R35 and RQI/FZI classifications. FUs 3, 6 and, 9 are normal flow units contributing to about 5% of the flow capacity and 20% of the storage capacity. These FUs consist mainly of mouth bar, shoreline barrier and minor estuarine/distributary channels of RT2 and RT3 as based on the R35 and RQI/FZI classifications. FU3 tends to have very low or no flow capacity because of high-shale content. FUs 1, 5, and 11 are baffles with almost no flow capacity and collectively contribute to 45% of the storage capacity. These baffle FUs consist of shaley sand, silty shale and, shale facies (Figure 3.10a). These zones tend to have very low flow capacity when they become sandy or silty. Note that there are missing core measurements for thin intervals within the C1U and C1L limited the analysis (I assumed that the sands are interpreted as FU4 and FU10 are homogeneous sands with high porosity and permeability).

The SMLP for the Maui-5 well (Figure 3.9c) suggests that the C1 Sand reservoir is divided into 11 FUs. Refining these FUs using MLP (Figure 3.9d) and SFP (Figure 3.10b) indicates that FUs 2, 8, and 10 are high-speed reservoir flow units contributing to 97% of the flow capacity and 30% of the storage capacity. These high permeability units consist mainly of marginal marine channel and estuarine/distributary channel of RT1, according to R35 and RQI/FZI classifications. FUs 3, 6, and 9 are normal reservoir flow units with an average flow capacity of 3% and a storage capacity of 40%. These normal reservoir intervals consist of marginal, tidal, estuarine channels with minor tidal flat of RT1, RT2, and RT3. FUs 1, 4, 5, 7, and 11 are baffles that cumulatively account for 30% of storage capacity and almost none of the flow capacity.

Figure 3. 10. Stratigraphic flow profile (SFP) for the C1 Sand reservoir penetrated by (a) Maui-7, (b) Maui-5 and (c) Maui-3 wells. Tracks from left to right display measured depth (MD), Gamma ray (GR), Caliber (CALI), Bit size (BS), Core porosity (CPHI), Effective porosity (PHIE), Core permeability (CKair), Predicted permeability (K_pred), Pore throat radius (R35), Rock quality index (RQI), Flow zone indicator (FZI), Storage capacity (%PHIH), Flow capacity (%KH), Reservoir process speed (K/PHI), Net reservoir flag (FLAG) and Flow units (FU).

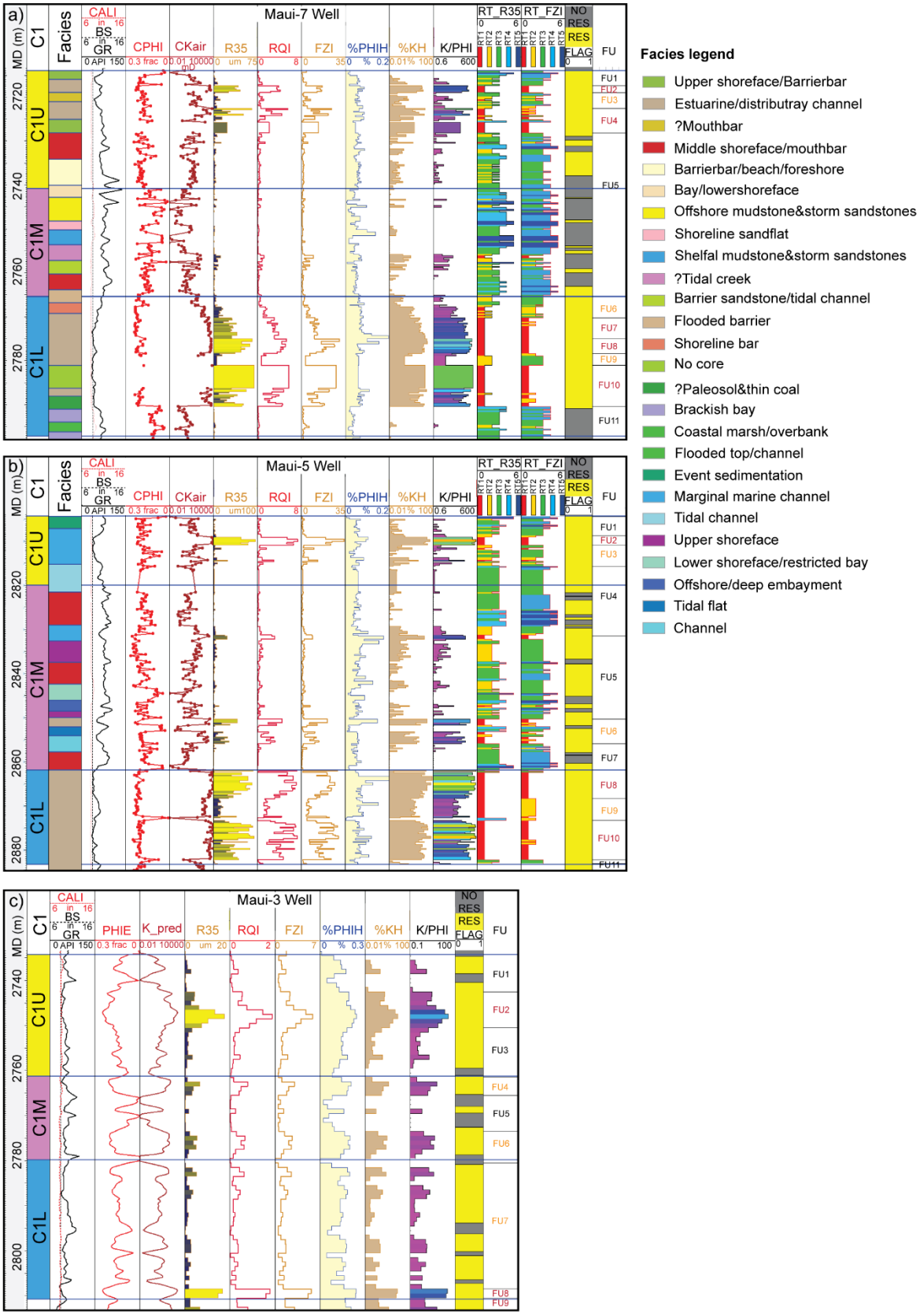
a)
Maui-7 Well
MD (m)
C1
Facies
CALI
BS
GR
CPHI
CKair
R35
RQI
FZI
%PHIH
%KH
K/PHI
RT_R35
RT_FZI
NO RES
RES
FLAG
FU
C1U
C1M
C1L
FU1
FU2
FU3
FU4
FU5
FU6
FU7
FU8
FU9
FU10
FU11
b)
Maui-5 Well
c)
Maui-3 Well
PHIE
K_pred
Facies legend
Upper shoreface/Barrierbar
Estuarine/distributray channel
?Mouthbar
Middle shoreface/mouthbar
Barrierbar/beach/foreshore
Bay/lowershoreface
Offshore mudstone&storm sandstones
Shoreline sandflat
Shelfal mudstone&storm sandstones
?Tidal creek
Barrier sandstone/tidal channel
Flooded barrier
Shoreline bar
No core
?Paleosol&thin coal
Brackish bay
Coastal marsh/overbank
Flooded top/channel
Event sedimentation
Marginal marine channel
Tidal channel
Upper shoreface
Lower shoreface/restricted bay
Offshore/deep embayment
Tidal flat
Channel

The SMLP for the Maui-3 well (Figure 3.9e) suggests that the C1 Sand reservoir can be divided into 9 FUs. FUs 2, 8 and, 9 are high-speed reservoir flow units collectively accounting for 90% of the flow capacity and 30% of the storage capacity (Figures 3.9f and 3.10c). FUs 4, 6, and, 7 are normal reservoir flow units accounting for 8% of the flow capacity and 30% of the storage capacity. FUs 1, 3, and 5 are baffles with less than 2% of the flow capacity and 40% of the storage capacity. Furthermore, the C1U reservoir seems to have better reservoir quality compared to C1L in the Maui A region. However, in the Maui B region and in the saddle between Maui A and Maui B, C1L sands have better reservoir quality (RT1 and RT2) compared to C1U sands. This suggests that the C1 Sand reservoir is quite heterogeneous with wide variations in the reservoir properties across the Maui field.

3.11 SOM-derived petrophysical flow units

The flow units derived at the well locations have thicknesses that vary from 2 m to 37 m. These units are thick enough to correlate with the SOM classification volume. Some SOM clusters correlate well to high-speed and normal reservoir flow units. Other SOM clusters correlate to poor reservoir quality reservoir or thin stratigraphic baffles. Viewing the SOM-derived flow units using vertical and 3D visualization tools aids in understanding reservoir quality and heterogeneity and in identifying stratigraphic baffles. Figures 3.11 to 3.13 show vertical sections of the SOM classification co-rendered with seismic amplitude (wiggle traces) and overlain by discrete logs of net reservoir and flow unit at three Maui wells. The NW-SE arbitrary line crossing the Maui B region and the Maui-7 well (Figure 3.11) shows that SOM clusters N33, N41, and N49 are correlated to high-speed and normal reservoir flow units (FU2, FU3 and FU4) and N17 correlates to a baffle (FU1) in the C1U interval.

The SOM classification volume shows greater granularity compared to Gunter et al. (1997) approach used in this study to identify flow units. The SOM classification result breaks down the baffle flow unit (FU5) into clusters (N49 and N57) that correlate well to more sandy units within FU5 and other clusters (N16, N2, N18, N25, and N35) that correlate to the shale within FU5. In the C1L interval, N34, N42, N59, and N24 show good correlation to high-speed and normal reservoir flow units (FU6, FU7, FU8, FU9, and FU10) and N19 correlates to a baffle (FU11). This method also shows that the SOM-derived reservoir flow unit clusters in the C1U interval extend towards the southeast (Maui A region) whereas the C1L SOM-derived reservoir clusters pinch-out towards the southeast.

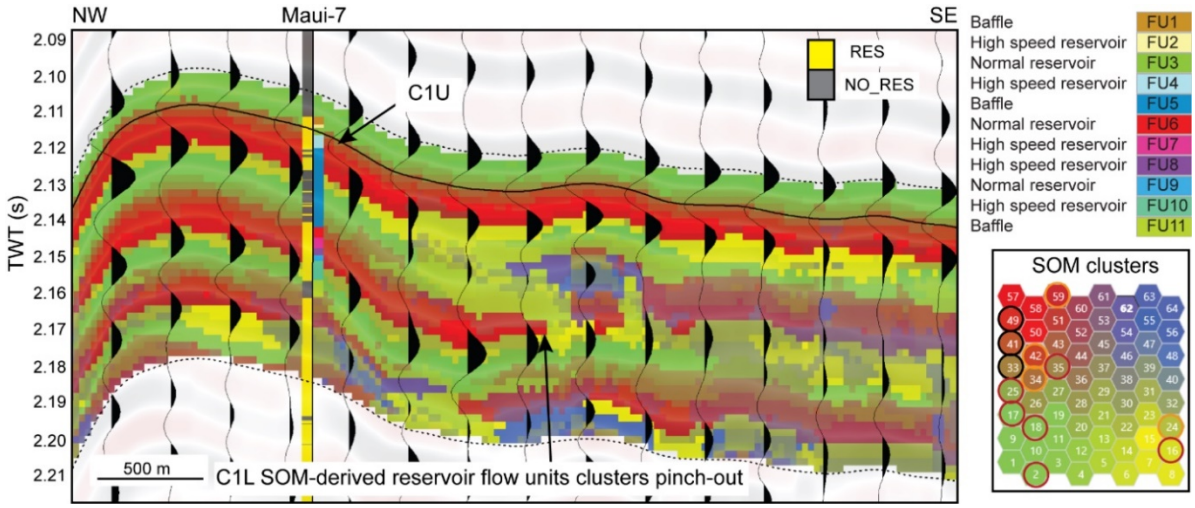

Figure 3. 11. NW-SE vertical SOM sections co-rendered with seismic amplitude (wiggle traces) and crosses Maui-7 well, which display net reservoir and flow units discrete logs. The locations of vertical section is shown in Figure 3.5a. The black and orange circles in the SOM 2D map indicate SOM neurons correlate to high speed and normal reservoir flow units defined in the C1U and C1L whereas black circles indicate baffles defined in the C1M interval. The solid horizon indicates the top of the C1 Sand reservoir and the dotted horizons indicate 10 ms and 70 ms analysis window used in the SOM analysis. FU - flow unit; SOM - self-organizing maps; RES - net reservoir; NO_RES - non-reservoir interval. The location of this section is shown in Figure 3.5a.

A west-east arbitrary line across the northern part of the Maui B region, the Maui-5 well and the southern part of the Maui A region (Figure 3.12) shows that clusters N50 and N51 correlate to high-speed and normal reservoir flow units (FU2 and FU3). The SOM also provides better granularity compared to Gunter et al. (1997) approach, which defines the shaley sand flow unit (FU4) as a baffle. The SOM shows that cluster N51 corresponds to the sandy zone within this C1U baffle and N6 correlates to the shaley zone within this flow unit. Moreover, the SOM results show that four clusters (N22, N30, N5 and N13) subdivide baffles (FU5 and FU7) into four smaller zones in the C1M interval. In the C1L interval, clusters N51, N50 and N57 correlate to high-speed and normal reservoir flow units (FU8, FU9 and FU10). In addition, the SOM clusters in the C1U extends towards Maui A and Maui B regions.

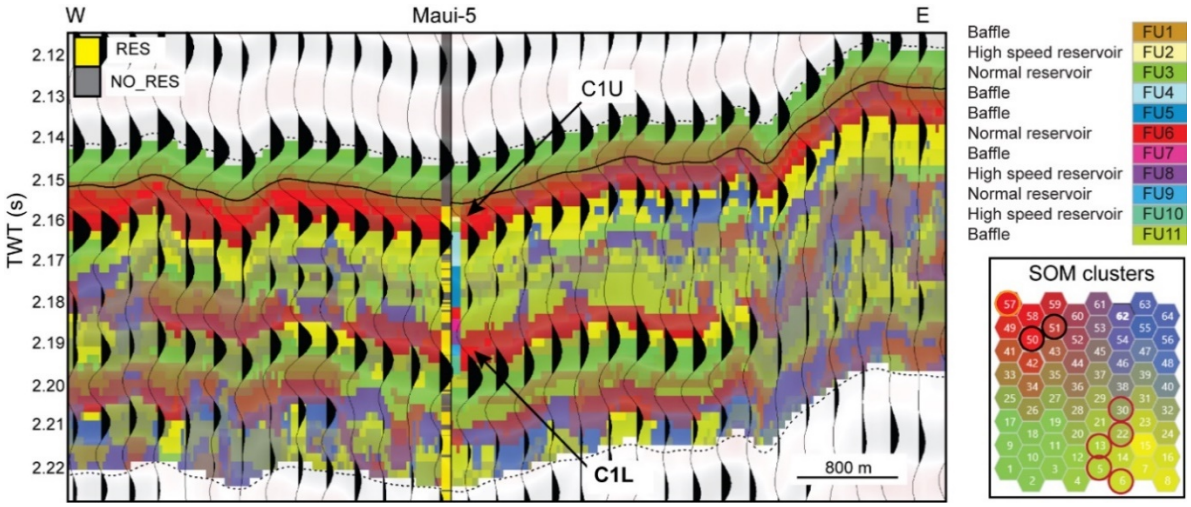

Figure 3. 12. W-E vertical SOM sections co-rendered with seismic amplitude (wiggle traces) and crosses Maui-5 well, which display net reservoir and flow units discrete logs. The locations of vertical section is shown in Figure 3.5a. The black and orange circles in the SOM 2D map indicate SOM neurons correlate to high speed and normal reservoir flow units defined in the C1U and C1L whereas black circles indicate baffles defined in the C1M interval. The solid horizon indicates the top of the C1 Sand reservoir and the dotted horizons indicate 10 ms and 70 ms analysis window used in the SOM analysis. FU - flow unit; SOM - self-organizing maps; RES - net reservoir; NO_RES - non-reservoir interval. The location of this section is shown in Figure 3.5a.

A nearly W-E arbitrary line crosses the northern part of Maui A and the Maui-3 well (Figure 3.13). In the C1U interval, cluster N52 correlates to the high-speed reservoir flow unit (FU2) whereas N26, N35, N59, and N15 correlate to baffles (FU1 and FU3). In the C1M interval, N48 and N11 show correlation to baffle (FU5) and N54, N45, N53, and N23 correlate to normal and high-speed reservoir flow units (FU7 and FU8) in the C1L. This cross-section shows that the high-speed and normal reservoir-derived SOM clusters defined in the C1U and C1L intervals at Maui A, the saddle and Maui B are connected (white arrows) and are affected by the Ihi fault (cyan arrow). The offsets of the reservoir clusters at the fault suggest that the fault is sealing.

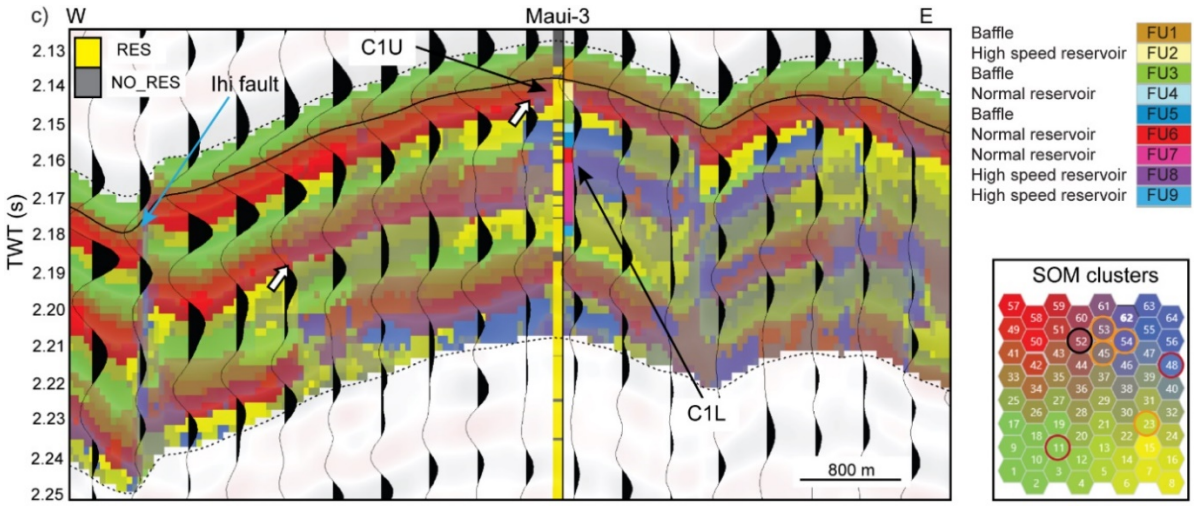

Figure 3. 13. Nearly W-E vertical SOM sections co-rendered with seismic amplitude (wiggle traces) and crosses Maui-3 well, which display net reservoir and flow units discrete logs. The locations of vertical section is shown in Figure 3.5a. The black and orange circles in the SOM 2D map indicate SOM neurons correlate to high speed and normal reservoir flow units defined in the C1U and C1L whereas black circles indicate baffles defined in the C1M interval. The solid horizon indicates the top of the C1 Sand reservoir and the dotted horizons indicate 10 ms and 70 ms analysis window used in the SOM analysis. FU - flow unit; SOM - self-organizing maps; RES - net reservoir; NO_RES - non-reservoir interval. The location of this section is shown in Figure 3.5a.

Based on the rock typing and SOM analyses, the majority of the high-speed and normal reservoir flow units are found in the C1U and C1L intervals whereas most of the baffles are in the C1M interval. I explored the spatial distribution of these SOM-derived flow units using 3D visualization tools. Figures 3.14 to 3.16 show 3D views of the SOM-derived flow units for the C1U interval (Figure 3.14), the C1M interval (Figure 3.15) and the C1L interval (Figure 3.16). Figure 3.14a shows the results with all SOM neurons turned on for the C1U interval. The high-speed and normal reservoir SOM-derived flow units penetrated by the Maui-7 well (Figure 3.14b) show NE-SW trending shoreline sands that seem to be fed by channelized sand features (green arrow). Channelized features were also observed on the northeast side of Maui B and in the Maui A west area (yellow arrows). The high speed and normal reservoir SOM-derived flow units penetrated by the Maui-5 well (Figure 3.14c) show sheet-like sand facies that were deposited across the field, going from the Maui B region to the Maui A region. The high-speed reservoir SOM-derived cluster at Maui-3 (Figure 3.14d) shows sheet-like facies that were deposited in the Maui A region. Based on these analyses, I noted that different SOM clusters indicate different high speed and normal reservoir flow units. This suggests that that the SOM is sensitive to subtle changes in reservoir properties within these sands.

Figure 3.14e shows all of the high speed and normal reservoir SOM-derived flow units identified at the three wells. It shows that reservoir clusters defined in the Maui B region (N50, N51, N49, and N41) extend to the Maui A region (N52). This suggests that the C1U reservoirs in Maui A and Maui B are connected and extremely permeable. This observation agrees with pressure data acquired in Maui-7 and Maui-5 wells that suggest 600-700 kPa pressure depletion in Maui B and the saddle region due to production from the Maui A wells.

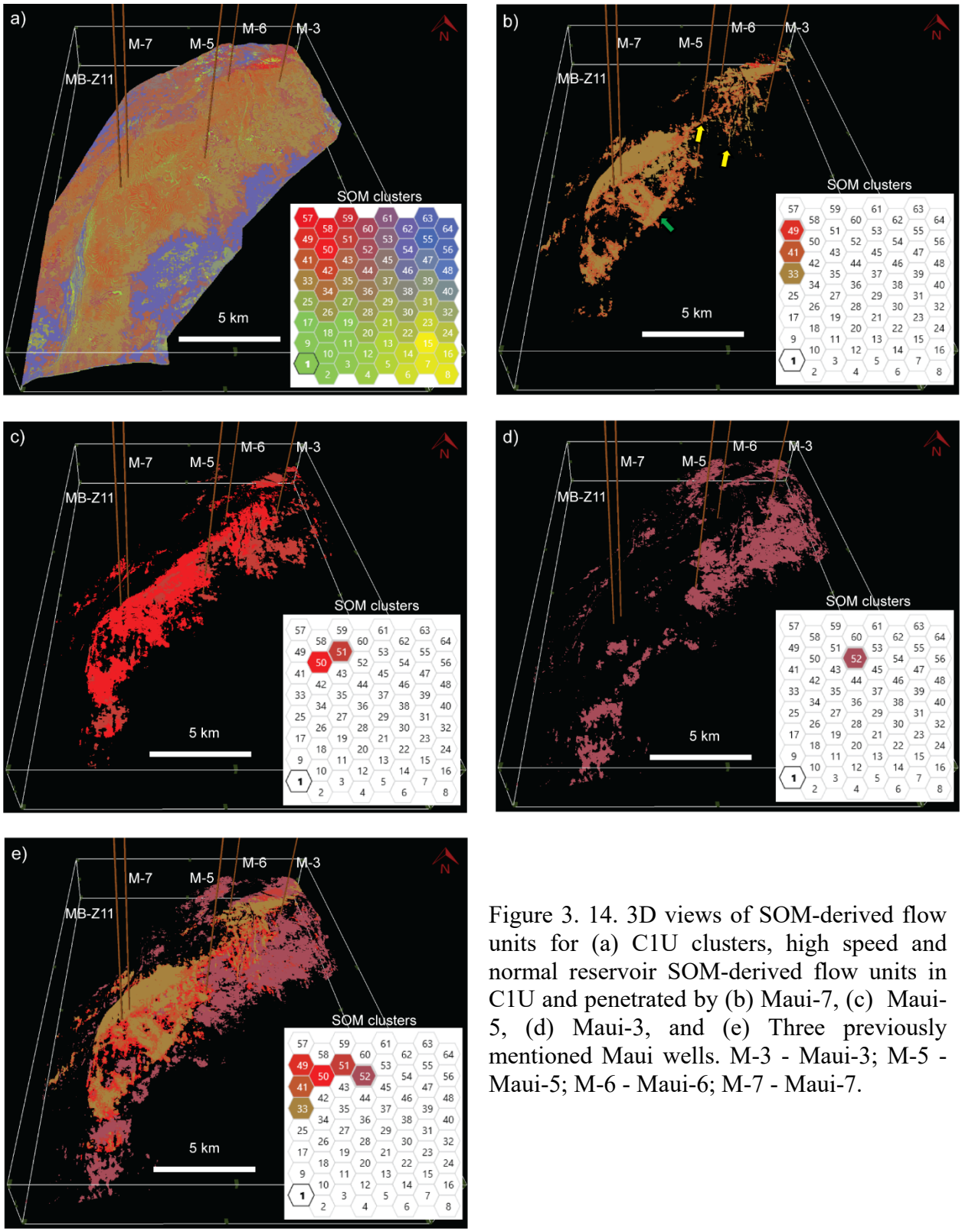

Figure 3. 14. 3D views of SOM-derived flow units for (a) C1U clusters, high speed and normal reservoir SOM-derived flow units in C1U and penetrated by (b) Maui-7, (c) Maui-5, (d) Maui-3, and (e) Three previously mentioned Maui wells. M-3 - Maui-3; M-5 - Maui-5; M-6 - Maui-6; M-7 - Maui-7.

Figure 3.15a shows all of the SOM clusters for the C1M interval. Figures 3.15b to 3.15d show only SOM-derived clusters that correlate to baffles in the Maui-7, Maui-5 and Maui-3 wells. I observed that the SOM clusters identified at Maui-7 well, where the C1M interval is composed mostly of shale, are different from the clusters defined at Maui-5 (a silty shale facies) and at Maui-3 (carbonate cemented sands). All of the SOM-derived clusters that correlate to baffles are shown in Figure 3.15e. These baffle units act as a main barrier between C1U and C1L.

Figure 3.16a shows all of the SOM classification results for the C1L interval. The high-speed and normal reservoir SOM-derived flow units penetrated by the Maui-7 and Maui-5 wells (Figures 3.16b and 3.16c) show NE-SW trending sinuous channel-like (cyan arrows) and sheet-like sand facies. The normal reservoir SOM-derived flow units penetrated by Maui-3 (Figure 3.16d) show sheet-like sand facies that seem to be deposited in the Maui A region and then extend to the eastern and southern parts of Maui B. All the high-speed and normal reservoir SOM-derived flow units identified in the C1L interval are shown in Figure 3.16e, which suggests that the C1L reservoir sands are in a good communication and have high permeability. This observation agrees with the pressure depletion measured at Maui-7 and Maui-5 wells due to Maui A production.

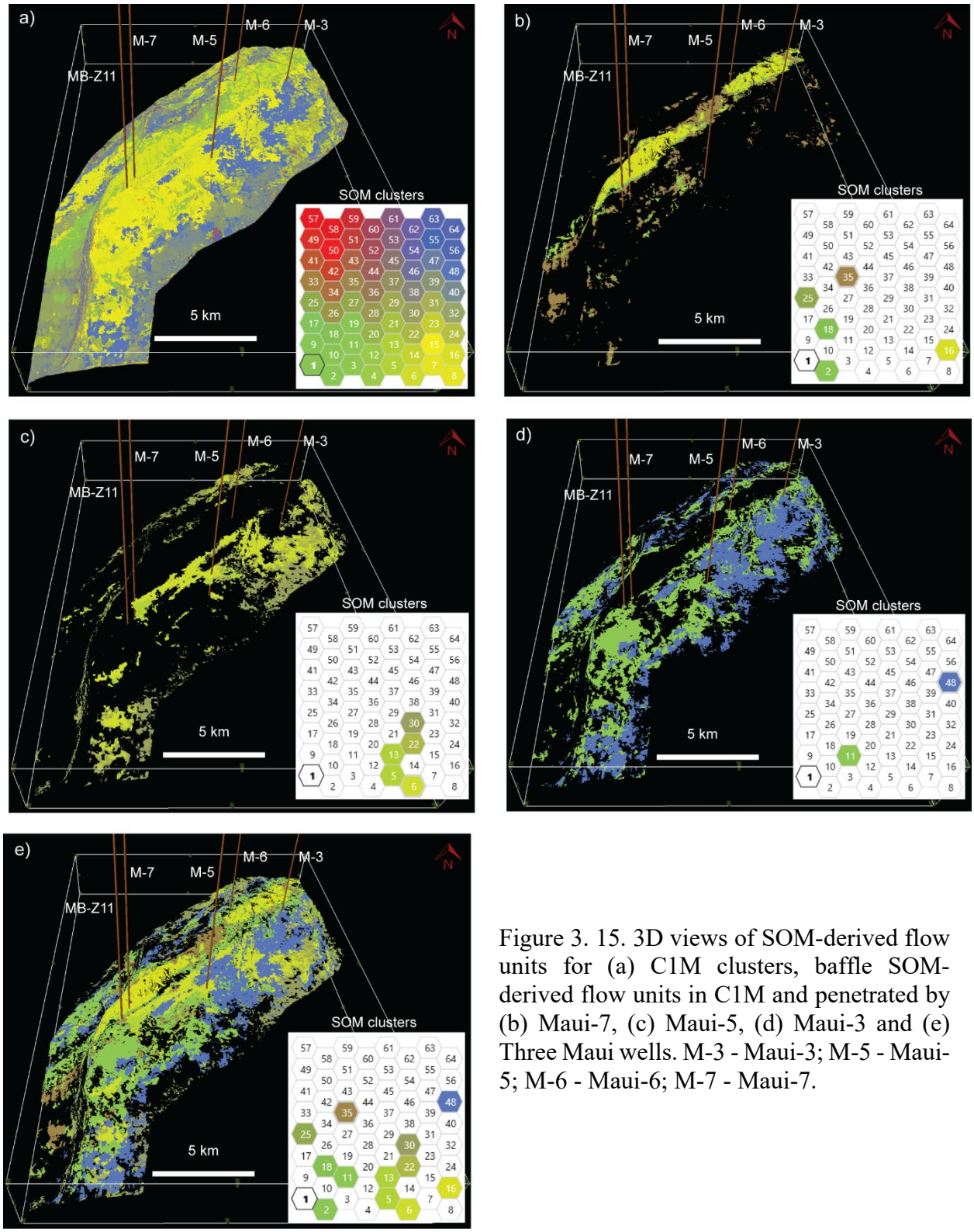

Figure 3. 15. 3D views of SOM-derived flow units for (a) C1M clusters, baffle SOM-derived flow units in C1M and penetrated by (b) Maui-7, (c) Maui-5, (d) Maui-3 and (e) Three Maui wells. M-3 - Maui-3; M-5 - Maui-5; M-6 - Maui-6; M-7 - Maui-7.

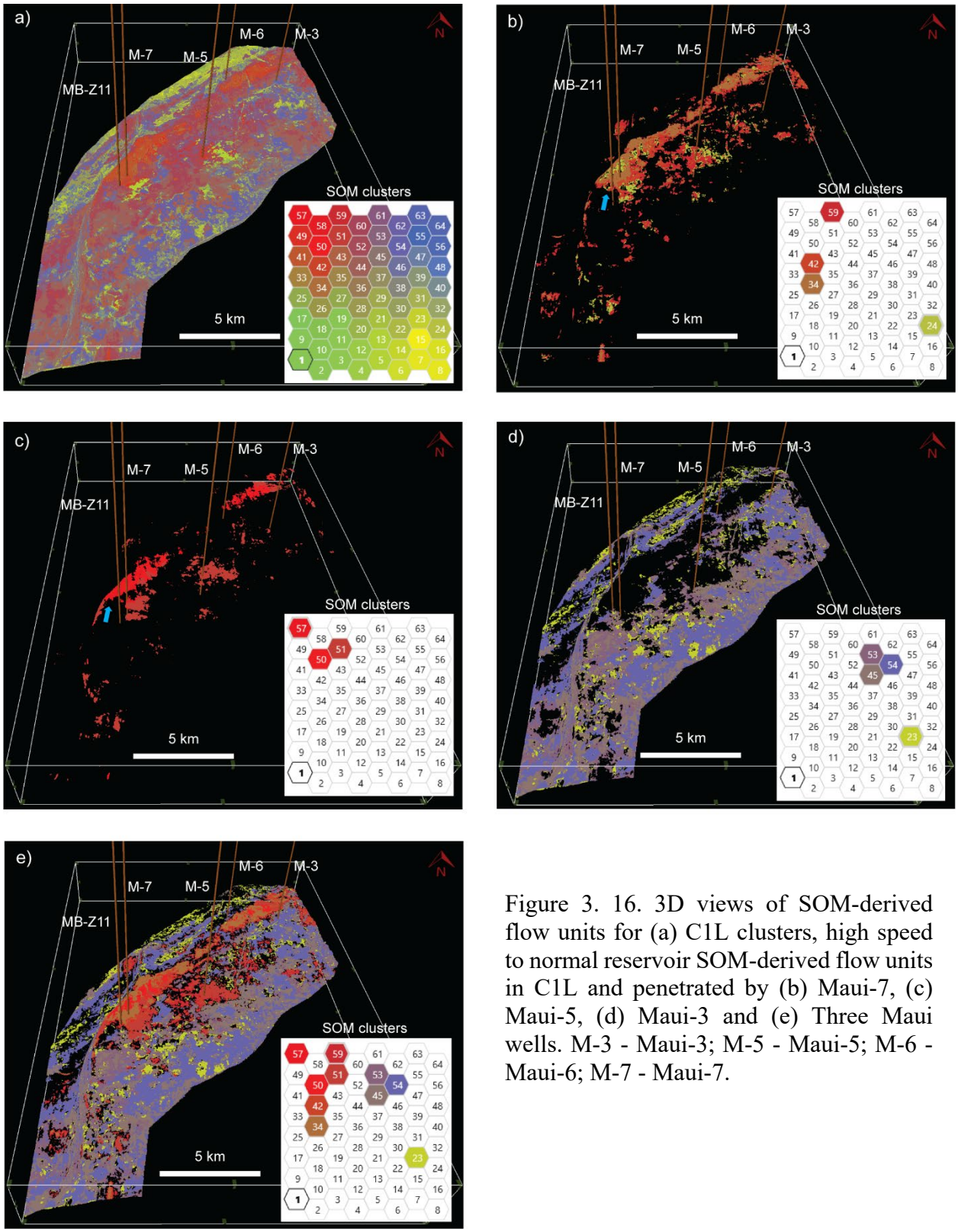

Figure 3. 16. 3D views of SOM-derived flow units for (a) C1L clusters, high speed to normal reservoir SOM-derived flow units in C1L and penetrated by (b) Maui-7, (c) Maui-5, (d) Maui-3 and (e) Three Maui wells. M-3 - Maui-3; M-5 - Maui-5; M-6 - Maui-6; M-7 - Maui-7.

3.12 Discussion

Incorporating well data with SOM cluster analysis is vital to identify net reservoir and delineate reservoir flow units. I found that different SOM cluster patterns along the Maui-7, Maui-5 and Maui-3 well trajectories in the C1U, C1M and C1L intervals suggest that the SOM is sensitive to reservoir properties variations. Those properties change dramatically across the field which suggests the reservoir is very heterogeneous. The three calibration wells are widely separated; Maui-7 is approximately 5.3 km away from Maui-5, which is itself 11 km from Maui-3. As a result, the SOM clusters at Maui-3 are very different from those defined at Maui-7 and Maui-5, which agree with the various log characters and graphical rock typing plots analyzed for these wells. The MB-11 well, which was not used for calibration and is about 1 km from Maui-7, correlates to SOM clusters that are similar to the patterns defined at Maui-7 (Figures 3.14b, 3.16b, and 3.17). This suggests that incorporating closely spaced wells can aid in validating the SOM classification results. Comparing SOM cluster patterns for farther apart wells helps develop a consistent understanding of the reservoir heterogeneity. Thus, SOM cluster analysis aids in filling our understanding of facies and reservoir properties variations where well data are missing.

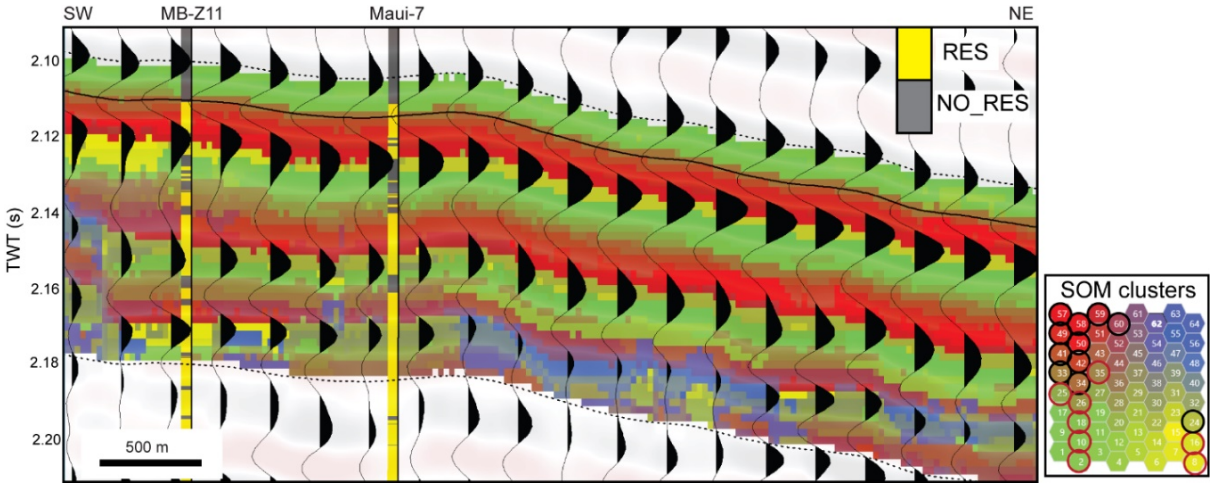

Figure 3. 17. SOM-to-well validation of closely-spaced wells (1 km apart). NE- SW arbitrary vertical section extracted from SOM classification volume co-rendered with seismic amplitude data (wiggle display) and crosses Maui-7 and MB-11 wells penetrated the C1 Sand reservoir at Maui B region. The location of the vertical section is shown in Figure 3.5a). In SOM 2D color map, the neurons in black circles correlate to net reservoir and those circled in red correlate to shale or silty shale intervals. The location of this section is shown in Figure 3.5a.

Unfortunately, missing core measurements in small intervals within C1U and C1L penetrated by Maui-7 well limits a more detailed analysis of those zones. The absence of a vertical well penetrating the central part of the Maui A region and the lack of core data for Maui-3 also limit our understanding of further details of the reservoir quality and heterogeneity within this area. This indicates that although the SOM classification technique identifies natural clusters with similar combinations of seismic attributes, the more wells that are included in the SOM interpretation process, the more detailed the information that can be revealed by the SOM clustered volume.

The SOM classification result appears to be more sensitive to porosity variations compared to facies changes. For instance, cluster N57 is correlated in the Maui 7 well to the upper part of a baffle flow unit (FU5), which is composed of middle shoreface, mouthbar, barrier bar, beach, or foreshore facies in the C1U interval (Figure 3.10a). However, in the Maui-5 well, the same neuron (N57) is correlated to a high-speed flow unit (FU10), which is composed of an estuarine/distributary channel in the C1L interval (Figure 3.10b). The petrophysical and core measurements from these thin zones (about 7 m) indicates that in the C1U of Maui-7 well, cluster N57 correlates to a shaley sand zone within FU5 with an average VSH = 31.7% and a core porosity = 19.4%. In the C1L of Maui-5 well, N57 correlates to a clean sand unit (FU10) with an average VSH = 1.2 % and a core porosity = 20.7 %. Although, the VSH changes significantly here, the core porosity display little changes (only a 1.3 % porosity difference). This highlights the importance of incorporating core data information to the SOM interpretation process.

Many case studies have been published about the application of the Gunter et al., 1997 graphical approach to the rock typing analysis of carbonate reservoirs (Rahimpour-Bonab et al., 2012, 2014; Radiansyah et al., 2014; Riazi, 2018). Few case studies have been presented for clastic reservoirs (Gunter et al., 1997; Mode et al., 2014). I find this graphical approach is useful in upscaling the R35 and RQI/FZI rock types and in identifying flow units in clean sands and slightly shaley sand reservoirs. However, the Gunter et al. (1997) approach does not seem to work well with highly shaley sand or silty shale. For example, the Maui-6 well penetrated the most distal part of the field, encountering the highly shaley sand to silty shale intervals of the C1 Sand reservoir. The SMLP and MLP suggest that the C1 Sand reservoir can be divided into 9 flow units (Figures 3.18a and 3.18b). FU2 is a high-speed flow unit which can be verified

by the SFP (Figure 3.18c). In contrast, the SMLP and MLP suggest that FU7 is a high-speed reservoir and FU8 is a normal reservoir flow units. Validating these flow units by using the SFP and net reservoir log indicate that FU7 and FU8 are correlated to non-reservoir silty shale units.

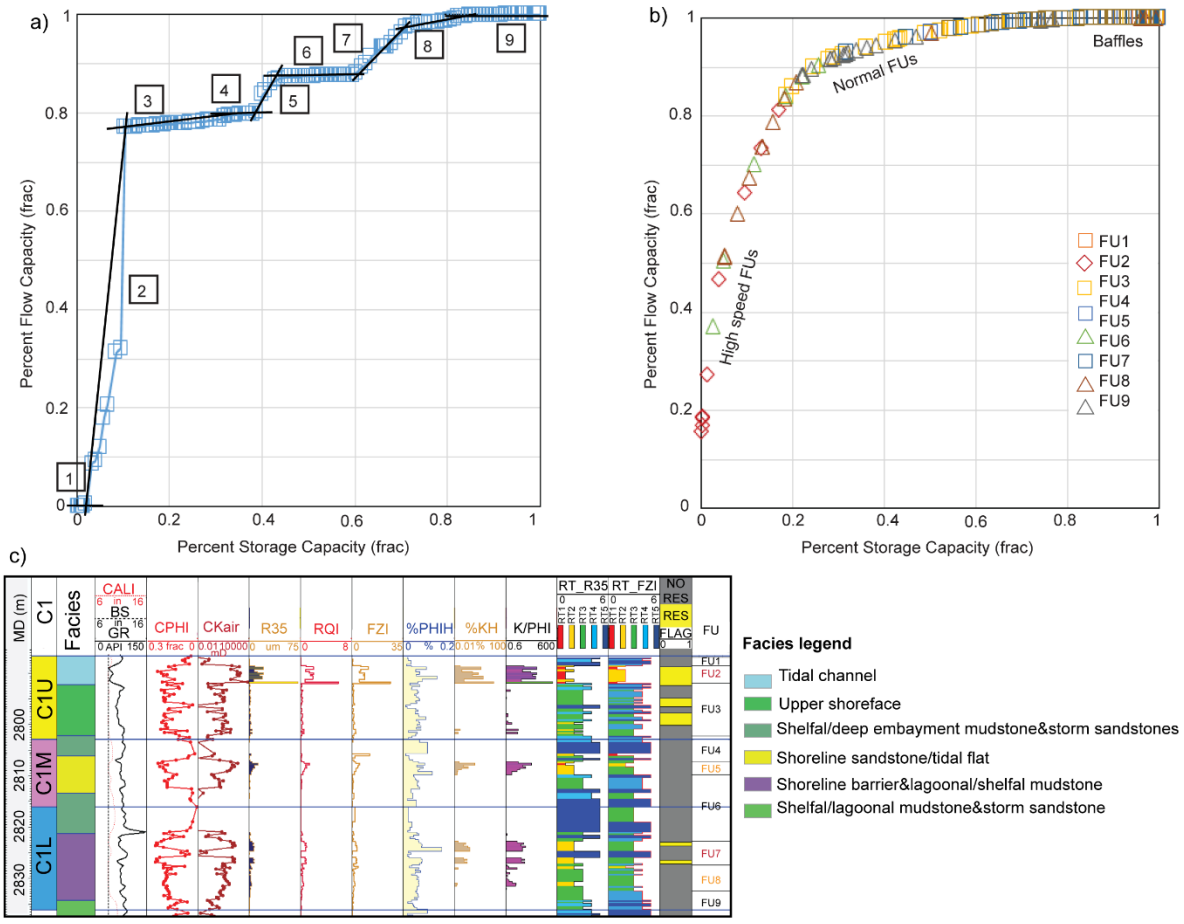

Figure 3. 18. A pitfall in Gunter et al., 1997 rock typing graphical approach for shaley sand reservoir to silty shale intervals. (a) Stratigraphic Modified Lorenz Plot (SMLP), (b) Modified Loren Plot (MLP), (c) Stratigraphic Flow Profile (SFP) of C1 Sand reservoir at Maui-6. Flow units written in red indicate high speed reservoir flow units, the ones written in orange indicate normal reservoir flow units and those written in black indicate baffles. Note that the high speed and normal reservoir flow units are correlated to non-reservoirs so, these flow units cannot be validated by SFP.

3.13 Conclusions

The accurate understanding of reservoir quality and heterogeneity is fundamental to successful reservoir management and oil recovery planning. Imaging subtle stratigraphic baffles, which controls how a petroleum reservoir can be swept, is important. Conventional seismic amplitude data, with its resolution limitations, may be challenged to image these thin reservoirs and stratigraphic barriers. Although seismic attributes can provide improved lateral and vertical resolution compared to amplitude data, the analysis of individual seismic attribute volumes can be a time-consuming process. Even then, any single attribute might not be able to visually illuminate subtle changes in the reservoir properties. Using PCA and SOM techniques, I find for the C1 Sand reservoir of the Maui field that combining the reservoir information content of eight spectral instantaneous attributes into one classification volume aids in understanding the reservoir architecture, quality, and heterogeneity. The SOM classification volume helps to discriminate flow units associated with good quality reservoir from those associated with poor quality reservoir or baffles. The SOM clustered volume seems to be sensitive to petrophysical variations, especially porosity, within the reservoir. Analyzing the 3D SOM-derived flow units enabled us to understand in greater detail than before the reservoir heterogeneity in addition to reservoir connectivity and permeability.

4 Unsupervised machine learning for time-lapse seismic studies and reservoir monitoring

4.1 Summary

Time-lapse (4D) seismic analysis plays a vital role in reservoir management and reservoir simulation model updates. However, 4D seismic data are subject to seismic interference and tuning effects. Being able to resolve and monitor thin reservoirs of different quality can aid in optimizing infill drilling or locating bypassed hydrocarbons. Using the 4D seismic data of Maui field in offshore Taranaki basin, I generated typical seismic attributes that are sensitive to reservoir thickness and rock properties. I found that spectral instantaneous seismic attributes illuminate more detailed reservoir features compared to those same attributes computed on broadband seismic data. I developed an unsupervised machine learning workflow that enables combining eight 4D spectral instantaneous seismic attributes into one merged classification volumes using self-organizing maps (SOM). Those volumes illuminate changes in the cluster patterns obtained for the baseline and monitor volumes. Those changes in the SOM natural clusters suggest production-related changes that are caused primarily by water replacing gas as the reservoir is being swept under a strong water drive. The classification volumes also facilitate monitoring water saturation changes within thin, good and poor quality reservoirs, and illuminates thin baffles. Thus, these SOM classification volumes show internal reservoir heterogeneity that can be incorporated in reservoir simulator models.

Using meaningful SOM clusters, I generated geobodies for the baseline and monitor SOM classifications. The recoverable gas reserves for those geobodies are then computed and compared to production data. I concluded that the SOM classification of the Maui 4D seismic data seems to be sensitive to water saturation change and subtle pressure depletions due to gas production under a strong water drive.

4.2 Introduction

Time-lapse seismic monitoring is an important tool in reservoir management and successful drilling planning (Calvert, 2005; Johnston, 2010). Time-lapse seismic data provides key information that is used to predict dynamic reservoir property changes (i.e., hydrocarbon saturation and/or pressure changes) due to production and to constrain reservoir simulation models through a 4D close-the-loop process (Gouveia et al., 2004; MacBeth et al., 2006; Tian et al., 2014; Nasser et al., 2017). Due to the computation limitations, flow simulation models usually have coarser grid blocks compared to the geological models (Doyen, 2007). Thus, these flow simulation models may not account for detailed reservoir heterogeneities, which can result in mismatches between the modeled seismic response and the actual 4D seismic amplitude (Sengupta et al., 2003; Helgerud et al., 2011).

Similar to 3D seismic, the 4D seismic data are subject to wavelet interference and tuning thickness effects (Johnston, 2013). Moving toward quantitative 4D interpretation and improving the seismic resolution, Bayesian-based probabilistic inversion can be used to quantify reservoir property changes and obtain uncertainty estimates. These inversion processes gradually perturb the reservoir property changes at each trace until a minimum mismatch between the synthetic and actual seismic traces is observed (Buland and El Ouair, 2006;

Kleemeyer et al., 2012; Xue, 2013; Grana and Mukerji, 2015). However, this requires accurate wavelet and rock physics models, which may be challenging to achieve for complex reservoir dynamics (Cao and Roy, 2017). Moreover, Bayesian inversions may not be able to discriminate between shale and thinly bedded sand-shale sequences due to seismic resolution challenges. Although thin sands may not have a significant contribution to the volume of recoverable hydrocarbon, those sands can influence fluid flow. If they are not captured in the geologic and flow simulation models, there can be a mismatch between the model and the 4D seismic data (Nasser et al., 2017).

In order to understand reservoir heterogeneity and to resolve thin reservoirs, spectral decomposition attributes have been applied to various time-lapse projects in different geologic settings (Zhao et al., 2006; Rojas et al., 2009; White et al., 2015). Grochau and Jilinski (2016) tested spectral decomposition analysis on synthetic difference volumes generated for a pre-salt carbonate reservoir. Production facies classifications based on the spectral decomposition difference volumes were derived using probability density functions. They showed that the spectral decomposition difference volumes capture reservoir heterogeneity and that the classification volume illuminated water-saturation-increase facies that can be correlated to known reference water saturation changes. However, the clusters interpreted to be pressure-related showed a poorer correlation to the known pressure changes (Grochau and Jilinski, 2016). Furthermore, Grochau and Jilinski's (2016) approach required time-lapse logging to calibrate the difference spectral decomposition and classification volumes. Unfortunately, time-lapse well data are rarely acquired (Cao and Roy, 2017).

In the absence of the time-lapse logs, an alternative approach is to gather reservoir information from multiple seismic attributes computed on the baseline and monitor volumes using an unsupervised machine learning method, such as self-organizing maps (SOM). An advantage of SOM is its ability to resolve thin beds (Roden et al., 2017). I demonstrated this approach by using 4D seismic data from the Maui field in Offshore Taranaki basin, New Zealand. I first compute typical spectral and instantaneous attributes of the baseline and monitor volumes for the C1 Sand reservoir. I developed a workflow to carefully select a combination of seismic attributes that can be input to the SOM analysis to integrate the preproduction and postproduction reservoir information of the baseline and monitor data into a merged classification volumes. The clustered volumes enable an understanding of the reservoir heterogeneity and illuminate the water saturation changes by calibrating SOM classes to well data, production data and attribute volumes. The SOM classifications also enable monitoring production-related changes within thin reservoirs of very good to good quality sand (high speed and normal reservoir flow units) and poor quality reservoirs, which cannot be monitored on the original 4D amplitude volumes. Geobodies can be extracted from meaningful clusters of the baseline and monitor SOM volumes and then used to calculate recoverable gas of the baseline and monitor. I compared the difference of the estimates to the estimates from the amplitude difference geobodies and to production data. Finally, I discuss the limitations of the workflow and present some ideas on how to deal with those limitations.

4.3 Field history

The Maui field was discovered in 1969 by the Maui-1 well which penetrated the Maui B region and the Maui-2 and Maui-3 wells in the Maui A region. Production commenced in the Maui A region through fourteen wells drilled from a single platform. Three more appraisal wells were drilled and 1600 km of 2D seismic data were acquired in 1986 (Pannett et al., 2004). In 1990, water breakthrough in Maui A wells indicated that the field was producing under a stronger water drive than expected. A full-field 3D seismic survey was acquired in 1991 to assist the development of the Maui B region (Figure 4.1). In 1993, Maui B was put on production through ten development wells drilled from a single platform (Pannett et al., 2004).

Water breakthrough in the MB-09 well in Maui B suggested more severe water overrun than could be explained by the 1995 and 1997 updated reservoir models. In addition, these models could not explain the absence of water in Maui B well MB-12 (Pannett et al., 2004). This indicated that the sweep mechanism in the Maui B region was more complicated than previously thought. Thus, a 4D seismic survey was acquired in 2002 (Figure 4.1) that aided in updating the reservoir model and understanding reservoir performance (Pannett et al., 2004). This was followed by various drilling campaigns in Maui A and Maui B to recover bypassed hydrocarbons (e.g., Telford and Murray, 2008; Murray, 2010; Murray et al., 2010; Thangam, 2013). In 2018, another 4D seismic survey was acquired over the Maui field in order to monitor reservoir production since 2002. According to the latest reserve estimates published by the Ministry of Business and Innovation & Development (MBIE) in 2019, the estimated remaining gas reserves of Maui field are 99 bcf and estimated remaining oil reserves are 4.5 million barrels.

4.4 Dataset

Three 3D seismic surveys have been acquired over the Maui field. The first seismic survey, shot in 1991, serves as the 4D baseline and covers 1000 km^2 (Figure 4.1). It was acquired in a quad-quad configuration – two boats, each with two streamers and two sources. The shot interval was 18.75 m and the receiver group interval was 25 m. For technical and economic reasons, replication of the 1991 survey parameters was not possible. However, a test swath of single-vessel data acquired in 2001 showed a strong 4D signal at the reservoir level (Pannett et al., 2004). The second seismic survey (monitor 1) was shot in 2002. It covers 480 km^2 and was acquired by using two sources and six streamers with 18.75 m and 12.5 m shot and receiver group intervals in 2002 (Van der Veeken, 2016).

During the acquisition of the monitor seismic data, Maui A and Maui B production platforms were in place. To ensure the safety and integrity of the production platforms, a 500 m exclusion zone was enforced around the production facilities that created gaps in the monitor seismic data (Pannett et al., 2004). The third seismic survey (monitor 2) replicated the 2002 seismic program and was acquired in 2018 (McConnell and Pannell, 2018). Only the 1991 3D and 2002 4D seismic data have been released for research purposes by the MBIE, New Zealand.

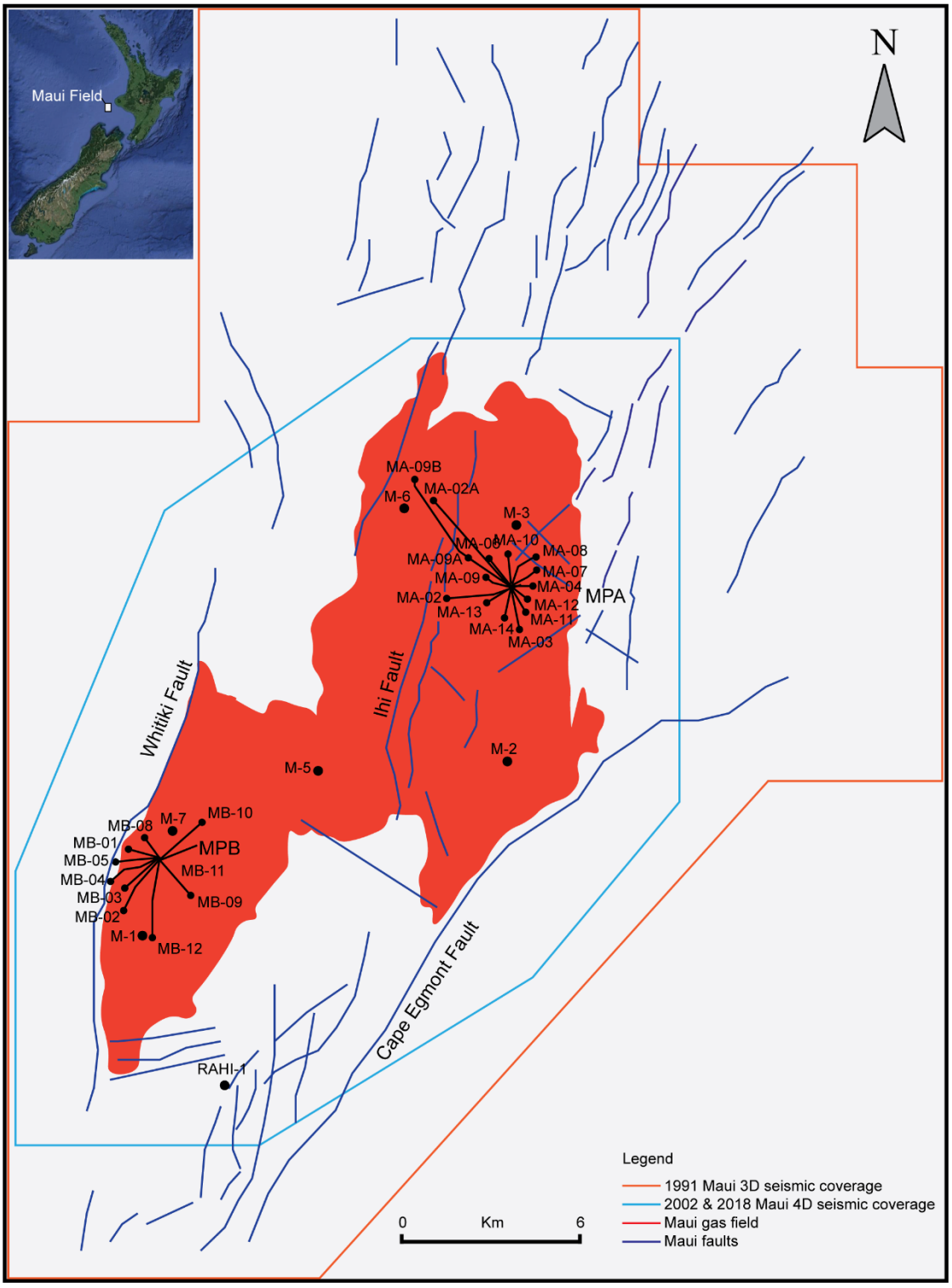

Figure 4. 1. Location map of Maui field in Offshore Taranaki basin, New Zealand (modified from Google Earth, Pannett et al., 2004 and Van der Veeken, 2016). MA - Maui A wells; MB - Maui B wells; MPA & MPB - Maui A & B production platforms. M - Maui vertical wells.

Originally, different seismic processing workflows were applied to the baseline and monitor seismic data. In 2008, the baseline and the first monitor surveys were reprocessed by Shell (personal communication). In this 4D processing workflow, advanced de-multiple and Kirchhoff pre-stack depth migration techniques were applied to the data in order to improve the 4D difference signal and reduce noise. The pre-stack depth migrated volumes were converted to time during the 4D processing (Van der Veeken, 2016). The seismic data used in this thesis include the full-stack baseline, monitor, amplitude difference, and time shift volumes derived from the 2008 reprocessing. No partial stack seismic volumes are available.

Sixty-nine wells have been drilled in the Maui field. Data for most of these wells were released for research purposes. However, only 23 wells have the conventional well logs (bit size, caliber, gamma-ray, density, neutron, resistivity, and sonic logs), well completion reports and deviation surveys. Only the well completion reports and deviation surveys are available for the remainder of the forty-two wells used in this study. Production data of some wells were also released. Not all wells were used in the study. Some wells were drilled long after the monitor survey and others were drilled in the data gaps.

4.5 Methodology

Figure 4.2 shows the methodology used in this study. In this section, I summarize each stage of the workflow. The details for each stage are described in the following sections. In stage 1, I performed rock physics analysis and 4D modeling using well log data to quantify the sensitivity of the seismic response to reservoir thickness and to changes in fluid saturation and pressure. I created zero-offset synthetic models that mimic the reservoir layering in the study

area in order to understand the expected amplitude changes and time shifts that may result from production.

In stage 2, I qualitatively interpreted the 4D data and prepared the data for machine learning analysis (Figure 4.2). Before starting a conventional 4D seismic interpretation, it is critical to check the repeatability of the 4D seismic data. Figure 4.3 shows the calculated normalized root mean square average (NRMS) (Kragh and Christie, 2002) of the 4D amplitude difference, calculated for a 250 ms interval above the C Shale horizon, the main reservoir seal. Repeatability is generally very good (NRMS < 0.2). the figure demonstrate that repeatability at Maui B is better than at Maui A where it there are acquisition artifacts that show up as north-south lineaments. Figure 4.3 also shows poorer repeatability to the east and west of Maui B (white arrows) due to poor seismic imaging caused by the Cape Egmont fault and Whitiki fault, respectively. I performed seismic-to-well ties of the baseline and monitor surveys to identify the main seismic events, which include the C Shale, C1U, and C1L intervals, and to obtain accurate time/depth relationships for machine learning analysis. I used the vertical wells for the seismic tie and map the high-impedance C shale as a peak seismic event (positive reflectivity) and the low-impedance C1U, and C1L sands as trough seismic events (negative reflectivity) on the baseline and monitor seismic volumes. I extracted horizon-based attributes on the baseline, monitor and difference volumes to qualitatively identify the swept areas within the reservoir.

Because of software limitations, I translated the position of the monitor seismic data to the east so that baseline and monitor can be included in a single file. This ensures that the same attribute parameters and SOM model were simultaneously used in the analysis of the baseline and monitor volumes. Well data and horizons were copied and translated to the new monitor seismic location.

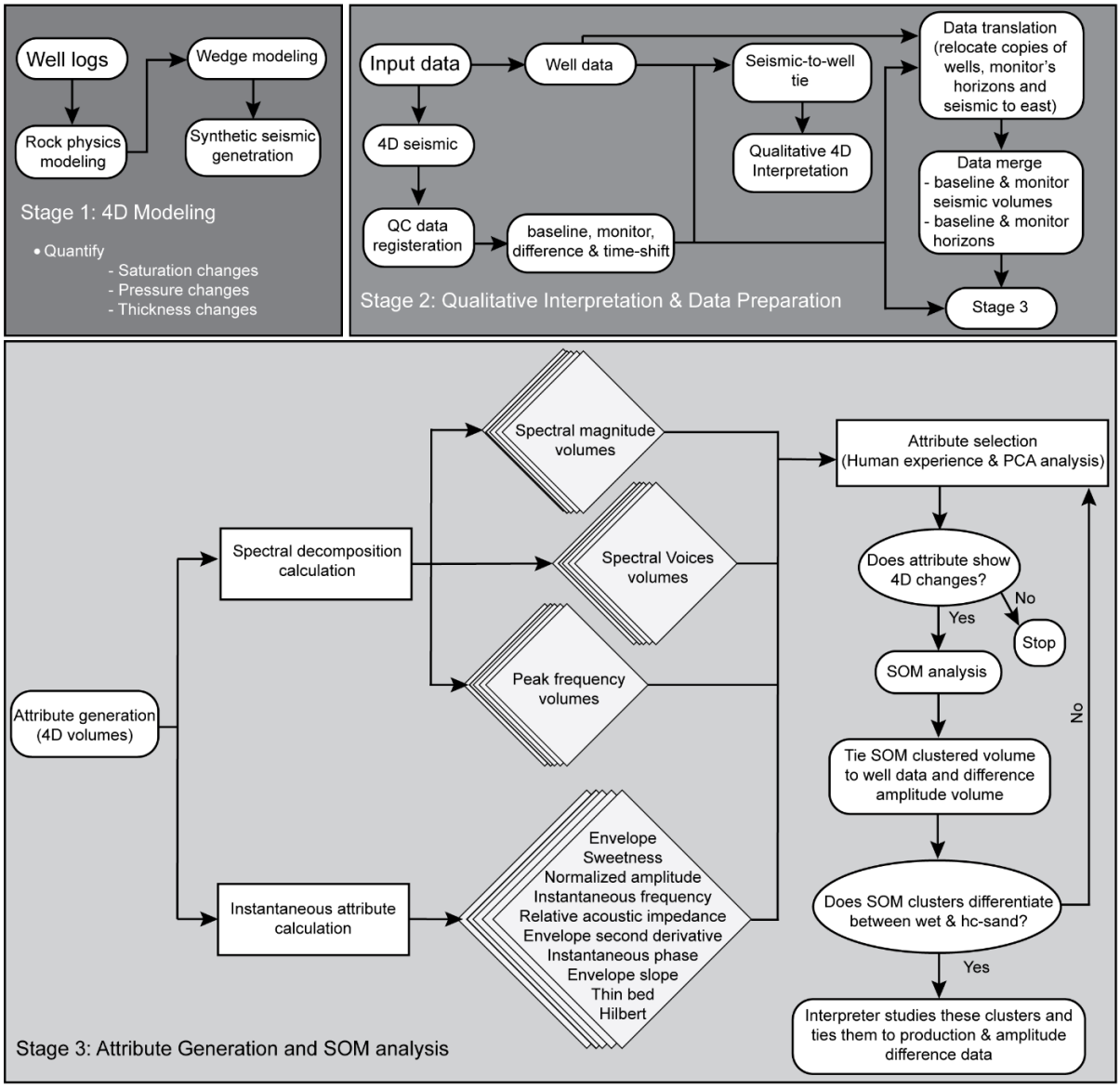

Figure 4. 2. Workflow for 4D modeling, interpretation and, attribute selection for unsupervised machine learning analysis. SOM - self-organizing map; PCA - principal component analysis.

Moving to stage 3, I computed the typical instantaneous and spectral decomposition attributes that are sensitive to reservoir thickness and to changes in reservoir in the C1 Sand reservoir level on the baseline, monitor, and difference volumes (Figure 4.2). I used the visual analysis and principal component analysis (PCA) to select the attributes that best show 4D changes, that are in agreement with the production data and the amplitude difference volumes. These attributes were then used as input to SOM analysis. I correlated the SOM classification volume to the well data in order to determine if the clusters can discriminate wet sand from hydrocarbon-charged sand and shale. If the SOM clustered volume satisfies these conditions, then I study the SOM clusters by using vertical sections and 3D views and calibrated the SOM classifications to amplitude difference and production data to identify swept and unswept areas of the reservoir.

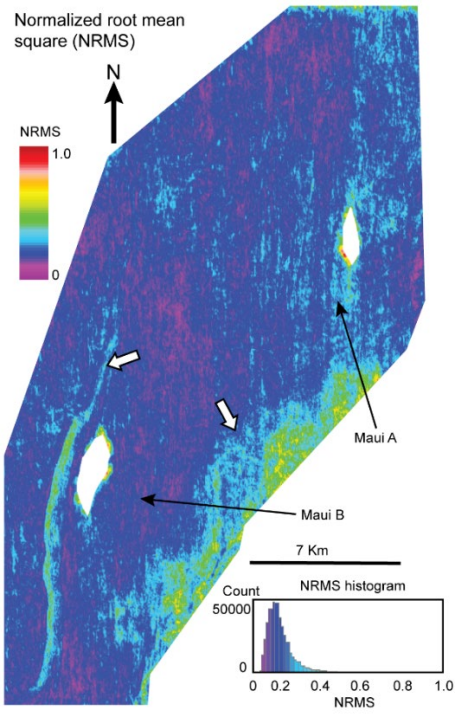

Figure 4. 3. Normalized root mean square slice extracted from 250 ms above the C Shale horizon. In the NRMS color bar, purple, and blue refer to low NRMS whereas red indicates high NRMS values.

4.6 4D Modeling and interpretation

4D modeling and time-lapse feasibility studies are essential tasks before acquiring monitor seismic data and in beginning any interpretation of 4D seismic data to identify the expected magnitude and interpretability of the 4D seismic response (Johnston, 2013). The details of the 4D feasibility studies of Maui field were published by Pannett et al., (2004). Here, I discuss the effect of changing water saturation on the reservoir properties by using Gassmann fluid replacement modeling. The fluid properties were calculated using FLAG software (Table 4.1). The pre-production reservoir properties were calculated as average values of the well logs under virgin conditions. I used Gassmann's (1951) equation to calculate the dry frame rock properties (Table 4.2) and the reservoir properties after production. The acoustic impedance versus water saturation crossplot (Figure 4.4a) shows that the impedance linearly increases as water replaces gas until water saturation reaches a value of about 0.9. Beyond that point, the impedance rapidly increased.

Figure 4.4b shows that if water saturation increases from its irreducible saturation value (Swirr) to its maximum value in swept reservoir (1-Srgw, where Srgw = 0.09) this results in a 4.8 % increase in density and a 0.9 % decrease in velocity. The combined effect of density and velocity change is a 4.1 % increase in acoustic impedance. This demonstrates that density dominates the impedance changes. Because the change in velocity is so small, time shifts for reflections below the reservoir are expected to be very small. The effect of pressure changes on the reservoir rock framework is negligible.

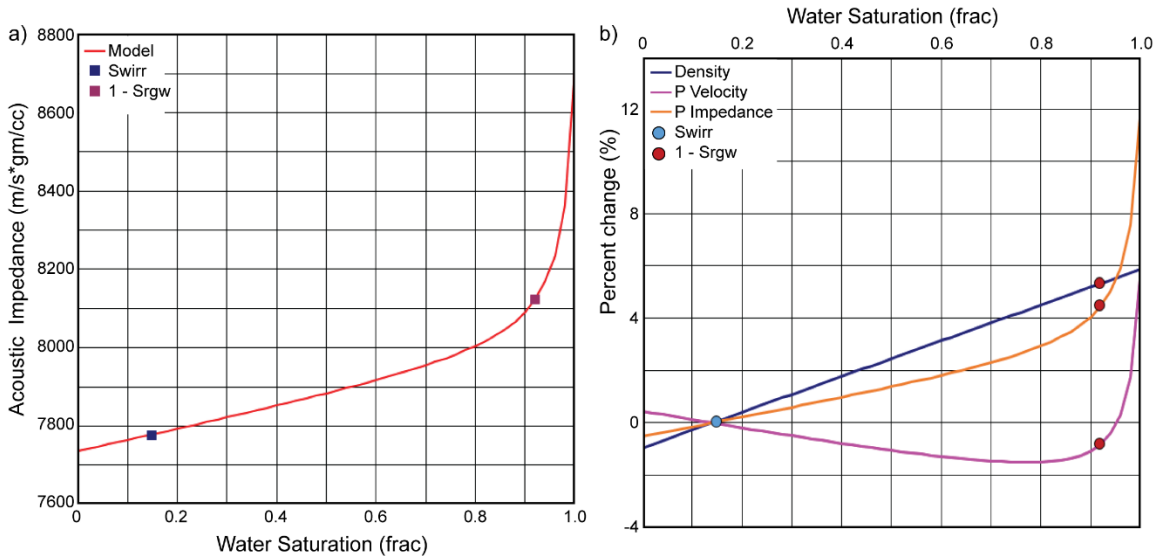

Figure 4. 4. Gassmann crossplots for water replacing gas calculated for the C1 Sand reservoir. (a) Acoustic impedance versus water saturation. (b) Percent change versus water saturation. Swirr - irreducible water saturation; Srgw - residual gas saturation.

Table 4. 1. Fluid properties of C1 Sand reservoir

T (C°)	P (Psi)	GOR (scf/stb)	Gas gravity	Salinity (ppm)	DENSg (gm/cc)	DENSw (gm/cc)	Kg (GPa)	Kw (GPa)
97	3620	20495	0.69	51638	0.16	1	0.049	2.709

Table 4. 2. Dry frame rock properties of C1 Sand reservoir

Kgrain (GPa)	PHI (%)	DENSgrain (g/cc)	Dry Vp/Vs
36	18	2.65	1.6

I used simple wedge modeling to understand 4D resolution and detection limits and to determine expected changes in the time-thickness of the reservoir and amplitude variations as the reservoir is being swept under a water drive mechanism. I create a wedge model mimicking the typical layering observed for the reservoir (Figure 4.5). Reservoir thickness is allowed to change from 0 m to 80 m. Preproduction conditions are a low-impedance gas sand imbedded in high-impedance shale layers of slightly different rock properties (Figure 4.5a). These preproduction reservoir, overburden, and under-burden properties were calculated using average values obtained from the well data. Replacing gas with water (water sweep), which is less compressible than gas and has higher density, resulted in an impedance increase (Figure 4.5b).

The peak frequency of the seismic data was about 38 Hz. Thus, a 38 Hz zero-phase Ricker wavelet is used to generate zero-offset synthetics for the preproduction gas sand reservoir (baseline condition) and water-swept reservoir (monitor). The results show a trough-peak seismic response for the baseline and monitor synthetics (Figures 4.5c and 4.5d). However, the seismic reflection amplitude of the monitor synthetic is smaller than that of the baseline as a result of the impedance increase observed when water replaces gas. The difference of these zero-phase synthetics (monitor-baseline) shows a peak-trough response associated with an impedance increase (Figure 4.5e). Interpretation of 4D data is often facilitated by using quadrature phase data which positions the difference energy in the reservoir interval (Johnston, 2013). Thus, applying -90 phase shift to the zero-offset synthetic yields the quadrature phase result that shows a peak that can be directly interpreted as an impedance increase (Figure 4.5f).

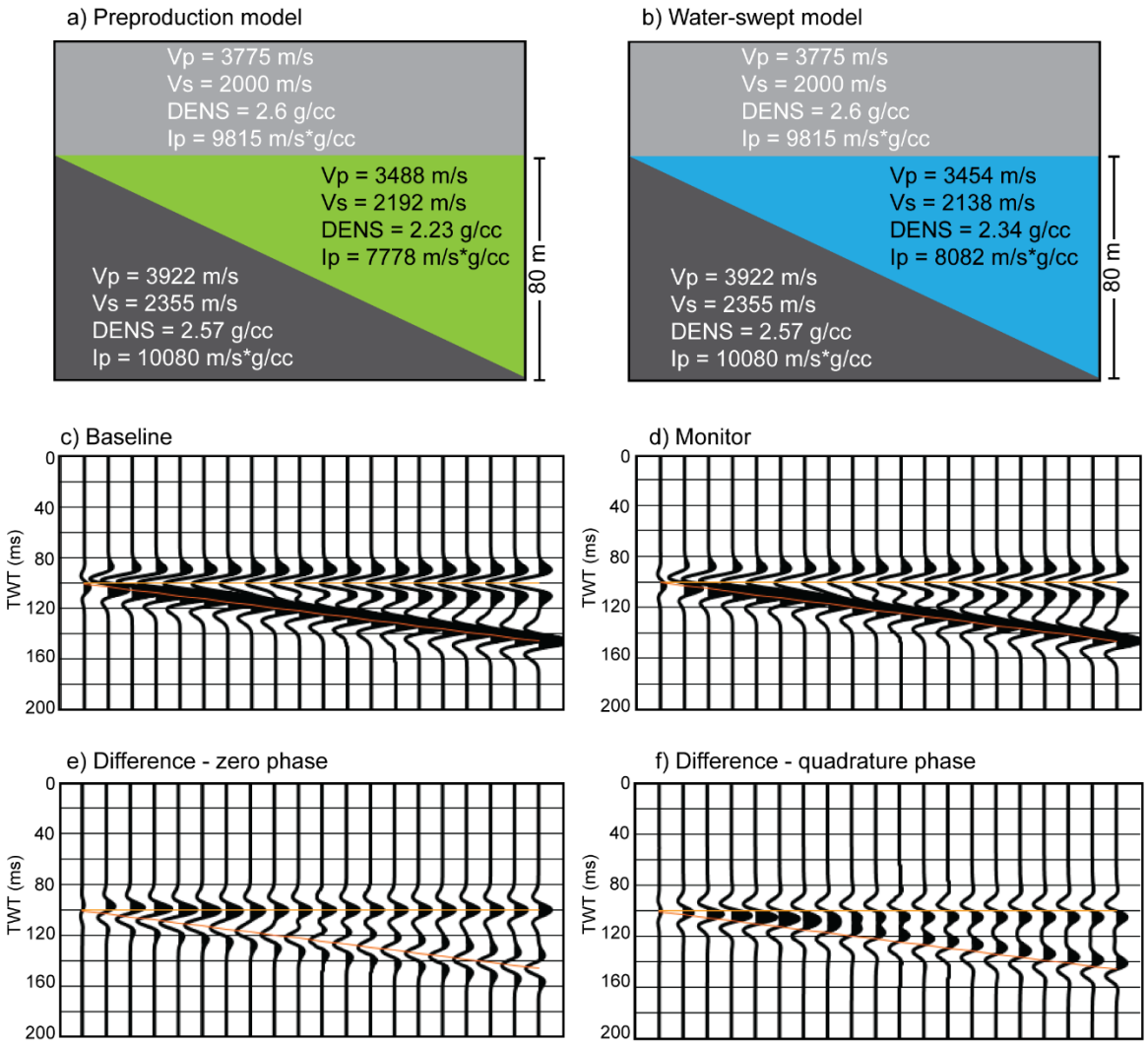

Figure 4. 5. Simple wedge models for C1 Sand reservoir under (a) Preproduction or baseline conditions and (b) Water-swept monitor condition. The reservoir properties for both conditions are written figures a) and b). Green and blue wedges indicate gas-filled and water swept of the C1 Sand reservoir respectively. Zero-offset synthetics using zero-phase 38 Hz Ricker wavelet for baseline (c), monitor (d) and difference (e). Zero-offset quadrature phase difference synthetics (f). The orange lines in the synthetics are the top and base of the wedge model, converted in two-way time. The difference synthetics are magnified by a factor of 3.7.

The modeling shows that time shifts that result from velocity changes in the reservoir are very small, 0.45 ms for 80 m thick reservoir. The synthetics show that the baseline, monitor and differences are subject to tuning but in this the reservoir, the calculating tuning thicknesses of these synthetics were about 19 m. At Maui A, the C1 Sand reservoir is well above the tuning thickness. At Maui B, the C1 Sand was subdivided into C1U and C1L with thicknesses close to tuning.

The 4D interpretation of the baseline, monitor and difference volumes aids to identify fluid saturation changes that occurred between 1991 and 2002 due to production from the C1 Sand reservoir in the Maui field. Figures 4.6a and 4.6b show vertical sections crossing the MB-12 well and extracted from the baseline and monitor seismic volumes. Figure 4.6c displays the quadrature difference (monitor-baseline) after cross-equalization that was done by Shell. The difference section shows two seismic peak events that indicate an increase in impedance over time (hardening). This is caused either by water replacing gas or by pressure depletion in the C1U and C1L reservoir intervals. The C1 Sand produces under a strong water drive from the south-east of the field and water influx across Whitiki fold to Maui B north (personal communication). The rock physics model for the C1 reservoir suggests pressure depletion effects are negligible. The MB-12 well was completed in the C1L and put into production in 1993. Time-lapse logging of MB-12 shows gradual water bottom rise in the high-quality C1L interval (Figure 4.7; Pannett et al., 2004). Impedance hardening is, in fact, observed in the C1L interval on the 4D seismic data, suggesting bottom water rise as water replaces gas due to production from the MB-12 and MB-Z11 wells. Impedance hardening observed in the C1U interval on the seismic data suggests that flank water is overriding the gas due to production

from other wells. This is confirmed by the time-lapse saturation logging acquired in MB-12 in 2003 (Figure 4.7; Pannett et al., 2004).

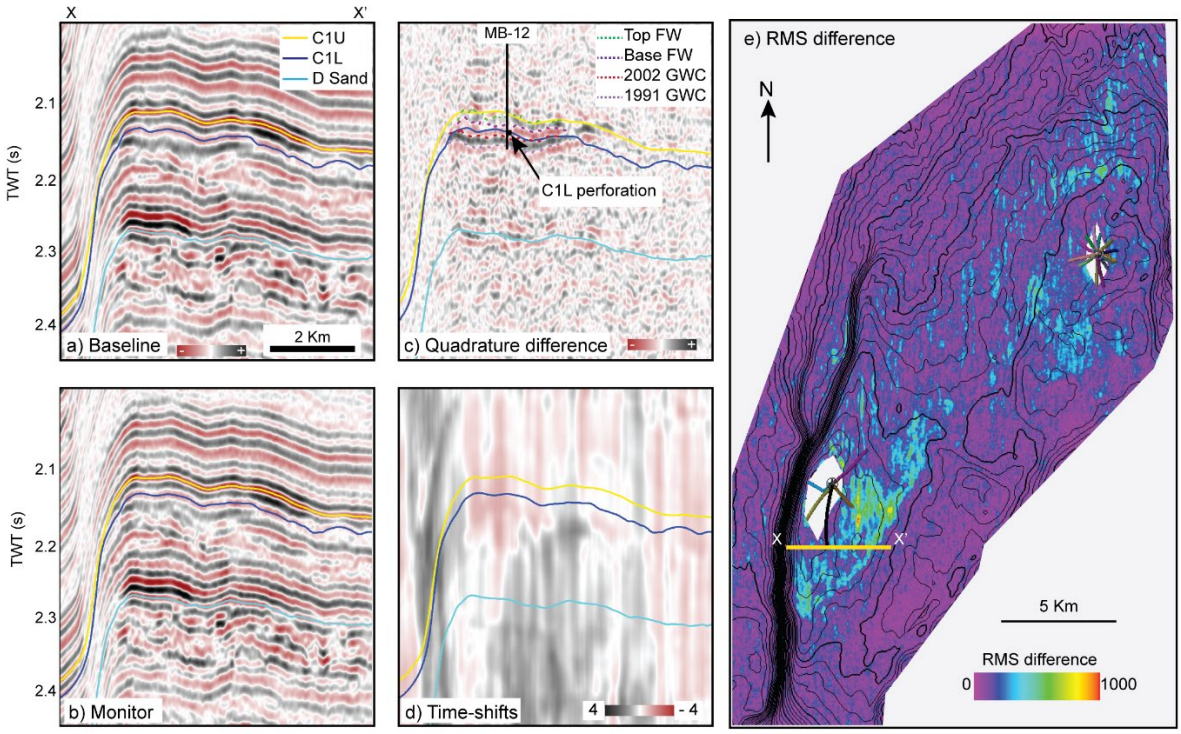

Figure 4. 6. Qualitative Interpretation of 4D Maui data. Vertical sections extracted from (a) zero-phase baseline, (b) zero-phase monitor, (c) quadrature difference, (d) time-shifts volumes. (e) reservoir-interval root mean square (RMS) extracted from amplitude difference volume shows the water sweep (cyan to orange colors) in Maui field. Contour lines indicate time structure map of the top of the C1U Sand reservoir. Yellow line in e) shows the location of the vertical sections (a to d). The black line in c) and the deviated black line in e) represents the location of MB-12 production well penetrated the C1 Sand reservoir. The deviated lines in e) display the production wells that were producing from the C1U between 1991 and 2002. White polygons in Maui A and Maui B regions show the gap zones underneath the production platforms. FW - flank water override; GWC - gas-water contact. The time shifts vary from -1 ms to +1 ms. In the RMS difference color bar, purple refers to low RMS difference values whereas yellow, and orange indicate high RMS difference (i.e., impedance hardening).

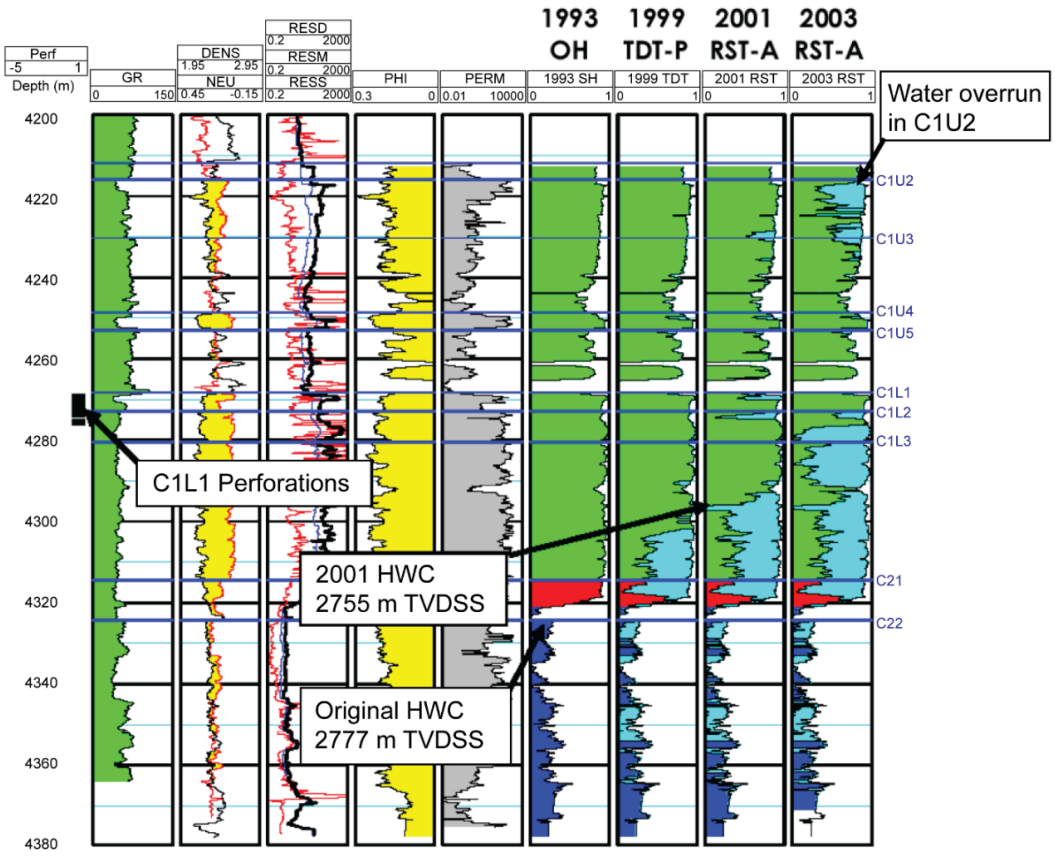

Figure 4. 7. MB-12 C1 Sand reservoir TDT/RST history. Saturation plot colours are: Gas - Green, Oil - Red, Water - Blue. TDT - Thermal decay tool; RST - Reservoir saturation tool. The log tracks from left to right are Gamma-ray (GR), Density (DENS), Neutron (NEU), Resistivity (RESD, RESM, RESS), Porosity (PHI), Permeability (PERM), Hydrocarbon saturation (HC) computed from original 1993 logs, Hydrocarbon saturation calculated from 1999 TDT, 2001 RST and 2003 RST logs (modified from Pannett et al., 2004, used by permission).

Time shifts between baseline and monitor were calculated using a Taylor expansion algorithm (Naeini et al., 2009) with the monitor seismic data as a reference. The vertical section extracted from the time-shift volume (Figure 4.6d) shows very small time-shift values (less than +/- 1 ms) that seem to result from subtle acquisition and processing differences between the baseline and monitor seismic volumes. The figure does not appear to shows production-related time shifts. The time shifts align with the shooting direction and are likely related to differences in acquisition.

The reservoir-interval root-mean square (RMS) amplitude map (Figure 4.6e) extracted from the difference volume for the C1U reservoir shows impedance hardening (cyan to orange colors) in the Maui B and Maui A regions. The 4D changes in Maui B are larger than seen in Maui A. . Production at Maui A began before the acquisition of the baseline survey in 1991. And, as shown in Figure 4.8, production data for two of the Maui B wells (MB-09 and MB-12) and one of the Maui A wells (MA-05) shows that a larger gas volume was withdrawn from Maui B compared to Maui A between 1991 and 2002.

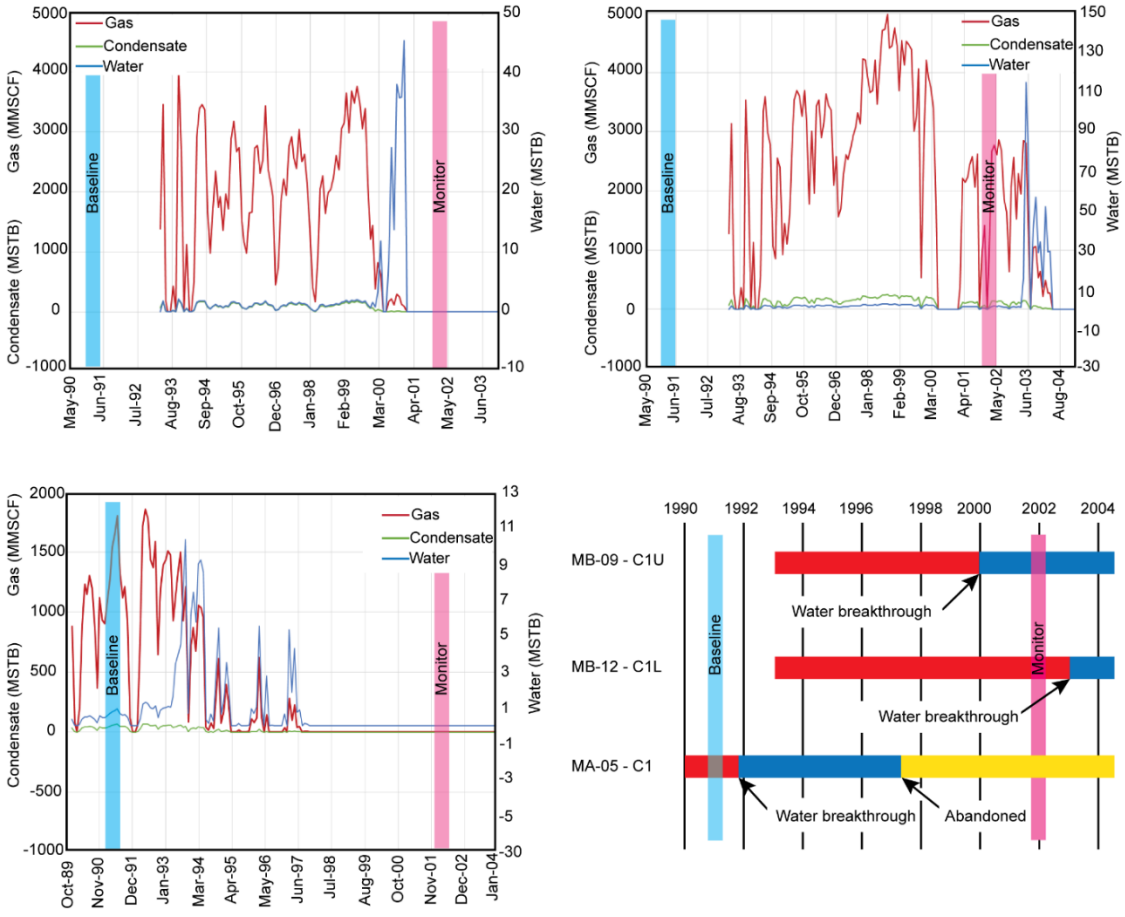

Figure 4. 8. Production history analysis of three of Maui wells. Production profile of (a) C1U Sand reservoir penetrated by MB-09 well at Maui B region, (b) C1L Sand reservoir penetrated by MB-12 at Maui B region and (c) C1 Sand reservoir at MA-05 well at Maui A region. (d) Well time lines of the three wells that summarizes the activities of the wells with respect to the timing of acquiring the baseline and monitor seismic data.

4.7 Seismic attribute selection

In the absence of angle stacks/gathers, I focused on post-stack seismic attributes that are sensitive to reservoir thickness and to lithological and reservoir property change. These include spectral decomposition and instantaneous seismic attributes. Spectral decomposition attributes measure time-varying spectral properties of the seismic data. These properties include spectral magnitude components, spectral voice components, peak frequency, peak magnitude, and spectral bandwidth (Barnes, 2016; Marfurt, 2018b). Instantaneous attributes are defined as time-frequency attributes, which are computed sample by sample on the real and quadrature components of the analytic seismic trace (Taner, 2001; Chopra and Marfurt, 2007).

We usually interpret broadband seismic data. However, broadband data may not the optimal input to seismic attribute analysis because some spectral bands may be contaminated by noise (Li and Lu, 2014). Spectral decomposition analysis maps a 1D signal to a 2D signal of time and frequency, which results in different spectral amplitude and phase components (Partyka et al., 1999; Castagna et al., 2003). Analyzing these various spectral components enables selection of the ones closest to the tuning frequency (tuning frequency = Vint/λ = 3800 / 100 = 38 Hz) of the reservoir and eliminate those bands that are contaminated by noise (White et al., 2015). The spectral decomposition analysis of 4D seismic data can be performed in two different ways; by performing spectral decomposition analysis separately on the baseline and monitor volumes then compute their differences or spectral decomposition were calculated directly on the difference volume (Zhao et al., 2006; Grochau and Jilinski, 2016).

In this study, I tested both approaches and compared the results. Initially, I calculated the spectral decomposition attributes of the baseline and monitor seismic volumes by using the

continuous wavelet transform (CWT). I perform the spectral decomposition analysis at the reservoir interval for a frequency range of 10 to 70 Hz with a 10 Hz frequency interval. I calculated the spectral difference volumes by subtracting the spectral baseline from the spectral monitor data. The objective of this analysis is to select a spectral voice (frequency band) which is close to the tuning frequency of the reservoir. This spectral voice can be used in further attribute generation and machine learning analysis.

Visual analysis of the individual spectral components of the calculated quadrature phase of the spectral difference volumes show that the lower frequency components, such as the 10 Hz spectral voice difference, look noisy and did not contain coherent 4D seismic energy (Figure 4.9b). High-frequency spectral voice differences, like the 60 Hz spectral voice difference displayed in Figure 4.9f, show coherent 4D seismic events similar to those imaged by the 4D broadband difference volume but it is much noisier (Figure 4.9a). I found that the reservoir tuning frequency lies in 30-to-50 Hz range. For example, the 40 Hz spectral voice difference shows 4D seismic events similar to that imaged by the broadband 4D difference volume (compare Figures 4.9a and 4.9e). The 40 Hz spectral voice difference is noisier than the broadband 4D difference and slightly cleaner than the 60 Hz spectral voice difference. I ran the spectral decomposition analysis again for a 30-to-50 Hz range with a 2 Hz interval. Because the frequency interval was less than half that used for the 10, 40, and, 60 Hz spectral voices, the amplitudes are proportionally smaller. However, visually analyzing the resultant spectral components to determine which frequency bands contain the most information about the reservoir is challenging. As a result, I turn to statistical analysis to enable me to select the spectral frequency that best represents the reservoir tuning frequency, which may contain the most information about the reservoir.

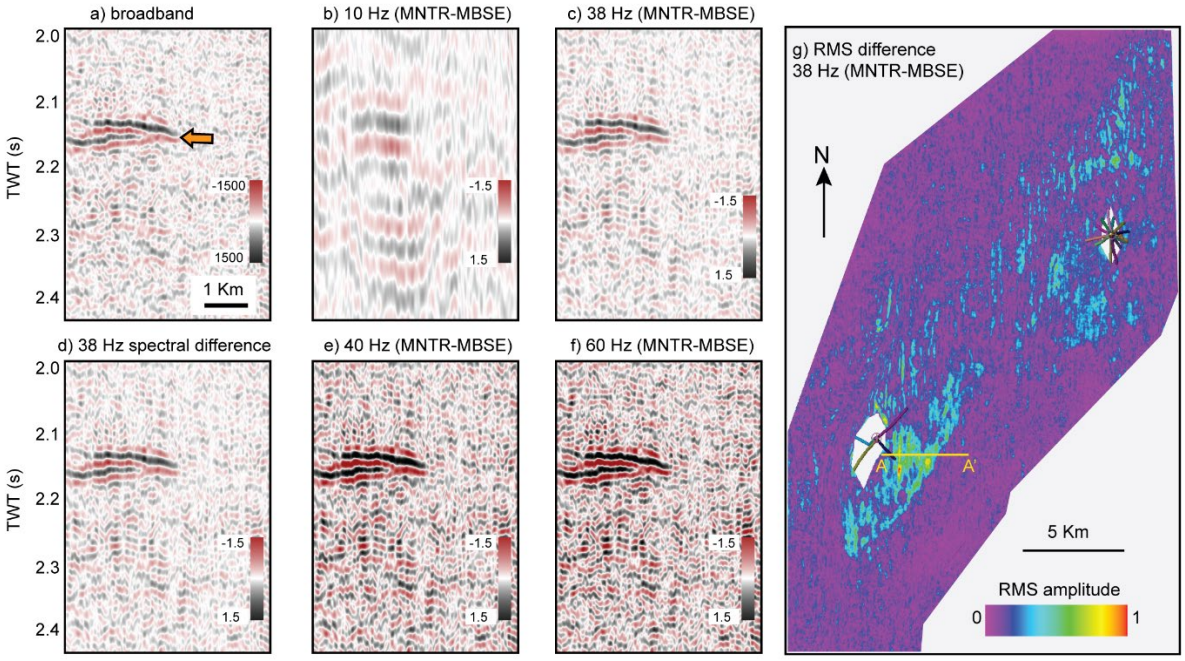

Figure 4. 9. Quadrature phase difference calculated the from broadband 4D difference amplitude (a), the difference calculated from the baseline and monitor spectral voices volumes (b, c, e and f) and 38 Hz quadrature difference (d) calculated from the broadband difference amplitude a). (g) Reservoir-interval RMS amplitude map of the C1U calculated from the 38 Hz spectral voice difference of the monitor and baseline d). Orange arrow shows the 4D changes at the C1 Sand reservoir. The deviated lines show the production wells produced from the C1U sand reservoir between 1991 and 2002. MNTR - monitor; MBSE - baseline. White polygons in Maui A and Maui B regions show the gap zones underneath the production platforms.

Principal component analysis (PCA) is a linear statistical technique that can distill a large library of seismic attributes into a smaller set of seismic attributes based on the relative variance of the attributes within the interval of interest (Roden et al., 2015). I ran the PCA analysis on 11 spectral voices (frequency bands) of the baseline volume, which are generated using spectral decomposition from 30-to-50 Hz in a window 10 ms above to 70 ms below the mapped C1U reservoir horizon. Investigating the PCA results, the 38 Hz spectral voice is listed on top of all the other attributes included in the 1st eigenvector, with a 9.25 % percent contribution to the data variance. This suggests that the 38 Hz spectral voice accounts for most

of the variance within the data and is close to the tuning frequency of the reservoir. This is consistent with the rock physics and synthetic modeling. The 38 Hz spectral voice difference (Figure 4.9c) is similar to that of the broadband amplitude difference (Figure 4.9a). The reservoir-interval RMS amplitude map (Figure 4.7g) calculated from the difference of 38 Hz spectral voices of the baseline and monitor volumes shows 4D changes similar to those illuminated by the broadband difference amplitude volume (Figure 4.6e). However, the RMS difference of the 38 Hz spectral data looks slightly cleaner compared to the broadband RMS difference.

I also performed the same spectral decomposition analysis on the broadband difference amplitude seismic volume. Comparing the 4D seismic events observed in the spectral difference volumes to those shown in the difference of the spectral baseline and monitor volumes, the results from both approaches were very similar. For instance, the 38 Hz spectral difference (Figure 4.9d) appeared to be very similar to the difference of the 38 Hz spectral baseline and monitor seismic volumes (Figure 4.9c).

I computed 15 instantaneous attributes on the baseline and monitor broadband data and on the 38 Hz spectral voices. Figure 4.10 shows a comparison for three of these attributes using average values of reservoir-interval extractions from 5 ms above to 15 ms below the top C1U reservoir. The white polygons indicate the data gaps underneath the Maui A and B platforms. Relative acoustic impedance was calculated using a running sum of the seismic traces followed by the application of a high-pass Butterworth filter. It is considered a modified version of recursive inversion described by (Russell, 1988; Barnes, 2016). This attribute is approximately the band-limited acoustic impedance. It can be related to reservoir properties and is used to define discontinuities. Reservoir-interval extraction from the baseline survey (Figure 4.10a)

shows high amplitude, low impedance events that are likely gas-charged low impedance sands deposited in Maui A and B. The monitor attribute extraction (Figure 4.10b) shows slightly smaller amplitudes of these low-impedance events in the eastern and southern parts of Maui B and the southern side of Maui A (orange arrows). The decrease in amplitude (an increase in impedance) is likely caused by production of the C1U Sand reservoir.

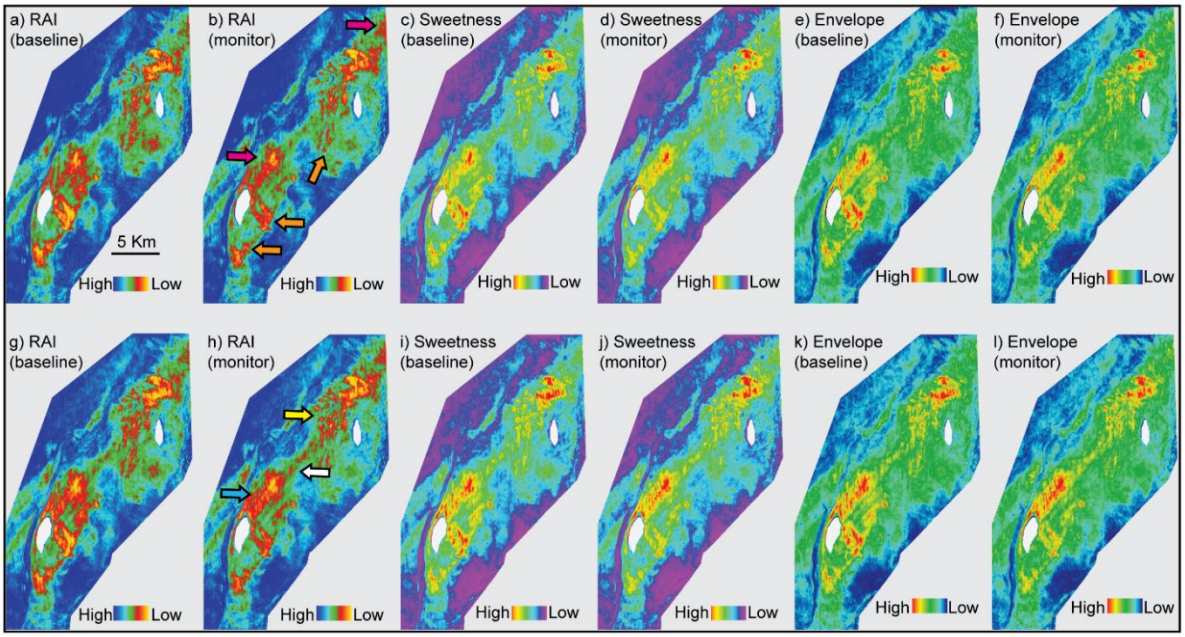

Figure 4. 10. Reservoir-interval slices extracted from broadband instantaneous attributes (a to f) and 38 Hz spectral instantaneous attributes (g to l) for the C1U Sand reservoir. White polygons indicate data gap zones underneath the Maui A and Maui B regions. Orange arrow indicate areas with reduced amplitude observed in the monitor slices that might have been caused by water replaced gas due to production from C1U between 1991 and 2002. Yellow, white and cyan arrows refer to enhancements in illuminating detailed sandy facies in the spectral instantaneous slices com-pared to those attributes calculated on the broadband data. Pink arrows refer to reservoir facies that is better imaged on the monitor data compared to baseline data. RAI - Relative acoustic impedance.

The sweetness attribute is defined as the ratio of the trace envelope to the square root of the instantaneous frequency. It is a useful sand/shale discriminator and helps to highlight sweet spots associated with hydrocarbon-charged reservoirs (Oliveros and Radovich, 1997; Hart, 2008). The sweetness reservoir-interval slices extracted from the baseline and monitor (Figures 4.10c and 4.10d) show high values across the field that indicate the deposition of a sandy facies.

However, the sweetness values in the monitor decrease in Maui B east and south and in Maui A south (Figure 4.10d). Lower sweetness values are observed at the margins of the field and likely indicate shaley lithology.

The envelope attribute describes the vector length of the real and imaginary parts of the seismic trace (Taner, 2001). The reservoir-interval extractions of the envelope for the baseline and monitor volumes (Figures 4.10e and 4.10f) show similar features to those illuminated by the relative acoustic impedance and sweetness attributes. Also, the monitor envelope slice shows decreased amplitude in Maui B east and south and in Maui A south (Figure 4.10f).

I now compare broadband instantaneous reservoir extractions (Figures 4.10a to 4.10f) to those same attribute extractions (Figures 4.10g to 4.10l) calculated from the 38 Hz spectral voice baseline and monitor volumes. The attributes computed from the 38 Hz spectral voice, called spectral instantaneous attributes, show more details than those calculated from the broadband data. Compared to the attributes calculated from the broadband data, the spectral instantaneous attributes better illuminate the sandy facies in Maui A west (yellow arrow) and the channelized sandy-filled features (white arrow) in the saddle between Maui A and B. In addition, the sheet-like sandy facies deposited in Maui B north (cyan arrow) are better illuminated on the spectral instantaneous attributes. However, these sheet-like facies seems to be better imaged in the monitor seismic data compared to the baseline data which suggests the monitor data have slightly better quality compared to the baseline. Similar to the broadband instantaneous attributes, the spectral instantaneous attributes show decreased values to in Maui B south and east and Maui A south that suggest these parts of the reservoir have been water swept. Therefore, the spectral instantaneous attributes can be considered useful candidates for machine learning analysis of 4D seismic data.

4.8 Unsupervised machine learning (SOM) for 4D seismic studies

The self-organizing map (SOM) is an unsupervised machine learning technique that can efficiently extract similar natural clusters within multiple seismic attribute volumes and project those similar patterns into one classification volume (Strecker and Uden, 2002; Roy et al., 2011; Zhao et al., 2016). An SOM uses a non-linear neural network to perform a sample-based investigation of the various input normalized seismic attributes in a multi-dimensional attribute space (Coléou et al., 2003; Roy et al., 2013; Roden et al., 2015). An SOM is sensitive to subtle variations within the input seismic attributes (Roy et al., 2011). Using a 2D topology map, the SOM groups or clusters similar data together into one clustered volume. The SOM clusters are topologically ordered with similar clusters lying beside each other within this 2D map (Roy et al., 2013). The user can control the number of natural clusters based on the predefined number of neurons within the 2D map (Kohonen, 1982; Matos et al., 2006).

My previous discussion focused on the analysis of spectral decomposition and instantaneous attributes, extracted from baseline, monitor and difference seismic volumes, in order to understand their sensitivity to 4D changes. For the SOM analysis, I ensured that the same SOM training model was applied to baseline and monitor. Thus, variations in the SOM clusters' shapes or colors can be tied to production-related changes at the reservoir level. I expect to observe very similar clusters in baseline and monitor data in areas with no production.

The attribute selection and SOM workflow I implemented is shown in Figure 4.11. To select the attributes for SOM analysis, I visually analyze 15 spectral instantaneous attributes, looking for differences between the baseline and monitor volumes. I then applied a PCA analysis at the reservoir level and selected those attributes that are prominent in the first three eigenvectors. Combining the two analyses, I selected the spectral instantaneous frequency, spectral thin bed, spectral quadrature component, spectral relative acoustic impedance, spectral sweetness, spectral envelope, spectral attenuation, and spectral cosine of instantaneous phase attributes as input for unsupervised machine learning (Figure 4.11). All input attributes are normalized so that no one attribute has more weight than another.

In the first step of machine learning, the SOM neurons (called prototype vectors in some publications) are trained using the eight spectral instantaneous attributes extracted from the baseline volume within the interval -10 ms above and 70 ms below the top of the C1 sand reservoir. The training is done at the seismic sample scale to gather similar data within the eight-dimensional attribute space into distinct natural clusters. Then, the trained winning neurons are used to classify all of the multi-attribute seismic samples in the baseline and monitor volumes. The natural SOM clusters were projected using an 8x8 topology map. I used Petrel software to calibrate the baseline and monitor SOM volumes to well data. The monitor SOM classifications are translated back to their original position prior to Petrel data loading. I performed 3D volumetric interpretation on the merged baseline and monitor SOM volumes using Paradise software to visualize swept versus undrained areas.

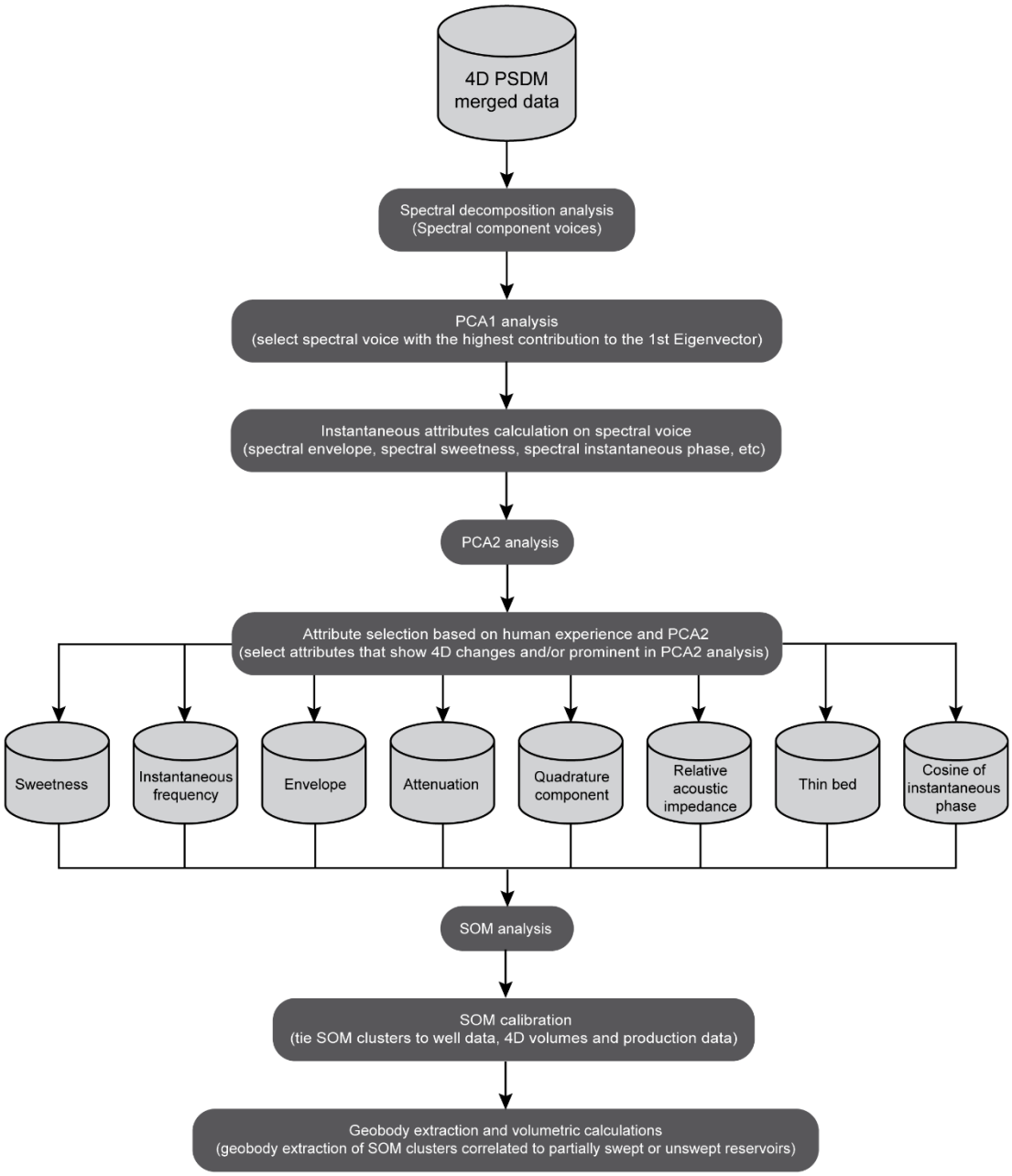

Figure 4. 11. Attribute selection and SOM cluster analysis workflow implemented to integrate data from eight 4D spectral instantaneous attributes for reservoir monitoring studies. PSDM – pre-stack depth migrated seismic; PCA - principal component analysis; SOM - self-organizing map.

4.9 SOM for reservoir monitoring

Similar to the wiggle trace display of a 4D seismic amplitude volume, SOM natural clusters of 4D seismic attributes do not have explicit geological or production meaning on their own. They are simply patterns within the input seismic volumes that must be correlated to geology and reservoir properties. Therefore, I calibrated the SOM classification by correlating SOM clusters to well data, production information and 4D seismic attributes using vertical and 3D displays. The first step was to correlate the SOM clusters of the baseline and monitor surveys to exploration and appraisal wells to validate that the SOM clusters are nearly the same where no production has occurred. Figure 4.12 shows a well display for three exploration and appraisal wells that penetrated the C1 Sand reservoir. The display shows the original wireline logs, petrophysical logs, flow units (see Chapter 3), and SOM classifications extracted from the baseline and monitor volumes. Maui-7 penetrated the Maui-B region. Maui-5 penetrated the saddle between A and B and Maui-6 penetrated the more distal part of the field to the west of the Maui-A region. Maui-7 is close to the production wells in an area likely affected by production. The other two wells are far away from Maui A and B production wells in areas unlikely to be affected by production. Thus, the SOM clusters extracted along Maui-5 and Maui-6 from the baseline and monitor classification volumes look very similar (Figure 4.12). For instance, at Maui-6, almost the same SOM clusters/neurons (N45, N54 and N53) were observed at C1U in the baseline and monitor SOM volumes. This helps validate the baseline and monitor SOM classifications and suggests that any variations in the SOM clusters close to or at producing wells could be related to production-related changes (i.e., water saturation changes).

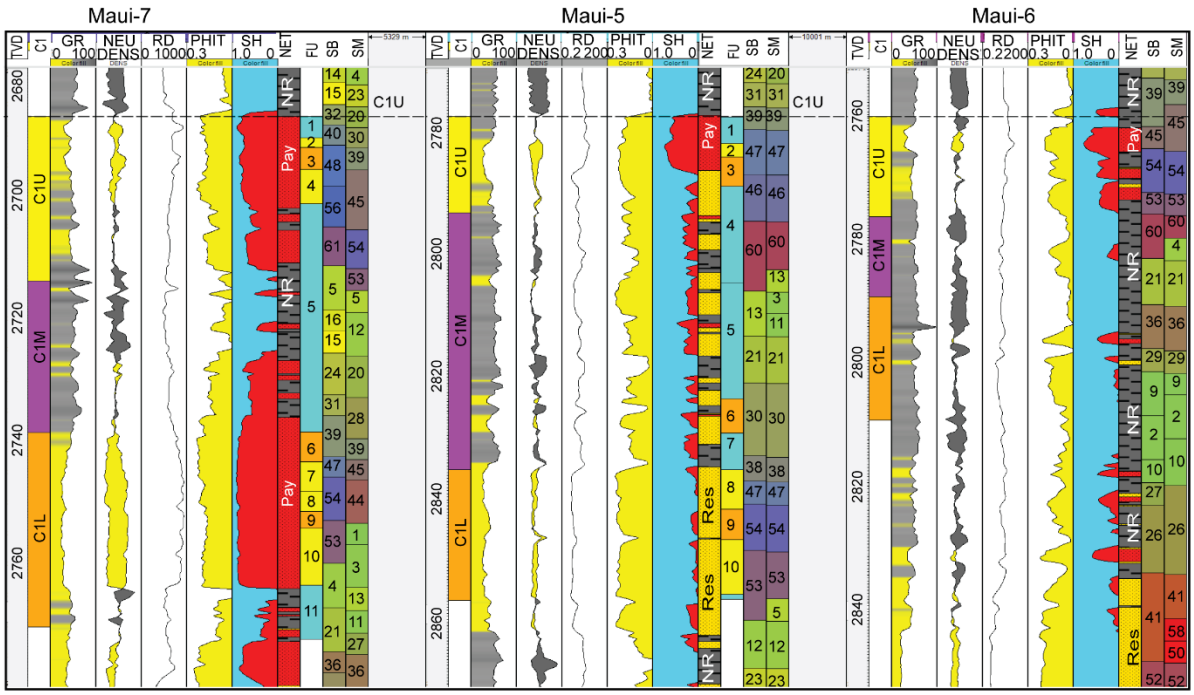

Figure 4. 12. Well section display of three vertical Maui wells show wireline logs, petrophysical logs, flow units and SOM classifications extracted from the baseline and monitor SOM classification volumes at the well locations. TVD – True vertical depth; GR - Gamma-ray; NEU - Neutron; RD - Deep resistivity; PHIT - Total porosity; SH - Hydrocarbon saturation; Pay - Net pay; Res - Net reservoir; NR - Non-reservoir; FU - flow units; SOM - self-organizing map; SB - SOM baseline; SM - SOM monitor. The numbers in FU track shows the flow unit numbers defined in Chapter 3 whereas the numbers in SB and SM tracks indicate the neurons numbers of the SOM classification volume. The flow units colored in yellow and orange indicate high speed and normal reservoir flow units whereas the ones colored in cyan indicate baffles.

Maui-7 is an appraisal well located on the northern edge of the data gap associated with the production platform at Maui B. Unfortunately, no data from vertical production wells away from the gap zone are available. However, because of its proximity to production wells, I expect some production-related changes to be observed at or close to Maui-7. Using the Maui-7 well to analyze the baseline SOM classification volumes, I observed that the gas-charged sand of the C1U interval shows distinct baseline SOM clusters (N32, N40, N48, N58, and N61) that are different from those observed in the gas-charged sand of the C1L (N39, N47, N54, and N53). Those gas-charged sand baseline SOM clusters are also different from the C1M clusters (N5, N16, N15, N24, and N31). This suggests that the SOM is sensitive to subtle rock property changes within the reservoir.

In the C1U and C1L, unlike in Maui-5 and Maui-6, the baseline and monitor clusters are different. This is to be expected due to production from wells close to Maui-7. I will discuss this in detail in the next paragraph. However, in the C1M interval, composed of shale and silty shale, there also slightly different baseline and monitor SOM clusters (Figure 4.12). These thin intra-reservoir shale units seem to be hydrocarbon-charged. The changes in the cluster patterns could be caused by water replacing gas even though the shales have relatively low permeability. Also, these shales respond to pressure changes within the surrounding sands (about a 15% decline compared to the initial reservoir pressure; Pannett et al., 2004). This can result in subtle time shifts (MacBeth et al., 2011; Johnston, 2013; Rangel et al., 2016) that are possibly detected by the SOM classification.

Based on the rock quality analysis of the C1 Sand reservoir (see Chapter 3), the C1 Sand reservoir can be divided in to different flow units (Figure 4.12). At the Maui-7 well, eleven flow units were identified. Flow units 2, 4, 7, 8, and 10 are high speed reservoir flow units with very good reservoir quality. Flow units 3, 6, and 9 are normal reservoir flow units with moderate to good reservoir quality. Flow units 1, 5 and, 11 are baffles with poor reservoir quality to non-reservoir facies (Figure 4.12). Baffles are defined as zones that throttle fluid movements. The SOM classifications correlate well to flow units. For instance, the baseline SOM clusters N32, N61, N5, N16, N15, N24, and N31 are correlated to baffles. The N40, N48, N47, N54, N53, and N4 clusters are correlated to high speed and normal reservoir flow units. I find that the SOM is useful in monitoring water saturation changes in the good reservoir units. SOM can also help monitor poor quality reservoirs, which cannot be observed in the 4D amplitude volumes. The monitor SOM classification shows slightly different clusters compared to those observed in the baseline SOM. For example, in the Maui-7 well, the monitor SOM shows that clusters N30 correlates to gas-charged reservoirs with flow units FU1 and FU2, whereas the baseline SOM shows that cluster N40 correlates to the same units (Figure 4.12). I interpret this result that the C1U sand reservoir flow units have been water-swept and the different monitor SOM clusters are reflective of the change in seismic response produced by water replacing gas.

Investigating the SOM classification of the baseline and monitor volumes using vertical and 3D views enables identifying swept areas of the reservoir and identify the undrained parts. Figure 4.13a shows a vertical section extracted from the baseline SOM classification volume co-rendered with the quadrature component of the baseline seismic data. The section crosses the Maui-7 well, on which the net pay discrete log is displayed. The SOM classification volume shows more details in the seismic facies compared to the quadrature component data.

At the well location, the baseline SOM clusters N32, N40, N48, N56, and N61 (denoted by red circles in the SOM topology map of Figure 4.13a) are correlated to gas-charged sand in the C1U reservoir. These clusters pinch-out updip and extend to touch other blue clusters to east side of the well (N62, N63, and N64; denoted by the orange circles in the SOM legend of Figure 4.13a). These blues clusters lie beside the gas-charged clusters in the SOM topology map, suggesting similar reservoir properties. Also, the quadrature component response of these clusters shows a strong negative amplitude, also indicating gas-charged sand.

The same vertical section extracted from the monitor SOM volume and co-rendered with quadrature component of the monitor seismic data is shown in Figure 4.13b. Clusters N20, N30, N39, N45, and N54 (denoted by the red circles in SOM cluster legend of Figure 4.13b) are correlated to the C1U sand at Maui-7 but are different than the clusters observed in the baseline survey. This suggests that the reservoir has been swept at the Maui-7 location due to production from nearby wells located at the crest of Maui B structure. However, I do not know whether the reservoir is fully or partially swept. The only way to find out would be to drill a new well that penetrates these clusters, to acquire a repeat saturation log at the Maui-7 well or 4D elastic inversion to get density change, if angle stack data become available. I observed that clusters N62, N63, and N64 are also visible in the monitor SOM volume which may suggest unswept areas of the C1U reservoir.

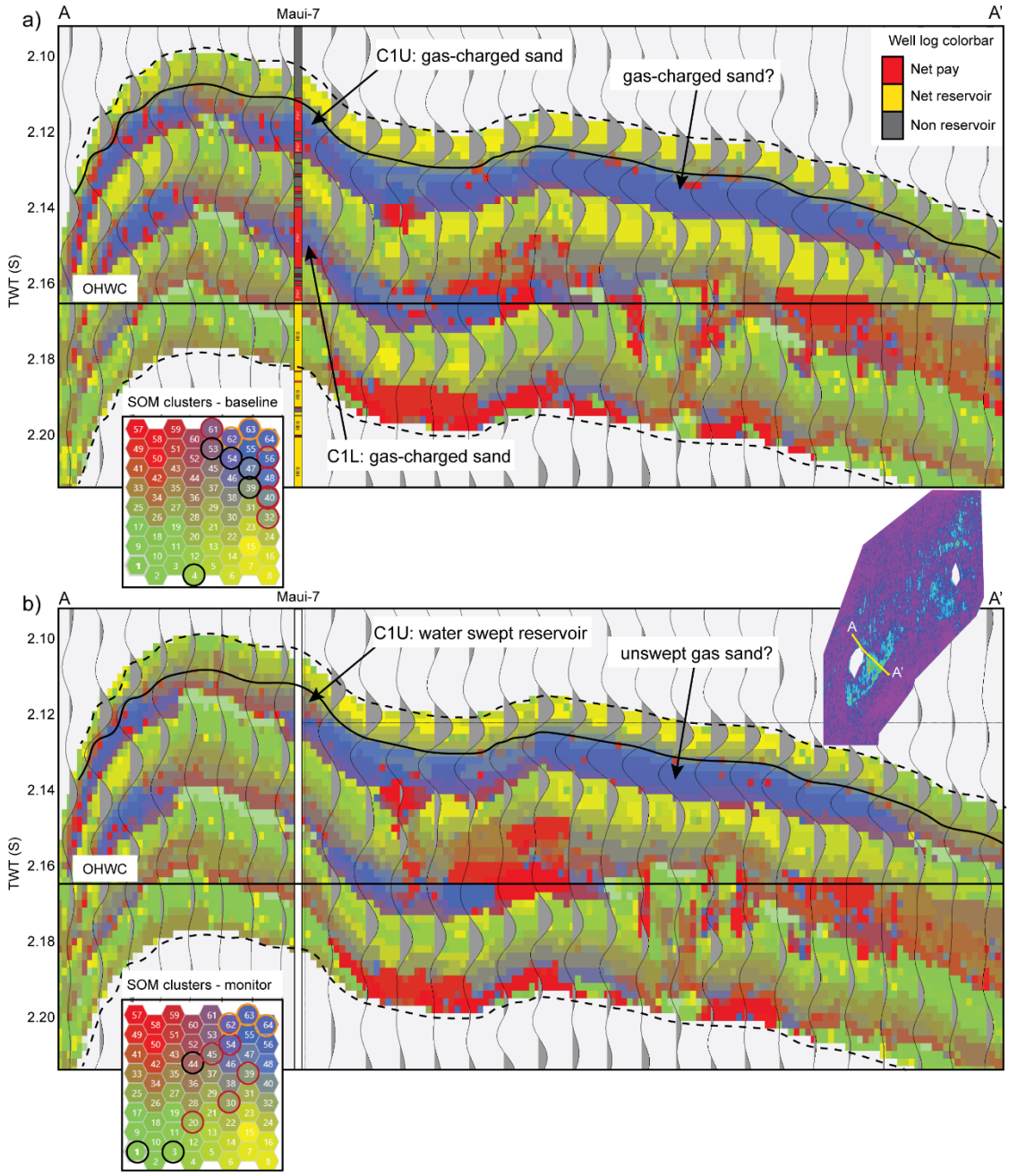

Figure 4. 13. Vertical sections extracted from SOM classification co-rendered with the quadrature phase components of (a) baseline and (b) monitor volumes and cross Maui-7 well, which display net pay and net reservoir discrete log. The red and black circles indicate SOM clusters of C1U and C1L that are correlated to gas-charged sand reservoir at the Maui-7 well. Orange circles in SOM legend indicate C1U to the east of Maui-7 well. The white bar in 2b) shows the Maui-7 well location. OHWC – approximate original hydrocarbon water contact. The OHWC is drawn as a flat line but in reality it is likely not be a flat in TWT. The inset slice is RMS amplitude map for the C1U reservoir extracted from the difference amplitude volume.

Figures 4.14 and 4.15 show 3D views of the baseline and monitor SOM clusters for the C1U sand reservoir and production wells that were producing from the reservoir between 1991 and 2002. Figure 4.14a shows the C1U classification volume with all neurons turned on. The figure shows that nearly the same SOM clusters were observed in both surveys at the edges of field where shelfal shale are deposited. However, there are subtle changes in the cluster patterns between the baseline and monitor SOM volumes over the Maui A and Maui B regions. I find that SOM classification volumes are useful for illuminating 4D changes in poor quality reservoirs within baffles units that cannot be imaged by the original 4D amplitude difference volumes (Figures 4.12 and 4.13). For instance, clusters N32 and N61 (Figures 4.14b and 4.14c respectively) are correlated to gas-charged poor quality reservoirs within FU1 and FU5 at the Maui-7 well. These clusters show smaller areal extent in the monitor SOM volume compared to the baseline SOM (red and cyan arrows) which suggests that the reservoir has been partially swept. Also, these clusters are not seen at Maui-7 well. However, N32 in Maui B north area covers a slightly larger area in the monitor SOM (orange arrow in Figure 4.14b) compared to baseline. This observation, which is likely due to better imaging in the monitor survey, agrees with the interpretation of the broadband and spectral instantaneous seismic attribute slices discussed earlier (Figure 4.10). The SOM cluster N40 (Figure 4.14d) is correlated to baffles and high speed reservoir flow units at the Maui-7 well and covers a slightly smaller area in the monitor SOM compared to the baseline. This suggests that the reservoir has been swept at Maui B east and south. The SOM cluster N48 (Figures 4.12 and 4.15) is correlated to gas-charged high speed and normal reservoir flow units at the Maui-7 well. This cluster shows a smaller areal extent in the monitor SOM compared to the baseline where the reservoir seems to be swept in Maui B east and south (Figure 4.15a).

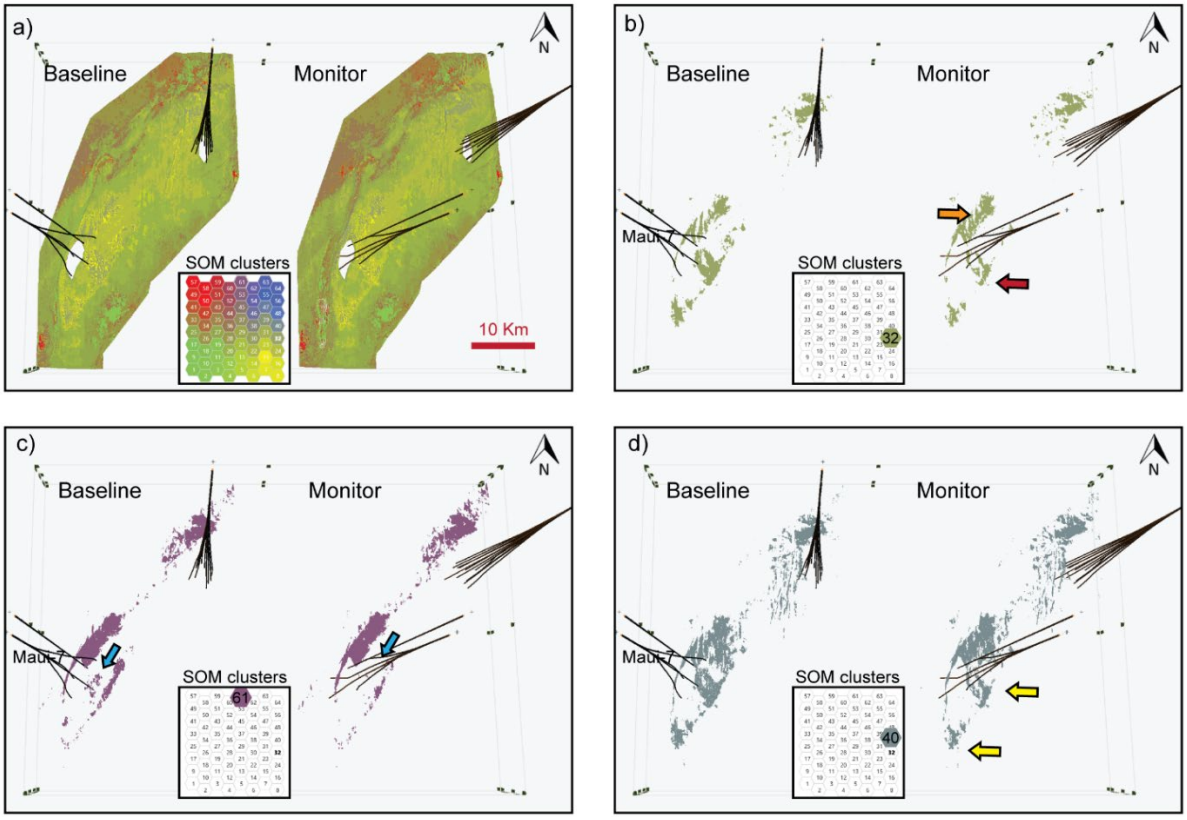

Figure 4. 14. 3D view of SOM clusters for the upper C1U Sand reservoir (C1U). (a) All SOM clusters are turned on. SOM clusters correlated to gas-charged flow units at Maui-7 well. (b) Neuron N32 correlated to poor quality reservoir within baffle (FU1), (c) N61 correlated to poor quality reservoir within baffle (FU5) and (d) N40 correlated to reservoir flow unit. Red, cyan and yellow arrows show changes in the cluster patterns (smaller pattern observed in the monitor SOM compared to the baseline) that might indicate swept areas of the reservoir. Orange arrow indicates slightly larger reservoir cluster in the monitor SOM compared to the baseline SOM slice. The light gray gaps in the baseline and monitor volumes in a) show exclusion areas underneath the Maui A and Maui B production platforms. The deviated lines shows the production wells that were producing mainly gas from the C1U Sand reservoir between 1991 and 2002 whereas the vertical line in Maui B region shows Maui-7 well.

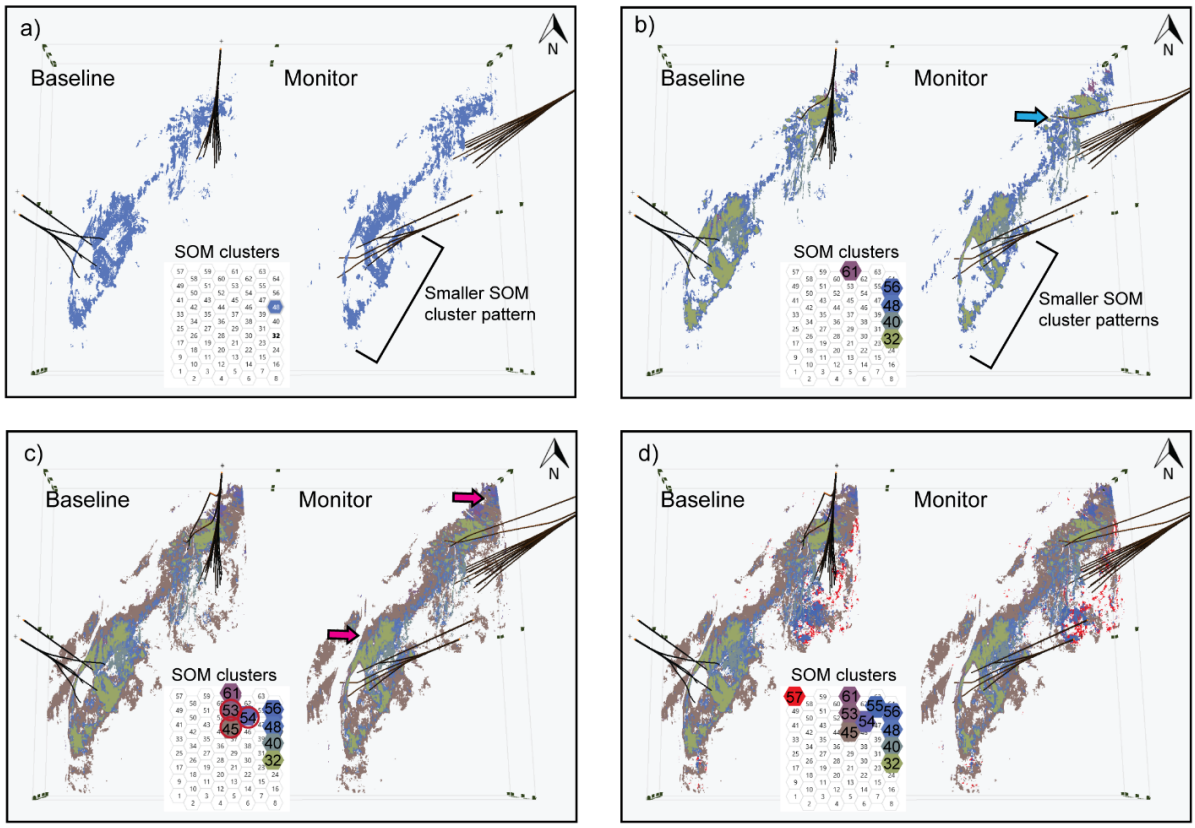

Figure 4. 15. 3D view of SOM clusters for the upper C1U Sand reservoir (C1U) with gas-charged reservoir penetrated by Maui-7 well clusters turned on. (a) N48 correlates to high speed and normal reservoir flow units. Gas-charged SOM clusters penetrated by (b) Maui-7 and MA-09B wells and (c) Maui-7, MA-02A and MA-09B. (d) SOM clusters shown in c) and clusters N57 and N55 that displays smaller patterns across Maui A south in the monitor SOM compared to the baseline SOM. The vertical line in Maui B region shows Maui-7 well whereas the deviated lines plotted in Maui A and Maui B regions shows the production wells from the C1U Sand reservoir. All the production wells were producing between 1991 and 2002 except MA-02A and MA-09B wells, which penetrated the C1U Sand reservoir in the Maui A west in 2008 and 2015, respectively. Pink arrows shows slightly larger reservoir portions clustered by SOM that agrees with the attribute slices displayed in Figure 4.8. Cyan arrow shows MA-09B well penetrated Maui-7 gas-charged sand SOM clusters.

The baseline SOM clusters correlated to the C1U gas-charged sand flow units at the Maui-7 well are displayed in Figure 4.15b. Those clusters seem to cover a smaller area in Maui B east and south and extend to the west side of Maui A where the MA-09B well, drilled in 2013, penetrated similar clusters (N40, N48, N56 and N63) to those defined at Maui-7 (cyan arrow). The MA-09B well found a thin gas sand (about 1 m in C1U) but the rest of the gas sands in the well seem to have been swept by production from the MA-02A well (Thangam, 2015). The MA-02A well, drilled in 2006, penetrated the C1U Sand reservoir clusters (N45, N54 and N53) and found unswept gas with the original gas-water contact (Telford and Murray, 2008). Figure 4.15c shows a 3D view of the Maui-7, MA-09B and MA-02A wells with the gas-charged reservoir clusters turned on (those circled in red on the SOM cluster legend). The reservoir clusters to the west side of the Maui A region seem to be connected and show the same patterns in the baseline and monitor SOM views.

To validate this observation, vertical sections extracted from baseline and monitor classifications and co-rendered with the corresponding quadrature-phase seismic volumes shown in Figure 4.16. These sections intersect the MA-09B, MA-02A and Maui-3 wells. The net pay and net reservoir discrete logs, calculated from the original wireline logs, are displayed for MA-02A and Maui-3. No wireline logs are available at MA-09B well. I observed that the gas-charged reservoir SOM clusters at MA-02A (circled in red in the SOM cluster legend) are in good communication with gas-charged clusters (circled in orange) identified at MA-09B. Comparing the baseline and monitor SOM classifications (Figures 4.16a and 4.16b respectively), the SOM patterns look similar, although subtle changes were observed to the east and west of MA-02A well. This suggests that there has been little or no production in the west side of Maui A between 1991 and 2002. When MA-02A was put on production in 2006, these

gas-charged sands seemed to have been swept (Thangam, 2015). This suggests that the SOM clusters (N32, N40, N48, N56, and N61) were gas-charged and unswept until sometime after 2002. The subtle changes in the baseline and monitor SOM clusters to the east and west of MA-02A well might have been caused by very small pressure depletion due to production from the Maui B region. I also note that the baseline and monitor SOM clusters (N28, N39, and N46; circled in cyan) penetrated by the Maui-3 well look very similar to each other. Maui-3 is an exploration well that was drilled into the C1 Sand reservoir in 1970. It is located about 2.2 km from the Maui A production platform from which there had been significant production prior to the acquisition of the baseline survey in 1991. It is likely that the reservoir was swept or partially swept before the baseline survey was acquired. The similarity in clusters for the baseline and monitor surveys in this area suggest little incremental production had occurred between 1991 and 2002. The gas-charged reservoir on the west of Maui A region appears to be compartmentalized and sealed by the Ihi fault, which is likely to have prevented the gas from migrating updip towards the Maui-3 well (Figure 4.16).

Focusing on bottom water rise within the C1L reservoir interval, at the Maui-7 well the baseline SOM clusters (N39, N47, N53, N54 and N4) are correlated to gas-charged sand (Figure 4.13). However, the monitor SOM classification show different clusters (N39, N45, N44, N1, and N3) in the C1L interval. This suggests that the C1L reservoir might have been swept by production wells located near the Maui-7 well. Water breakthrough in 2003 was observed at MB-12 (Figure 4.7), just updip from Maui-7, validating this interpretation.

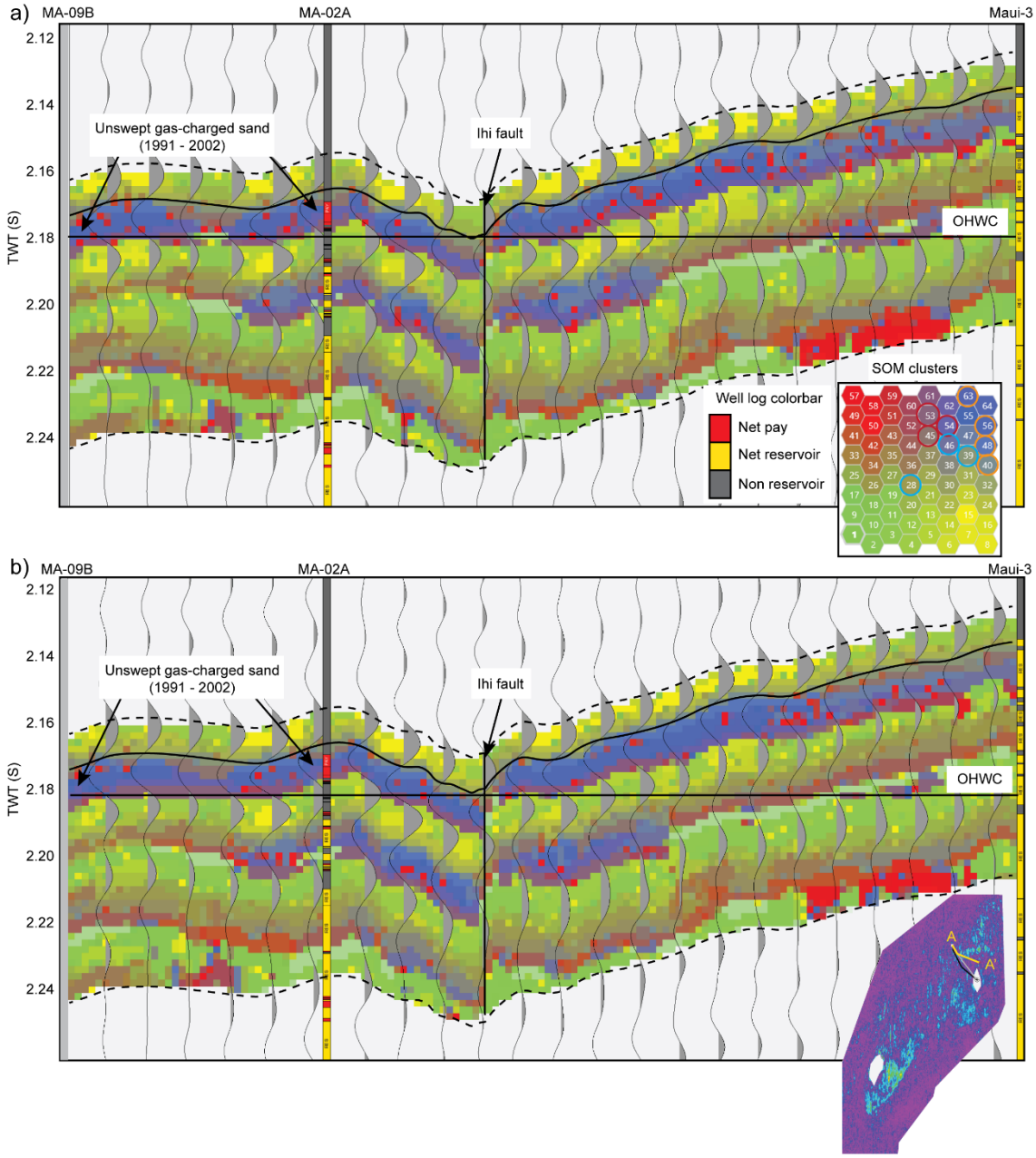

Figure 4. 16. Vertical sections extracted from SOM classification co-rendered with the quadrature phase components of (a) baseline and (b) monitor volumes. These sections cross the MA-09B, MA-02A and Maui-3 wells, which display net pay and net reservoir discrete logs. Black and white deviated lines in the RMS map indicate the MA-09B and MA-02A well paths. Orange and red circles indicate gas-charged sand reservoir penetrated by MA-09B and MA-02A wells, respectively. Cyan circles refer to the C1U Sand reservoir penetrated by Maui-3 well. The gray bars to the left of a) and b) show the location of MA-09B. No well logs are available for MA-09B. OHWC – approximate original hydrocarbon water contact. The OHWC is drawn as a flat line but in reality it is likely not be a flat in TWT. The inset slice is RMS amplitude map for the C1U reservoir extracted from the difference amplitude volume.

Figure 4.17 shows a vertical section which crosses the MB-12 well (drilled in 1993), extracted from the baseline and monitor SOM classification volumes and co-rendered with the quadrature components of the baseline and monitor data. I note that the baseline and monitor SOM clusters are correlated to the gas-charged sands within the C1U Sand reservoir. The same clusters (N4, N31, N39, N45, N53, and N54; denoted by the orange circles in the SOM legend) were observed for the baseline and monitor SOM volumes. This suggests that there was little or no water sweep in the C1U Sand reservoir near the MB-12 well between 1991 and 2002. This agrees with the production data from this well.

On the other hand, the baseline and monitor SOM clusters look different for the C1L Sand reservoir. At the MB-12 well, there is a thin oil-rim about 2 m thick (Figure 4.7). The oil rim is well below the seismic and SOM resolution, so it is hard to differentiate and/or resolve gas versus oil. In the baseline SOM classification volume, the C1L hydrocarbon-charged sands correlate to clusters N21, N28, N36, N41, and N1 and cluster N2 correlates to the hydrocarbon-water contact (Figure 4.17). For the monitor, the upper part of the C1L interval (gas-charged sands) is correlated to SOM clusters N28, N37, and N41, which are very similar to those observed in the baseline SOM volume. However, different clusters (N50 and N52) were observed in the lower part of C1L reservoir for the monitor SOM volume. This suggests that the lower part of the C1L interval might have been water swept. The monitor SOM classification clearly shows the change in the hydrocarbon-water contact. As the reservoir was being produced, the acoustic impedance in the reservoir increased because of the water sweep. Thus, the seismic response of the reservoir changes. This results in a change in the cluster patterns which shows a coning affect along the borehole and extending updip towards the rest of the production wells (Figure 4.17b). The monitor SOM volume clearly shows cluster patterns

along the borehole that cannot be imaged by the monitor seismic data or by the 4D amplitude difference. The red clusters may also in part due to subtle changes in the seismic response because of subtle pressure draw down near the wellbore (Figure 4.17b).

Figure 4.18a is a 3D view of the baseline and monitor SOM classification volumes for the C1L interval with all neurons turned on. Figure 4.18b shows the SOM view with only the neurons correlated to reservoir at Maui-7 and MB-S12 turned on. The figure shows that, compared to the baseline, the reservoir clusters cover a smaller area in the monitor SOM volume in Maui B east and south (orange and cyan arrows). But, the monitor SOM clusters in Maui B north cover a larger area compared to the baseline results (yellow arrow in Figure 4.18b). I attribute this to better data quality in the monitor compared to the baseline amplitude data. As a result, the monitor SOM volumes illuminate the reservoir facies better than in the baseline volume. Fully understanding the SOM clusters of the C1L reservoir across the Maui B region is challenging because C1L production occurs from only the MB-11 and MB-12 wells. The MB-11 well was drilled in the seismic data gap zone and cannot be used in the calibration process of the SOM classification volumes. Thus, only the SOM clusters penetrated by Maui-7 and MB-12 were used to understand 4D signal at this interval.

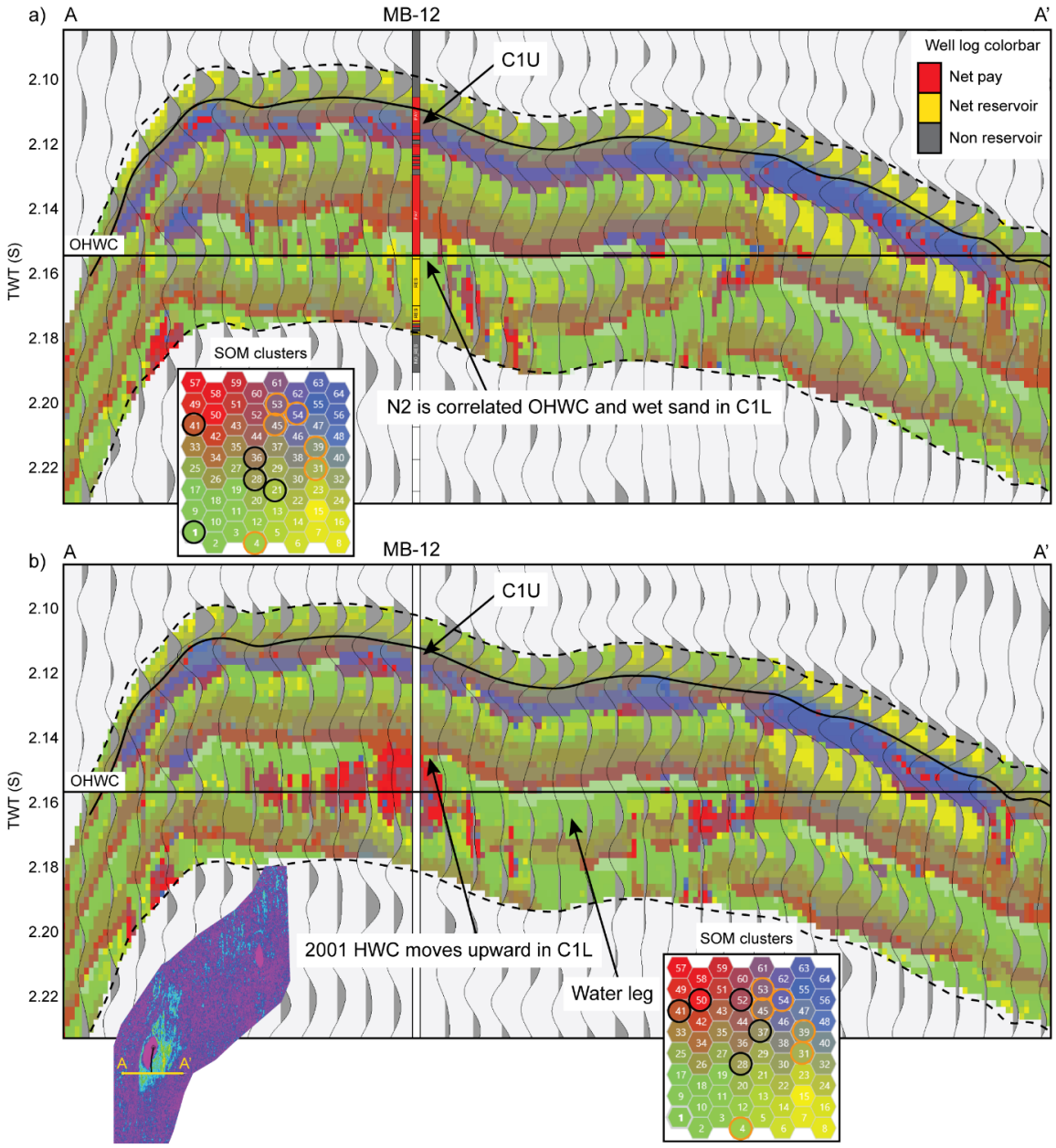

Figure 4. 17. Vertical sections extracted from SOM classification co-rendered with the quadrature phase of (a) base-line and (b) monitor volumes. These sections cross the MB-12 well, which display net pay and net reservoir discrete logs. HWC - hydrocarbon water contact; C1U and C1L - Upper and Lower C1 Sand reservoir. The orange and black circles in the SOM cluster legend (inset) indicate clusters correlate to the C1U and C1L reservoir. The white bar in 2b) shows MB-12 location. OHWC – approximate original hydrocarbon water contact. The OHWC is drawn as a flat line but in reality it is likely not be a flat in TWT. The inset slice is the RMS amplitude for the C1L reservoir extracted from the difference amplitude volume.

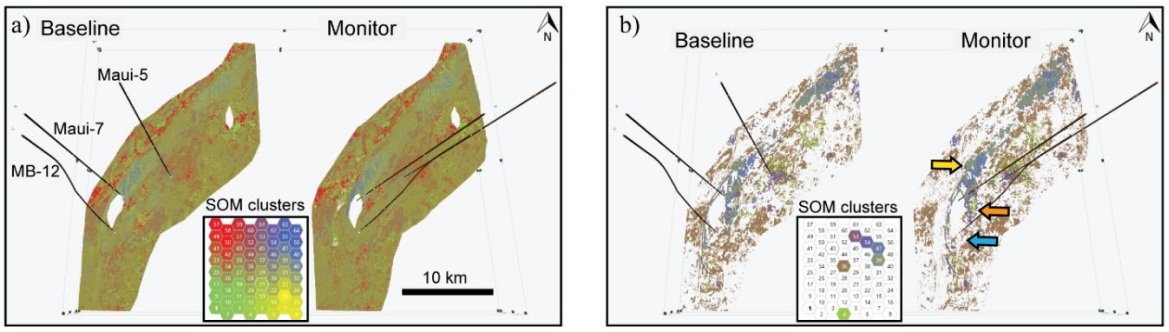

Figure 4. 18. 3D view of SOM classification for the lower C1 Sand reservoir (C1L). (a) All SOM clusters are turned on. (b) SOM clusters correlated to gas-charged sand at Maui-7 and MB-12. Orange and cyan arrows refer to SOM clusters disappeared or cover smaller area in the monitor SOM compared to the baseline SOM. Yellow arrow denote SOM clusters that cover larger area in the monitor compared to the baseline SOM slice.

4.10 Geobody extraction and volumetric calculations

In this study, I have shown a workflow that enables us to combine multiple seismic attributes volumes at a seismic-sample scale into SOM classification volumes. Analysis of the SOM clustered volumes facilitates the 4D interpretation of reservoir below tuning thickness (i.e., down to 4 m thick reservoir zones). Geobodies can be created from SOM clusters that are tied to the well and production data. Once the geobodies are generated, the original hydrocarbon and recoverable gas volumes for the baseline and monitor conditions can be calculated by incorporating information from the wells that penetrated these geobodies.

I have discussed the baseline SOM clusters (N32, N40, N48, N56, and N61) for the C1U Sand reservoir calibrated by the Maui-7 well. Geobodies can be generated by connecting the seismic samples within those SOM clusters (Figures 4.19a and 4.19b). In Figures 4.19a and 4.19b, the geobodies created for each cluster have the same color as the cluster. For example, all of the green geobodies are generated from cluster N32. The sizes of the monitor geobodies are smaller than the baseline geobodies. The difference in their volumes gives a qualitative measure of the produced volume between 1991 and 2002 (Figures 4.19a and 4.19b). The geobodies remaining in the monitor survey may indicate undrained parts of the C1U reservoir. The red arrows in Figure 4.19 indicate the swept areas within the in Maui A south reservoir. However, most of the production appears to have occurred in the Maui B region where I see the greatest decrease in the volume of reservoir geobodies between baseline and monitor. There seems to have been less production at the south of the Maui A region.

To estimate the amount of water sweep due to production between 1991 and 2002, I calculated the recoverable gas volumes for the baseline and monitor geobodies. Those computations require interval velocity (Vint) to calculate geobody thickness, net to gross ratio (N/G), porosity (PHI) and water saturation (Sw) to be known for each SOM cluster (Table 1). Assuming the same clusters of the baseline and monitor volumes have similar reservoir properties (e.g., the N32 cluster is assumed to have similar reservoir properties in the baseline and monitor SOM volumes), then the original reservoir properties at the Maui-7 well (the yellow arrow in Figure 4.19) can be used in the volumetric calculations. Calculating the size of the geobodies and their associated recoverable gas volumes for the baseline and monitor SOM volumes provides a quantitative measure of the amount of swept (and produced) hydrocarbon and the amount of recoverable gas reserves (i.e., unswept reservoirs).

$$RG = GRV * N/G * PHI * (1 - SW) * GEF * RF \quad (1)$$

where RG represents the recoverable gas, GRV is the gross rock volume, N/G is the net-to-gross, PHI is the porosity, SW is the water saturation, GEF is gas expansion factor and RF is the recovery factor.

Table 4.3 shows the recoverable gas volumes of the C1 Sand reservoir based on Maui-7 well parameters for the baseline and monitor. The difference is the volume of reservoir swept by water due to production between 1991 and 2002. I observed that the calculated recoverable gas volume that was withdrawn between 1991 and 2002 is higher for geobodies correlated to high speed and normal reservoir flow units (N40 and N48; Table 4.3) compared to those calculated for poor reservoir within baffle flow units (N32 and N61; Table 4.3).

Table 4. 3. C1U reservoir properties and recoverable gas volumes calculated from the baseline and monitor SOM classification geobodies. The gas expansion factor (GEF) used in the computation is 230

CLUSTER	VINT (M/S)	PHI (FRAC)	SW (FRAC)	N/G	RF	RG91 (BCF)	RG02 (BCF)	RG91–RG02 (BCF)
N32	3805	0.2	0.2	0.41	0.5	24	20	4
N40	3690	0.19	0.19	1	0.7	93	79	14
N48	3683	0.18	0.21	1	0.7	136	120	16
N56	3527	0.18	0.29	0.74	0.5	77	74	3
N61	3471	0.17	0.33	0.83	0.5	35	32	3

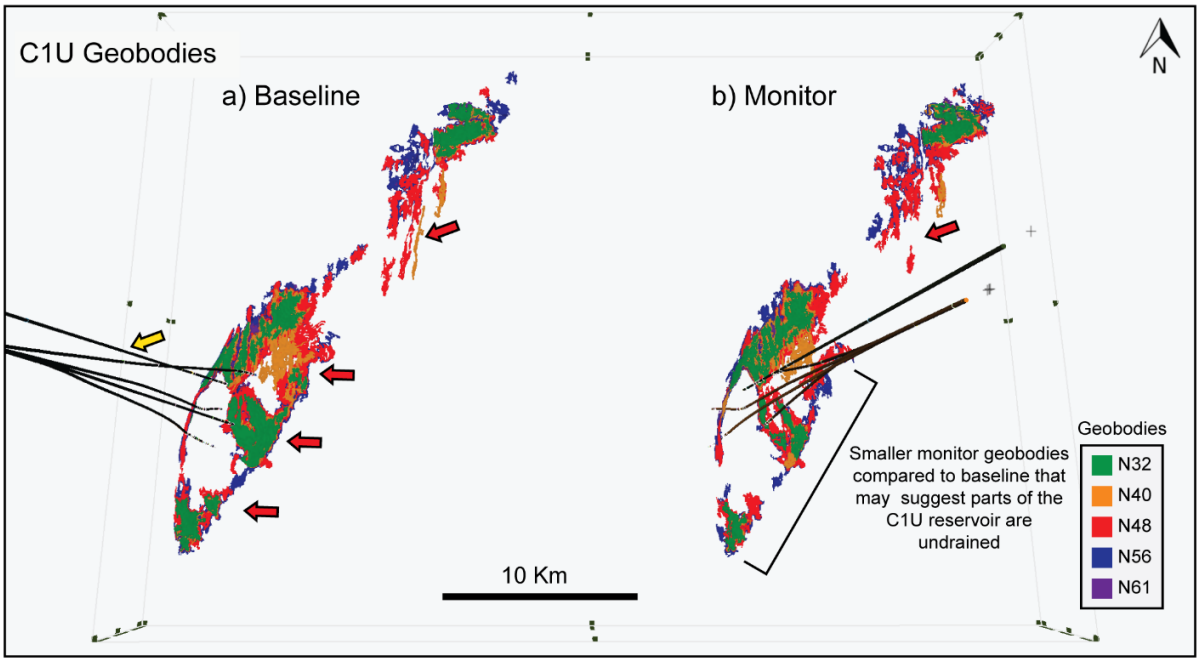

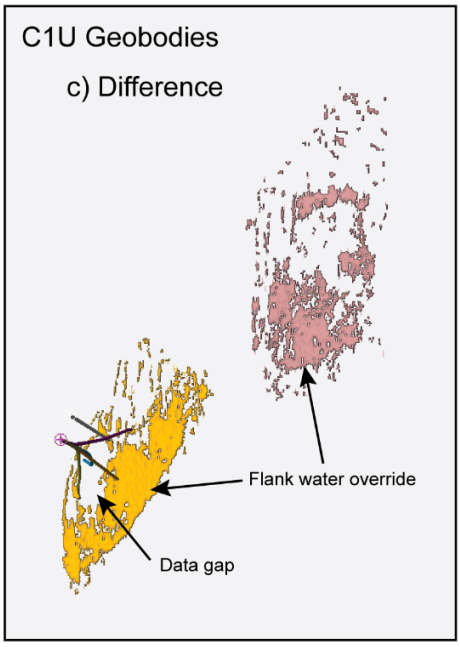

Figure 4. 19. 3D view of geobodies extracted for the C1U Sand reservoir from the baseline (left) and monitor (right) SOM classification volumes. The red arrows refer to water swept areas of the reservoir. The monitor geobodies cover smaller areas and may suggest the undrained parts of the C1U reservoir. The deviated lines indicate the production wells that were producing from the C1U sand reservoir. Vertical line (yellow arrow) refers to Maui-7 well. (c) 3D view of geobodies extracted for the C1U Sand reservoir from the quadrature component volume.

4.11 Discussion

The SOM classifications of the baseline and monitor volumes are useful to monitor water saturation changes within thin reservoir intervals (below seismic resolution) of very good and poor reservoir quality sands. Compared to original 4D amplitude volumes, SOM classification shows more details that illuminate flank water override and changes in the hydrocarbon water contact. However, the baseline SOM classification may not be useful in discriminating commercial gas-charged reservoir and from residual gas saturated reservoirs for the same geology. For example, at the Maui-7 and Maui-5 wells, the baseline SOM classifies both gas-charged and wet, high speed and normal reservoir flow units as N54 and N53 (Figure 4.12) in the C1L. Closer investigation of those flow units, finds that they have the same facies (clean sand form estuarine channels) and similar porosity ranges between 18-21% (see Chapter 3). At Maui-7, the monitor SOM shows different clusters (N39, N45, N44, N1, and N3) compared to the baseline SOM for the C1L interval. However, similar baseline and monitor SOM clusters are observed at the Maui-5 well (Figure 4.12). This suggests that the 4D response is a bit more complicated than simply a water saturation change. This might have been caused in part by subtle pressure depletion.

Although SOM is an unsupervised machine learning technique that classifies natural clusters within multiple input seismic attribute volumes, incorporating as many wells as possible in the interpretation process is vital. The absence of a logged well penetrating the C1 Sand reservoir in the Maui A region that is timed with either the 1991 or 2002 seismic data limits our understanding of the production-related changes in this area. I observed subtle changes in SOM cluster patterns in the southern Maui A region (Figure 4.15d) but those clusters cannot be calibrated to well data.

As I mentioned previously, I do not have sufficient released data from production wells in the field. I used the Maui-7 well to generate geobodies and calculated recoverable gas assuming that the same clusters have the same properties, which might not accurate. Including more wells in the analysis would allow a better understanding of the changes in water saturation, interval velocity and net-to-gross ratio used to populate the SOM-derived geobodies that would provide more accurate reserve estimates. Although, the calculated difference in the recoverable gas (40 BCF) from the baseline and monitor geobodies is smaller than the actual production (416 BCF), I only used the clusters penetrated by the Maui-7 well. There are also large volumes of the reservoir underneath the Maui B production platform and in Maui B south that I could not include in our reserve estimate computation due to missing data in the gap zone. Most of the production wells for which I have data are drilled in this area. The calculated recoverable gas for geobodies computed from the difference volume is 252 BCF. This represents the amount of gas withdrawn from the C1U reservoir due to production between 1991 and 2002. The computed gas volume from the difference volume is bigger than calculated difference in gas volumes computed from the baseline and monitor geobodies because the geobodies extracted from the difference volume are bigger than the SOM-derived geobodies (Figure 4.19).

However, the gas volume computed on the amplitude difference is smaller than the production data because I could not consider the volumes withdrawn within the data gaps underneath the Maui B platform. Also, the poor reservoir quality interval do not exhibit 4D amplitude difference signal so, I could not include those reservoirs in the volumetric gas computation from the 4D difference volume.

The data quality of the 4D seismic volumes controls the SOM classification results. The repeatability of the 4D seismic data of Maui field is good. However, the 2002 monitor seismic data shows slightly better imaging for the reservoir facies in Maui B north and the northern part of Maui A compared to baseline volume (as illustrated by the pink arrows in Figure 4.10b). This results in SOM clusters that cover slightly larger areas in the monitor compared baseline volume (orange arrows in Figure 4.14b) which are similar to the facies illuminated in the seismic attribute slices (pink arrows in Figure 4.10b).

Only full-stack seismic volumes are available for this study. And only a few production wells were released for research. Thus, in this study, I was limited in terms of the available seismic data and wells that could be used to calibrate and interpret baseline and monitor SOM classifications. The same workflow could be applied to seismic attributes extracted from partial angle stack data or to partial angle stack 4D difference volumes. Time-lapse well logs, if they were come to be available, could be used to monitor changes in the hydrocarbon water contact or flank water override and would greatly assist SOM interpretation and calibration. The water saturation changes dominate the 4D changes in the analysis of the C1 Sand reservoir, which is considered in this study. This methodology could be applied to compacting reservoirs and using angle stacks could possibly distinguish between saturation and pressure changes.

4.12 Conclusions

Time-lapse seismic attributes were used to constrain the history matching of reservoir simulation models, which helps make better reservoir management decisions. Understanding reservoir heterogeneities and the associated 4D responses is a critical part of this process. In this chapter, I propose a machine learning workflow that enables us to combine multiple 4D spectral instantaneous seismic attribute volumes into merged classification volumes. Calibrating the SOM baseline and monitor classification volumes to well data, production data and 4D seismic attributes helps to identify clusters that are meaningful in terms of production reservoir facies. Changes in the cluster patterns between baseline and monitor surveys suggest production-related changes, primarily caused by water replace gas. The 4D SOM classification volumes show internal reservoir heterogeneity and illuminate 4D changes for good and poor quality reservoir and identify thin baffles. Thus, compared to the 4D seismic amplitude volumes, the 4D SOM volumes better show the changes in the flank water over ride and bottom water rise. Geobodies can be generated from the production-related SOM clusters of the baseline and monitor classifications. Computing the recoverable gas volumes for the baseline and monitor geobodies and calibrating those volumes to production data aids in estimating the remaining recoverable gas but there are uncertainties that cannot be fully addressed given this dataset. The SOM identifies natural cluster patterns in multiple 4D spectral instantaneous attribute volumes. However, determining the meaning of the clusters requires calibration using well data. Incorporating as many wells as possible is critical for accurate geobody extractions and volumetric calculations.

5 Conclusions

Over the last few decades, geoscientists have been using machine learning techniques in different disciplines such as seismic processing and interpretation, well log predictions, remote sensing applications and many others. This dissertation focuses on using machine learning as an aid to reservoir characterization and time-lapse seismic studies, with application to the Maui field, Offshore Taranaki basin of New Zealand.

Imaging subtle faults is critical for reservoir exploration and developments studies. These small faults may act as conduits or baffles that control the hydrocarbon migration path-ways inside a petroleum reservoir. However, these subtle faults can be overlooked in the interpretation of seismic amplitude data. Seismic attributes aid in illuminating small faults. However, over the past few years, dozens of seismic attributes have been developed to an extent that it is difficult for interpreters to select which attribute to use. I investigated typical seismic attributes that are sensitive to faults and fractures by using individual and multi-attribute analyses. I find integrating the geological information within multiple seismic attribute volumes helps to illuminate small faults. I propose a workflow to enable seismic interpreters to select best attributes that show small faults. And then combine multiple seismic attribute volumes by using multi-attribute display and machine learning clustering technique such as self-organizing maps (SOM).

Understanding reservoir distribution, quality, and heterogeneity and illuminating stratigraphic baffles are key information to be considered in static reservoir models. We usually tend to understand the reservoir properties and quality through petrophysical and rock typing analysis at the well locations. However, interpolating and extrapolating the reservoir facies with their associated rock quality and stratigraphic baffles away from well controls is critical for realistic model building. It is challenging to image small petrophysical changes or thin stratigraphic baffles from conventional seismic amplitude data. I investigated typical seismic attributes that are sensitive to reservoir properties and thickness variations. I provide a workflow to integrate the reservoir information within multiple spectral instantaneous attributes into one classification volume by using SOM method. Calibrating this SOM clustered volume to well data (i.e., net reservoir and flow units discrete logs) aids in illuminating thin reservoir and stratigraphic baffles; hence, understanding the reservoir quality and heterogeneity across the whole field.

Time-lapse seismic data are usually acquired during the field development phase to aid in understanding the fluid movements and constrain history-matched and simulation models. However, the 4D seismic data are subject to seismic interference and tuning effects. Incorporating thin reservoir and stratigraphic baffles in reservoir simulation models is critical to achieve a good match between the modeled 4D response and observed 4D seismic in a timely manner. Although Bayesian inversion methods help to quantify the reservoir properties variations (i.e., water saturation and/or pressure changes) due to production, these techniques cannot discriminate between shale and thin bedded sand-shale intervals due to the seismic resolvability issues.

Using the 4D seismic data of Maui field, I developed a machine learning workflow to integrate the preproduction and postproduction reservoir information within eight 4D spectral instantaneous attributes into merged classification volumes. The baseline and monitor classification volumes are calibrated to well data, production data and 4D volumes to identify meaningful clusters, which show changes in cluster patterns that are correlated to water saturation changes due to water replacing gas under strong water drive mechanism. SOM classification volumes of 4D seismic data aid in illuminating very good to poor quality reservoirs and baffles that are below the seismic resolution with their associated 4D responses. I also generated geobodies from the baseline and monitor SOM clusters and then I calculate the recoverable gas from those geobodies. The baseline and monitor reserves are compared to each other and to the production data for validation purposes. There are uncertainities in the computed recoverable gas volumes that cannot be fully addressed given this dataset.

6 Future work

There is a potential to extend the work presented in this dissertation. For the subtle fault detection, it may be useful to run different geometric attributes on stochastic inverted impedance volume. This might better illuminate small faults and fractures than the broadband processed seismic volumes. Given enough labelled data, convolutional neural network (CNN) can be applied to carefully selected attributes that show anomalous features at the inferred fault positions. This might help the CNN to detect low angle, thrust and/or listric faults.

Similarly, instantaneous and spectral decomposition analysis can be tested on stochastic inverted impedance volume. This may better illuminate small stratigraphic details than the broadband processed seismic volume. The same machine learning workflow proposed in Chapter 3 can be applied on stochastic inverted impedance volume. Additionally, in the presence of enough labeled data and well data, CNN can be applied on the proposed eight spectral combination of attributes proposed in Chapter 3.

I find SOM is useful for 4D seismic studies and reservoir monitoring. I applied the 4D machine learning workflow in the baseline and monitor seismic volumes. It would be useful to test the same machine learning workflow on difference amplitude volume and calibrate the classification volume to time-lapse logs whenever, these logs become available. Alternatively, fluid subsituted models of the original logs based on the production data can be used in the SOM calibration.

In Chapter 4, I applied spectral decomposition analysis on the 4D broadband processed seismic volumes in order to focus on the reservoir level. The results look promising and encouraging. It was necessary to test SOM on angle stacks seismic volumes that enabled better separation between the geology and fluid effect. SOM seems to be sensitive to saturation and subtle pressure changes. It would be useful testing SOM on synthetic models to understand in details and quantify the SOM sensitivity to those reservoir properties' changes. In this study, I used the C1 Sand reservoir of Maui field in offshore Taranaki basin. This reservoir is competent and produces under strong water drive. Water saturation changes dominates the 4D changes and the reservoir is less compacted. More work needs to be done considering using data for compacted reservoirs. In the presence of 4D angle stacks and enough well data, deep neural network models can be tested for water saturation and pressure changes prediction. In case of absence of enough wells, more research could be done to generate synthetic data that mimic field geology and production history. Supervised deep learning methods can then be trained on these synthetic data and applied to field data in order to quantify production-related changes (i.e. water saturation/pressure changes).

BIBLIOGRAPHY

Al-Dossary, S., and K. J. Marfurt, 2006, 3D volumetric multispectral estimates of reflector curvature and rotation: Geophysics, 71, 5, P41–P51.

Amaefule, J. O., M. Altunbay, D. Tiab, D. G. Kersey, and D. K. Keelan, 1993, Enhanced reservoir description: using core and log data to identify hydraulic (flow) units and predict permeability in uncored intervals/ wells: SPE Annual Technical Conference and Exhibition, 205–220.

Aqrawi, A. A., and T. H. Boe, 2011, Improved fault segmentation using a dip guided and modified 3D Sobel filter: 81th Annual International Meeting, SEG, Expanded Abstracts, 999–1003.

Attia, A. M., and H. Shuaibu, 2015, Identification of barriers and productive zones using reservoir characterization: International Adanced Research Journal In Science, Engineering and Technology, 2, 12, 8–23.

Avseth, P., T. Mukerji, and G. Mavko, 2010, Quantitative seismic interpretation: applying rock physics tools to reduce interpretation risk: Cambridge University Press, 408 p.

Bahorich, M. S., and S. L. Farmer, 1995, 3-D seismic discontinuity for faults and stratigraphic features: The coherence cube: The Leading Edge, 14, 10, 1053–1058.

Baldwin, J. L., R. M. Bateman and C. L. Wheatley, 1990, Application of a neural network to the problem of mineral identification from well logs: Petrophysics, 31, 5, 279-293.

Barnes, A. E., 2006, A filter to improve seismic discontinuity data for fault interpretation: Geophysics, 71, 3, P1–P4.

Barnes, A. E., 2016, Handbook of poststack seismic attributes: Geophysical Reference Series, no. 21, 254 p.

Barnes, A. E., and K. J. Laughlin, 2002, Investigation of methods for unsupervised classification of seismic data: 72th Annual International Meeting, SEG, Expanded Abstracts, 2221-2224.

Baur, J. R., P. R. King, T. Stern, and B. Leitner, 2010, Development and seismic geomorphology of a Miocene slope channel megasystem, offshore Taranaki Basin, New Zealand, Seismic Imaging of Depositional and Geomorphic Systems: SEPM Society for Sedimentary Geology, 618–649.

Branets, L. V., S. S. Ghai, S. L. Lyons, and X. H. Wu, 2008, Challenges and technologies in reservoir modeling: Communications in Computational Physics, 6, 1, 1–23.

Brown, A. A., 2011, Interpretation of three-dimensional seismic data: AAPG Memoir 42, SEG Investigations in Geophysics, no. 9, 665 p.

Bryant, I. D., C. W. Greenstreet, and W. R. Voggenreiter, 1995, Integrated 3-D geological modeling of the C1 Sands reservoir, Maui Field, offshore New Zealand: AAPG Bulletin Bulletin, 79, 3, 351–374.

Bryant, I. D., M. G. Marshall, C. W. Greenstreet, W. R. Voggenreiter, J. M. Cohen, and J. F. Stroeman, 1994, Integrated geological reservoir modelling of the Maui Field Taranaki Basin, New Zealand: 1994 New Zealand Oil Exploration Conference Processings, 256–281.

Buland, A., and Y. El Ouair, 2006, Bayesian time-lapse inversion: Geophysics, 71, 3, R43–R48.

Calvert, R., 2005, Insights and methods for 4d reservoir monitoring and characterization: Distinguished Instructor Short Course, no. 8, 219 p.

Cao, J., and B. Roy, 2017, Time-lapse reservoir property change estimation from seismic using machine learning: Leading Edge, 36, 3, 234–238.

Castagna, J. P., S. Sun, and R. W. Siegfried, 2003, Instantaneous spectral analysis: detection of low-frequency shadows associated with hydrocarbons: Leading Edge, 22, 2, 120-127.

Chopra, S., and K. J. Marfurt, 2006, Seismic attribute mapping of structure and stratigraphy: SEG/EAGE Distinguished Instructor Short Course, no. 9, 234 p.

Chopra, S., and K. J. Marfurt, 2007, Seismic attributes for prospect identification and reservoir characterization: SEG Geophysical Development Series no. 11, 464 p.

Chopra, S., and K. J. Marfurt, 2019, Multispectral, multiazimuth, and multioffset coherence attribute applications: Interpretation, 7, 2, SC21–SC32.

Coléou, T., M. Poupon, and K. Azbel, 2003, Unsupervised seismic facies classification : A review and comparison of techniques and implementation: The Leading Edge, 942–953.

Das, V., A. Pollack, U. Wollner, and T. Mukerji, 2018, Convolutional neural network for seismic impedance inversion: 88th Annual International Meeting, SEG, Expanded Abstracts, 2071–2075.

Dewett, D. T., and A. A. Henza, 2016, Spectral similarity fault enhancement: Interpretation, 4, 1, SB149–SB159.

Di, H., and D. Gao, 2016, Improved estimates of seismic curvature and flexure based on 3D surface rotation in the presence of structure dip: Geophysics, 81, 2, IM13–IM23.

Doyen, P. M., 2007, Seismic reservoir characterization: an earth modelling perspective, EAGE Publications, 256 p.

Dubois, M. K., G. C. Bohling, and S. Chakrabarti, 2007, Comparison of four approaches to a rock facies classification problem: Computers and Geosciences, 33, 5, 599–617.

Francesconi, A., F. Bigoni, P. Balossino, N. Bona, F. Marchini, and M. Cozzi, 2009, Reservoir rock types application - Kashagan: SPE/EAGE Reservoir Characterization and Simulation Conference - Overcoming Modeling Challenges to Optimize Recovery, 359–375.

Funnell, R. H., V. M. Stagpoole, A. Nicol, S. D. Killops, A. G. Reyes, and D. Darby, 2001, Migration of Oil and Gas into the Maui Field, Taranaki Basin, New Zealand: Eastern Australasian Basins Symposium - A Refocused Energy Perspective for the Future, 121–130.

Gao, D., 2013, Integrating 3D seismic curvature and curvature gradient attributes for fracture characterization: methodologies and interpretational implications: Geophysics, 78, 2, O21–O31.

Gao, D., 2011, Latest developments in seismic texture analysis for subsurface structure, facies, and reservoir characterization: A review: Geophysics, 76, 2, W1–W13.

Gassmann, F., 1951, Elastic waves through a packing of spheres: Geophysics, 16, 4, 673–685.

Gersztenkorn, A., and K. J. Marfurt, 1999, Eigenstructure-based coherence computations as an aid to 3-D structural and stratigraphic mapping: Geophysics, 64, 5, 1468–1479.

Gouveia, W. P., D. H. Johnston, A. Solberg, and M. Lauritzen, 2004, Jotun 4D: Characterization of fluid contact movement from time-lapse seismic and production logging tool data: The Leading Edge, 23, 11, 1187–1194.

Grana, D., and T. Mukerji, 2015, Bayesian inversion of time-lapse seismic data for the estimation of static reservoir properties and dynamic property changes: Geophysical Prospecting, 63, 3, 637–655.

Grochau, M., and P. Jilinski, 2016, 4D seismic spectral decomposition over a pre-salt carbonate reservoir: A feasibility study: 86th Annual International Meeting, SEG, Expanded Abstracts, 5547–5551.

Gunter, G. W., J. M. Finneran, D. J. Hartmann, and J. D. Miller, 1997, Early determination of reservoir flow units using an integrated petrophysical method: SPE Annual Technical Conference and Exhibition, 373–380.

Guo, G., M. A. Diaz, F. Paz, J. Smalley, and E. A. Waninger, 2007, Rock typing as an effective tool for permeability and water-saturation modeling: A case study in a clastic reservoir in the Oriente basin: SPE Reservoir Evaluation and Engineering, 10, 6, 730–739.

Hall, B., 2016, Facies classification using machine learning: Leading Edge, 35, 10, 906–909.

Hami-Eddine, K., P. Klein, and L. Richard, 2009, Well facies based supervised classification of prestack seismic: Application to a turbidite field: 79th Annual International Meeting, SEG, Expanded Abstracts, 1885–1889.

Hami-Eddine, K., P. Klein, L. Richard, D. Elabed, E. Chatila, and A. Furniss, 2011, Multivariate supervised classification, application to a New Zealand Offshore Field: Presented at 31st Annual International Meeting, Gulf Coast Section of Society of Economic Paleontologists and Mineralogists, 1-23.

Hami-Eddine, K., L. Richard, and P. Klein, 2013, Integration of lithology uncertainties in net volume prediction using democratic neural network association: 83th Annual International Meeting, SEG, Expanded Abstracts, 2495–2499.

Hami-Eddine, K., P. Klein, L. Richard, B. De Ribet, and M. Grout, 2015, A new technique for lithology and fluid content prediction from prestack data: An application to a carbonate reservoir: Interpretation, 3, 1, SC19–SC32.

Hampson, D. P., J. S. Schuelke, and J. A. Quirein, 2001, Use of multiattribute transforms to predict log properties from seismic data: Geophysics, 66, 1, 220–236.

Haque, A. E., M. A. Islam, and M. Ragab Shalaby, 2016, Structural modeling of the Maui gas Field, Taranaki Basin, New Zealand: Petroleum Exploration and Development, 43, 6, 965–975.

Hart, B. S., 2008, Channel detection in 3-D seismic data sing sweetness: AAPG Bulletin, 92, 6, 733–742.

Haskell, T. R., 1991, An analysis of Taranaki basin hydrocarbon migration pathways: some questions answered: Petroleum Exploration in New Zealand News, 32, 19–25.

Helgerud, M. B., A. C. Miller, D. H. Johnston, M. S. Udoh, B. G. Jardine, C. Harris, and N. Aubuchon, 2011, 4D in the deepwater Gulf of Mexico: Hoover, Madison, and Marshall fields: Leading Edge, 30, 9, 1008–1018.

Henderson, J., S. J. Purves, and G. Fisher, 2008, Delineation of geological elements from RGB color blending of seismic attribute volumes: Leading Edge, 27, 3, 342–350.

Higgs, K, P. King, R. Skyes, E. Crouch, G. Browne, I. Raine, D. Strogen, B. Brathwaite, C. Chagué-Goff and J. Palmer, 2010, Middle to Late Eocene stratigraphy, Taranaki basin, New Zealand, A catalogue integrating biostratigraphy, sedimentology, geochemistry, and log data over the NE-SW trending Mangahewa Formation fairway: GNS Science Report No: 2009/30.

Higgs, K. E., P. R. King, J. I. Raine, R. Sykes, G. H. Browne, E. M. Crouch, and J. R. Baur, 2012, Sequence stratigraphy and controls on reservoir sandstone distribution in an Eocene marginal marine-coastal plain fairway, Taranaki Basin, New Zealand: Marine and Petroleum Geology, 32, 1, 110–137.

Holt, W. E., and T. A. Stern, 1994, Subduction, platform subsidence, and foreland thrust loading: The late Tertiary development of Taranaki Basin, New Zealand: Tectonics, 13, 5, 1068–1092.

Honório, B. C. Z., U. M. Da Costa Correia, M. C. De Matos, and A. C. Vidal, 2017, Similarity attributes from differential resolution components: Interpretation, 5, 1, T65–T73.

Infante-Paez, L., and K. J. Marfurt, 2019, Using machine learning as an aid to seismic geomorphology, which attributes are the best input? Interpretation, 7, 3, SE1–SE18.

Johnston, D. H., 1993, Seismic attribute calibration using neural networks: 63th Annual International Meeting, SEG, Expanded Abstract, 250–253.

Johnston, D. H., 2010, Methods and applications in reservoir Geophysics: SEG, Investigations in Geophysics, no. 15, 655 p.

Johnston, D. H., 2013, Practical Applications of Time-lapse Seismic Data: Distinguished Instructor Short Course no. 16, 270 p.

Kharrat, R., R. Mahdavi, M. H. Bagherpour, and S. Hejri, 2009, Rock type and permeability prediction of a heterogeneous carbonate reservoir using artificial neural networks based on flow zone index approach: SPE Middle East Oil and Gas Show and Conference, 1–18.

Kim, Y., and N. Nakata, 2018, Geophysical inversion versus machine learning in inverse problems: Leading Edge, 37, 12, 894–901.

King, P. R., and G. P. Thrasher, 1996, Cretaceous-Cenozoic geology and petroleum systems of the Taranaki Basin, New Zealand: Monograph - Institute of Geological and Nuclear Sciences (New Zealand), 13, 258 p.

Kleemeyer, M., P. Gelderblom, A. Altintas, and K. Foreste, 2012, 4D close-the-loop using probabilistic seismic inversion on the astokh field, offshore Sakhalin: 74th European Association of Geoscientists and Engineers Conference and Exhibition, 648–652.

Kohonen, T., 1982, Self-organized formation of topologically correct feature maps: Biological Cybernetics, 43, 1, 59–69.

Kolodzie, S., 1980, Analysis of pore throat size and use of the waxman-smits equation to determine OOIP in spindle field, Colorado: SPE Annual Technical Conference and Exhibition, 1-10.

Kragh, E., and P. Christie, 2002, Seismic repeatabiliy, normalized rms, and predictability: The Leading Edge, 21, 7, 640–647.

Laudon, C., S. Stanley, and P. Santogrossi, 2019, Machine learning applied to 3D seismic data from the Denver-Julesburg basin improves stratigraphic resolution in the Niobrara: SPE/AAPG/SEG Unconventional Resources Technology Conference, 1–17.

Li, F., and W. Lu, 2014, Coherence attribute at different spectral scales: Interpretation, 2, 1, SA99–SA106.

Li, F., J. Qi, B. Lyu, and K. J. Marfurt, 2018, Multispectral coherence: Interpretation, 6, 1, T61–T69.

Libak, A., B. Alaei, and A. Torabi, 2017, Fault visualization and identification in fault seismic attribute volumes: Implications for fault geometric characterization: Interpretation, 5, 2, B1–B16.

Lowell, J., and V. Erdogan, 2019, Combining Artificial Intelligence with Human Reasoning for Seismic Interpretation James: 89th Annual International Meeting, SEG, Expanded Abstracts, 2353–2357.

Luo, Y., W. G. Higgs, and W. S. Kowalik, 1996, Edge detection and stratigraphic analysis using 3D seismic data: 66th Annual International Meeting, SEG, Expanded Abstracts, 324–327.

MacBeth, C., M. Floricich, and J. Soldo, 2006, Going quantitative with 4D seismic analysis: Geophysical Prospecting, 54, 303–317.

MacBeth, C., Y. HajNasser, K. Stephen, and A. Gardiner, 2011, Exploring the effect of meso-scale shale beds on a reservoir's overall stress sensitivity to seismic waves: Geophysical Prospecting, 59, 1, 90–110.

Mai, H. T., K. J. Marfurt, and S. Chávez-Pérez, 2009, Coherence and volumetric curvatures and their spatial relationship to faults and folds, an example from Chicontepec basin, Mexico: 79th Annual International Meeting, SEG, Expanded Abstracts, 1063–1067.

Marfurt, K. J., 2017, Interpretational aspects of multispectral coherence: EAGE Conference and Exhibition.

Marfurt, K. J., 2018, Seismic attributes as the framework for data integration throughout the oilfield life cycle: SEG Distinguished Instructor Short Course, no. 21, 494 p.

Marfurt, K. J., and R. L. Kirlin, 2001, Narrow-band spectral analysis and thin-bed tuning: Geophysics, 66, 4, 1274–1283.

Martin, A. J., S. T. Solomon, and D. J. Hartmann, 1997, Characterization of petrophysical flow units in carbonate reservoirs: AAPG Bulletin, 81, 5, 734–759.

Matos, M., P. Osorio, and P. Johann, 2006, Unsupervised seismic facies analysis using continues wavelet transform and self-organizing maps: Geophysics, 72, 1, P9–P21.

Matos, M. C. De, M. M. Yenugu, S. M. Angelo, and K. J. Marfurt, 2011, Integrated seismic texture segmentation and cluster analysis applied to channel delineation and chert reservoir characterization: Geophysics, 76, 5, P11–P21.

McConnell, H., and N. Pannell, 2018, Maui 4D seismic survey: Marine Mammal Impact Assessment: SLR Consulting NZ limited.

Mode, A. W., O. A. Anyiam, and C. N. Onwuchekwa, 2014, Flow unit characterization: Key to delineating reservoir performance in “Aqua-Field”, Niger Delta, Nigeria: Journal of the Geological Society of India, 84, 701–708.

Mohamed, I. A., H. Z. El-Mowafy, D. Kamel, and M. Heikal, 2014, Prestack seismic inversion versus neural-network analysis: A case study in the Scarab field offshore Nile Delta, Egypt: Leading Edge, 33, 5, 498–506.

Mohamed, I. A., M. Hemdan, A. Hosny, and M. Rashidy, 2019, High-resolution water-saturation prediction using geostatistical inversion and neural network methods: Interpretation, 7, 2, T455–T465.

Murray, D., 2010, Maui-5 A well completion report: NZP&M, Ministry of Business, Innovation & Employment (MBIE), New Zealand Unpublished Petroleum Report PR4275.

Murray, D., D. Hadley, J. Davies, and I. Mostafa, 2010, MB-03A, MB-05B, and MB-11A/B well completion report: NZP&M, Ministry of Business, Innovation & Employment (MBIE), New Zealand Unpublished Petroleum Report PR4275.

Naeini, E. Z., H. Hoeber, G. Poole, and H. R. Siahkoohi, 2009, Simultaneous multivintage time-shift estimation: Geophysics, 74, 5, V109–V121.

Nasser, M., C. Gronister, B. Hay, and C. Amos, 2017, 4D seismic close-the-loop impacts business decisions at the Okume Complex, Equatorial Guinea: Leading Edge, 36, 5, 394–400.

Nicol, A., J. Walsh, K. Berryman, and S. Nodder, 2005, Growth of a normal fault by the accumulation of slip over millions of years: Journal of Structural Geology, 27, 327–342.

Nodder, S. D., 1993, Neotectonics of the offshore cape egmont fault zone, Taranaki Basin, New Zealand: New Zealand Journal of Geology and Geophysics, 36, 2, 167–184.

Oliveros, R. B., and B. J. Radovich, 1997, Image-processing display techniques applied to seismic instantaneous attributes over the Gorgon gas field, North West Shelf, Australia: 67th Annual International Meeting, SEG, Expanded Abstracts, 2064–2067.

Pannett, S., S. Slager, G. Stone, and S. Dekker, 2004, Constraining a complex gas-water dynamic model using 4D seismic: SPE Annual Technical Conference and Exhibition, 209–225.

Partyka, G., J. Gridley, and J. Lopez, 1999, Interpretational applications of spectral decomposition in reservoir characterization: The Leading Edge, 18, 3, 353–360.

Pedersen, S. I., T. Randen, L. Sønneland, and Ø. Steen, 2002, Automatic fault extraction using artificial ants: 72th Annual International Meeting, SEG, Expanded Abstracts: 512–515.

Pedersen, S. I., T. Skov, A. Hetlelid, P. Fayemendy, T. Randen, and L. Sønneland, 2003, New paradigm of fault interpretation: 73rd Annual International Meeting, SEG, Expanded Abstracts, 350-353.

Qi, X., and K. Marfurt, 2018, Volumetric aberrancy to map subtle faults and flexures: Interpretation, 6, 2, T349–T365.

Radiansyah, J., T. E. Putra, R. Ismail, R. A. Wibowo, E. E. Riza, and M. Kurniawan, 2014, Reservoir description using hydraulic flow unit and petrophysical rock type of pmt carbonate early Miocene of Baturaja Formation , South Sumatra Basin: AAPG International Conference & Exhibition, Extended Abstract.

Rahimpour-Bonab, H., H. Mehrabi, A. Navidtalab, and E. Izadi-Mazidi, 2012, Flow unit distribution and reservoir modelling in Cretaceous carbonates of the sarvak formation, Abteymour Oilfield, Dezful embayment, SW Iran: Journal of Petroleum Geology, 35, 3, 213–236.

Rahimpour-Bonab, H., A. H. Enayati-Bidgoli, A. Navidtalab, and H. Mehrabi, 2014, Appraisal of intra reservoir barriers in the Permo-Triassic successions of the central Persian Gulf, Offshore Iran: Geologica Acta, 12, 1, 87–107.

Randen, T., E. Monsen, C. Signer, A. Abrahamsen, J. O. Hansen, T. Sæter, J. Schlaf, and L. Sønneland, 2000, Three-dimensional texture attributes for seismic data analysis: 70th Annual International Meeting, SEG, Expanded Abstracts, 668-671.

Rangel, R., C. Macbeth, and M. Mangriotis, 2016, The effect of shale activation on 4D seismic interpretation of a UKCS field: 78th EAGE Conference and Exhibition 2016: Efficient Use of Technology - Unlocking Potential.

Reilly, C., A. Nicol, J. J. Walsh, and K. F. Kroeger, 2016, Temporal changes of fault seal and early charge of the Maui gas-condensate field, Taranaki Basin, New Zealand: Marine and Petroleum Geology, 70, 237–250.

Riazi, Z., 2018, Application of integrated rock typing and flow units identification methods for an Iranian carbonate reservoir: Journal of Petroleum Science and Engineering, 160, 1–15.

Roberts, A., 2001, Curvature attributes and their application to 3D interpreted horizons: First Break, 19, 2, 85–100.

Roden, R., T. Smith, and D. Sacrey, 2015, Geologic pattern recognition from seismic attributes: Principal component analysis and self-organizing maps: Interpretation, 3, 4, SAE59–SAE83.

Roden, R., T. Smith, P. Santogrossi, D. Sacrey, and G. Jones, 2017, Seismic interpretation below tuning with multiattribute analysis: Leading Edge, 36, 4, 330–339.

Rojas, N., S. A. Ecopetrol, and T. L. Davis, 2009, Spectral decomposition applied to time-lapse seismic interpretation, Rulison Field, Colorado: 79th Annual International Meeting, SEG, Expanded Abstracts, 3845–3849.

Roy, A., K. J. Marfurt, and M. C. de Matos, 2010, Applying self-organizing maps of multiple attributes, an example from the Red-Fork formation, Anadarko Basin: 80th Annual International Meeting, SEG, Expanded Abstracts, 1591–1595.

Roy, A., M. M. C. de Matos, and K. J. Marfurt, 2011, Application of 3D clustering analysis for Deep marine seismic facies classification—an Example from Deep-Water Northern Gulf of Mexico: Gulf Coast Section SEPM 31st Annual Bob. F. Perkins Research Conference, 410–439.

Roy, A., 2013, Latent space classification of seismic facies, Ph.D. dissertation, University of Oklahoma.

Roy, A., B. L. Dowell, and K. J. Marfurt, 2013, Characterizing a Mississippian Tripolitic Chert reservoir using 3D unsupervised seismic facies analysis and well logs: An example from Osage County, Oklahoma: Interpretation, 1, 2, SB109–SB124.

Russell, B. H., 1988, Introduction to Seismic Inversion Methods, Course note series, no. 2, 176 p.

Russell, B., 2019, Machine learning and geophysical inversion - A numerical study: Leading Edge, 38, 7, 512–519.

Russell, B. H., D. P. Hampson, and L. R. Lines, 2003, Application of the radial basis function neural network to the prediction of log properties from seismic attributes - A channel sand case study: 73rd Annual International Meeting, SEG, Expanded Abstracts, 1–4.

Sacrey, D., and C. Sierra, 2020, Systematic workflow for reservoir characterization in northwestern Colombia using multi-attribute classification: First Break, 38, 77–82.

Sams, M., and D. Carter, 2017, Stuck between a rock and a reflection: A tutorial on low-frequency models for seismic inversion: Interpretation, 5, 2, B17–B27.

Sengupta, M., G. Mavko, and T. Mukerji, 2003, Quantifying subresolution saturation scales from time-lapse seismic data: A reservoir monitoring case study: Geophysics, 68, 3, 803–814.

Seybold, O. M., C. W. Greenstreet and D. Hawton, 1996, Reservoir management of the giant Maui gas/condensate field: New Zealand Petroleum Exploration Conference Proceedings, Ministry of Commerce, Wellington, 125-132.

Sritongthae, W., 2016, Petrophysical Rock Typing: Enhanced permeability prediction and reservoir descriptions: AAPG Geosciences Technology Workshop, Characterization of Asian Hydrocarbon Reservoirs, Bangkok, Thailand.

Stolz, A. K., and R. M. Graves, 2003, Sensitivity study of flow unit definition by use of reservoir simulation: SPE Annual Technical Conference and Exhibition: 1927–1940.

Strecker, U., and R. Uden, 2002, Data mining of 3D poststack seismic attribute volumes using Kohonen self-organizing maps: The Leading Edge, 21, 10, 1032–1037.

Strogen, D. P., H. Seebeck, A. Nicol, K. Bland, P. R. King, and A. J. Tulloch, 2015, Rift to drift on the edge of Gondwana: two-phase Cretaceous-Paleocene rifting in the Taranaki basin, New Zealand: International Conference & Exhibition, AAPG, Melbourne, Australia.

Taner, M. T., F. Koehler, and R. E. Sheriff, 1979, Complex seismic trace analysis: Geophysics, 44, no. 6, 1041–1063.

Taner, M. T., J. S. Schuelke, R. O'Doherty, and E. Baysal, 1994, Seismic attributes revisited, 64th Annual International Meeting, SEG, Expanded Abstract, 1104–1106.

Taner, M. T., 2001, Seismic attributes: Canadian Society of Exploration Geophysicists Recorder, 26, no. 7, 1–15.

Tavakoli, V., 2018, Geological core analysis: application to reservoir characterization: SpringerBriefs in Petroleum Geoscience & Engineering, 99 p.

Telford, C., and D. Murray, 2008, MA-02A well completion report: NZP&M, Ministry of Business, Innovation & Employment (MBIE), New Zealand Unpublished Petroleum Report PR4491.

Thangam, A., 2013, MA-04A well completion report: NZP&M, Ministry of Business, Innovation & Employment (MBIE), New Zealand Unpublished Petroleum Report PR4821.

Thangam, A., 2015, MA-09A and MA-09B well completion report: NZP&M, Ministry of Business, Innovation & Employment (MBIE), New Zealand Unpublished Petroleum Report PR4821.

Tian, S., A. Shams, and C. MacBeth, 2014, Closing the loops using engineering-consistent 4D seismic inversion: Leading Edge, 33, 2, 188–196.

Van Benten, J.A., 1986, Petrophysical properties of core samples from well Maui-5, PML 381012: NZP&M, Ministry of Business, Innovation & Employment (MBIE), New Zealand Unpublished Petroleum Report PR1227.

Van Benten, J.A., 1987, Petrophysical properties of core samples from well Maui-6, PML 381012: NZP&M, Ministry of Business, Innovation & Employment (MBIE), New Zealand Unpublished Petroleum Report PR1269.

Van Benten, J.A., 1987, Petrophysical properties of core samples from well Maui-7, PML 381012: NZP&M, Ministry of Business, Innovation & Employment (MBIE), New Zealand Unpublished Petroleum Report PR1300.

Van der Veeken, J. P. M., and J. B. M. Lutz, 2008, Maui PreSDM 2006 processing: NZP&M, Ministry of Business, Innovation & Employment (MBIE), New Zealand Unpublished Petroleum Report PR4491.

Van der Veeken, 2016, 4D PreSDM processing for the Maui base and monitor surveys: NZP&M, Ministry of Business, Innovation & Employment (MBIE), New Zealand Unpublished Petroleum Report, PR5377.

White, J. C., G. A. Williams, S. Grude, and R. A. Chadwick, 2015, Utilizing spectral decomposition to determine the distribution of injected CO2 at the Snøhvit Field: Geophysical Prospecting, 63, 5, 1213–1223.

Winland, H.D., 1972, Oil accumulation in response to pore size changes, Weyburn Field, Saskatchewan: Amoco Production Research Report, No. F72-G-25.

Wu, X., Y. Shi, S. Fomel, L. Liang, Q. Zhang, and A. Z. Yusifov, 2019, FaultNet3D: predicting fault probabilities, strikes, and dips with a single convolutional neural network: IEEE Transactions on Geoscience and Remote Sensing, 57, 11, 9138–9155.

Xue, Y., 2013, Novel stochastic inversion methods and workflow for reservoir characterization and monitoring, Ph.D. dissertation, University of Texas at Austin.

Xue, Y., M. Araujo, J. Lopez, K. Wang, and G. Kumar, 2019, Machine learning to reduce cycle time for time-lapse seismic data assimilation into reservoir management: Interpretation, 7, 3, SE123–SE130.

Zhang, Z., A. D. Halpert, L. Bandura, and A. D. Coumont, 2018, Machine learning based technique for lithology and fluid content prediction - case study from offshore West Africa: 88th Annual International Meeting, SEG, Expanded Abstracts, 2271–2276.

Zhao, T., 2019, 3D convolutional neural networks for efficient fault detection and orientation estimation: 89th Annual International Meeting, SEG, Expanded Abstracts: 2418–2422.

Zhao, T., 2018, Seismic facies classification using different deep convolutional neural networks: 88th Annual International Meeting, SEG, Expanded Abstracts, 2046-2050.

Zhao, T., V. Jayaram, A. Roy, and K. J. Marfurt, 2015, A comparison of classification techniques for seismic facies recognition: Interpretation, 3, 4, SAE29–SAE58.

Zhao, B., D. H. Johnston, and W. Gouveia, 2006, Spectral decomposition of 4D seismic data: 76th Annual International Meeting, SEG, Expanded Abstract, 3235–3239.

Zhao, T., F. Li, and K. J. Marfurt, 2018, Seismic attribute selection for unsupervised seismic facies analysis using user-guided data-adaptive weights: Geophysics, 83, 2, O31–O44.

Zhao, T., J. Zhang, F. Li, and K. J. Marfurt, 2016, Characterizing a turbidite system in Canterbury Basin, New Zealand, using seismic attributes and distance-preserving self-organizing maps: Interpretation, 4, 1, SB79–SB89.

APPENDICES

APPENDIX A

Seismic data conditioning

Some data quality analysis and data conditioning have been performed on the final 2006 processed seismic volume. This includes seismic data resampling, amplitude spectrum investigation and application of structure-oriented filtering to remove random noise and improve the imagining of structural and stratigraphic features.

Data resampling and polarity

The original seismic amplitude volume provided by MBIE was sampled at 4 ms sampling interval. The machine learning analysis including SOM is a kind of geostatistical analysis that requires a lot of data. Reducing the sampling interval to 2 ms will provide more data points for the SOM analysis. The original seismic volume was resampled to 2 ms sampling interval.

Seismic data provided by MBIE was in European polarity (negative amplitude numbers indicate increase in acoustic impedance). To ease the geological interpretation of the seismic data and time-lapse seismic analysis, the amplitude of all the seismic volumes (merged and time-lapse seismic amplitude data) was multiplied by -1 to get all the data in American polarity (positive amplitude numbers indicate increase in amplitude).

Amplitude spectrum and spectral balancing

After investigating the amplitude spectrum of the merged seismic volume, reviewing the processing report provided by MBIE, and discussion with Shell processing individual (personal communication), and the data seemed to be spectrally balanced (Figure A.1). As discussed in Chapter 1, the pre-processed 2002 seismic data from the 2002 processing project was complemented by the 1991 seismic data in the DMO processing step. This required frequency spectrum equalization, amplitude spectrum equalization and time alignment of both surveys (van der Veeken and Lutz, 2008). Within these processing steps, spectral balancing is applied to the data (personal communication).

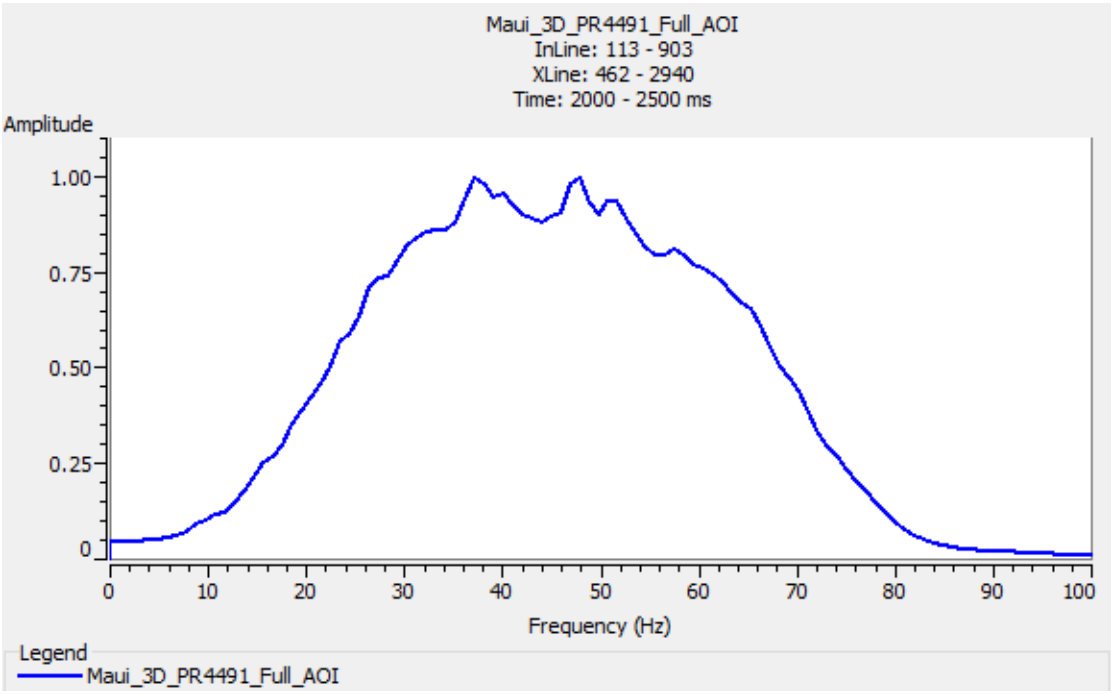

Figure A. 1. Amplitude spectrum of 2006 processed merged seismic volume around the reservoir interval; 2000-2500 ms.

Structure-oriented filtering (SOF)

Although the quality of the seismic data provided by the MBIE is good, some acquisition artifacts and random noise have been observed. The principal component structure-oriented filter (PC SOF) was applied to the seismic data to remove the random noise and provide better quality attribute image. The inline dip, crossline dip, dip magnitude, and dip azimuth have been calculated by using the gradient structure tensor algorithm. The amplitude seismic volume, inline dip, and crossline dip were used to calculate the energy ratio similarity volume. The amplitude seismic volume, energy ratio volume, inline, and crossline dip components of the reflector were used as input volumes to the PC-SOF analysis to enhance the signal along the reflector and suppress random noise (Figure A.2).

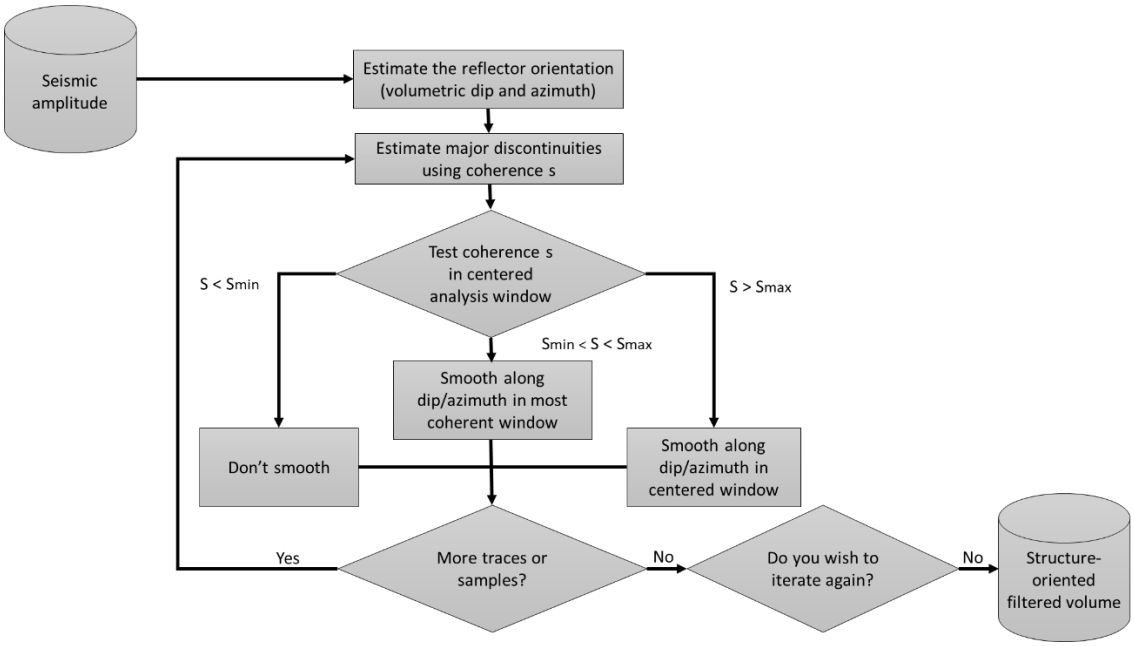

Figure A. 2. PC SOF workflow (modified from Marfurt, 2018)

Given the good quality of the input seismic data, the PC-SOF was selected over the other algorithms (alpha-trimmed mean filter, lower-upper-median filter, and mean filter) to preserve the seismic amplitude. Figure A.3 shows the original amplitude data, the data after the first and second iterations of PC-SOF and rejected noise. The seismic reflectors look more coherent (red arrows) and the faults seem to be sharper (green arrows). The rejected noise after the second PC-SOF is little compared to the first PC SOF iteration (Figures A.3d and A.3e).

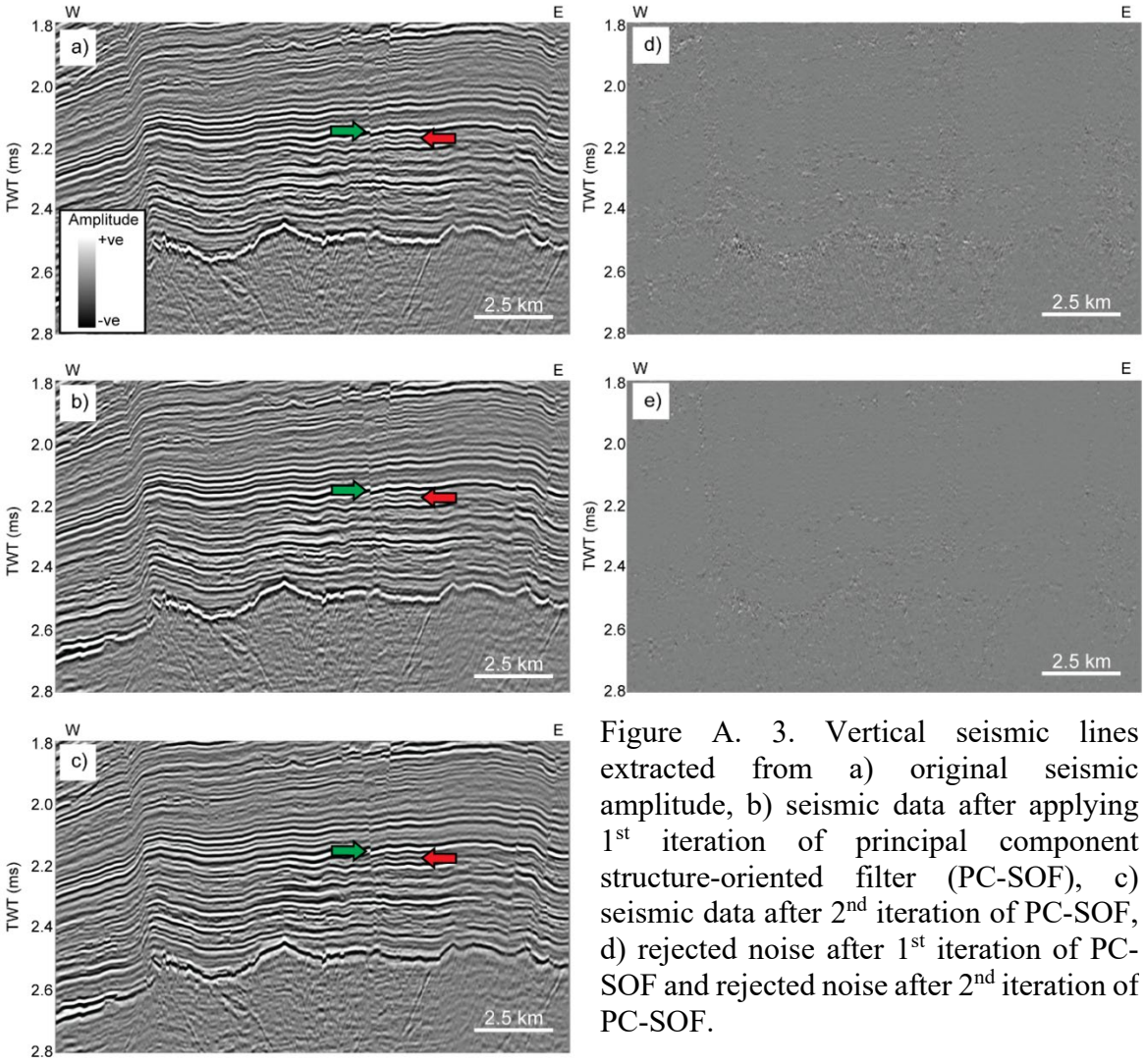

Figure A. 3. Vertical seismic lines extracted from a) original seismic amplitude, b) seismic data after applying 1st iteration of principal component structure-oriented filter (PC-SOF), c) seismic data after 2nd iteration of PC-SOF, d) rejected noise after 1st iteration of PC-SOF and rejected noise after 2nd iteration of PC-SOF.

APPENDIX B

Mathematical background of seismic attributes

In this appendix, I summarize the mathematical concepts of the attributes that I use in this paper. More detailed definitions of these attributes are available in Chopra and Marfurt, 2007a and Marfurt, 2018, which were adapted from Sheriff, 2002.

Dip attributes

Apparent inline and crossline dip components of seismic reflections

The apparent dip is defined by the change in the reflector time or depth with respect to distance in a specific direction and is measured in m/m or s/m. According to SEGY convention, the x-axis refers to the east and the y-axis refers to the north. The apparent north component (inline) of reflector dip p_y and the east component (crossline) reflector dip p_x can be calculated as follows

$$p_x = \frac{\partial t}{\partial x}, \tag{B-1}$$

and

$$p_x = \frac{\partial t}{\partial y}. \tag{B-2}$$

Dip magnitude and dip azimuth

The dip magnitude measures the magnitude of the vector dip$|p|$, which is given by

$$|p| = \left(p_x^2 + p_y^2\right)^{0.5}. \tag{B-3}$$

A compressional velocity of 4000 m/s for the C Sand formation was used to calculate the angular dip θ, which is given by

$$\theta = tan^{-1}\left[\frac{V_p}{2}\left(p_x^2 + p_y^2\right)^{0.5}\right]. \quad \text{(B-4)}$$

The dip azimuth relative to north direction can be calculated as follows

$$\Psi = ATAN2(p_x, p_y) \quad \text{(B-5)}$$

where $ATAN2$ ranges between -180° and 180°

Coherence attributes

Coherence attributes such as energy ratio similarity and the eigenstructure similarity described by Gersztenkorn and Marfurt (1999), measure the lateral changes in waveform only. In this study, I compute the covariance matrix by using the original data (d) and its Hilbert transform (dH). I estimate the energy ratio similarity along structural dip of M traces within a ± K sample analysis window as the ratio between the coherent energy (d_{KL}) and the total energy (d_{KL}^H) as follows

$$C_{ER} = \frac{\sum_{m=1}^{M}\sum_{k=-K}^{K}\left\{[d_{KL}(t_k,x_m,y_m)]^2 + \left[d_{KL}^H(t_k,x_m,y_m)\right]^2\right\}}{\sum_{m=1}^{M}\sum_{k=-K}^{K}\{[d(t_k,x_m,y_m)]^2 + [d^H(t_k,x_m,y_m)]^2\}} \quad \text{(B-6)}$$

where t_k represents the time of structurally interpolated sample at (x_m, y_m) distance from the analysis point$(x = 0, y = 0, t = 0)$. The coherent energy is calculated by using the Karhunen-Loeve filter.

Other coherence attributes sensitive to lateral changes in waveform and amplitude include outer product, semblance-based similarity and Sobel filter similarity attributes. The semblance-based similarity calculates the ratio of the energy of the average analytic trace to the average of the energy of each analytic trace along the structural dip. I use the analytic trace (i.e. original seismic trace and its Hilbert transform) to reduce structural leakage for small windows about zero crossings of the real seismic wavelet. The Sobel filter similarity is calculated along structure dip by normalizing the inline and crossline derivative by the energy. In this study, I calculate these different coherence attributes and all of them provide similar images. However, the energy ratio similarity provides a relatively clear image compared to other coherence attributes. As a result, I use it an example of coherence attributes.

Multispectral coherence attribute

To calculate the multispectral energy ratio attribute, I follow Marfurt's (2017) approach and apply five different band-pass filter banks to the input seismic volume to obtain five spectral voices. I calculate the multispectral energy ratio similarity using a co-variance matrix computed along structural dip using these spectral voices and their Hilbert transforms as shown below

$$C_{mn} = \sum_{l=1}^{L} \sum_{k=-K}^{K} [u(t_k, f_l, x_m, y_m)\, u(t_k, f_l, x_n, y_n) + u^H(t_k, f_l, x_m, y_m)\, u^H(t_k, f_l, x_n, y_n)] \quad \text{(B-7)}$$

Then I calculate the coherence for each spectral voice component.

Amplitude gradients

The inline and crossline amplitude gradients are defined by computing the derivatives of the coherent energy along structural dip in the inline and crossline directions. This can be done by calculating the inline and crossline derivatives of the eigenmap (the first eigenvector), which describes the data in the analysis window. These derivatives can be weighted by the energy, root mean square amplitude (RMS), envelope, or impedance inversion volumes. The energy-weighted amplitude gradients (g) can be computed as follows

$$g = \begin{pmatrix} g_x \\ g_y \end{pmatrix} = \lambda_1 \begin{pmatrix} \frac{\partial v^{(1)}(x,y)}{\partial x} \\ \frac{\partial v^{(1)}(x,y)}{\partial y} \end{pmatrix}. \tag{B-8}$$

where λ_1 is the first eigenvalue that measures the amount of energy represented by its corresponding eigenvector and $\frac{\partial v^{(1)}(x,y)}{\partial x}$ and $\frac{\partial v^{(1)}(x,y)}{\partial y}$ define the derivatives of the eigenmap. The resulting inline and crossline amplitude gradient maps look like shaded relief maps. However, they represent lateral energy variation, not changes in time structure (Marfurt, 2018).

Curvature attributes

Structural curvature

I calculate the structural curvature as the first derivative of the volumetric inline and crossline components of dip. I compute the long-wavelength and short-wavelength curvature volume by applying different linear band pass filter operators to the curvature results. The most positive (K_1) and most negative (K_2) curvatures are used to calculate the curvedness (C) and shape index (S) as follows

$$C = (K_1^2 + K_2^2)^2. \quad \text{(B-9)}$$

and

$$S = -\frac{2}{\Pi} ATAN\left(\frac{K_2 + K_1}{K_2 - K_1}\right). \quad \text{(B-10)}$$

The details of this implementation can be found Chopra and Marfurt (2007).

Amplitude curvature

The amplitude curvatures are computed by taking the first derivatives of the amplitude gradients in the inline and crossline directions. Like the structural curvature, I apply the same short-wavelength and long-wavelength filter operators to the curvature results. In our example, these attributes show the acquisition artifacts.

Reflector rotation

To compute the reflector rotation, I first calculate the normal vector, n, from the apparent dip components, p and q, and then compute the curl of n, $\Psi = \nabla$ x n. The reflector rotation about the normal can be defined as the components of curl parallel to the average normal (Marfurt and Rich, 2010)

$$K_{rot} = \bar{n}.\Psi = \bar{n}_x\left(\frac{\partial n_y}{\partial z} - \frac{\partial n_z}{\partial y}\right) + \bar{n}_y\left(\frac{\partial n_z}{\partial x} - \frac{\partial n_x}{\partial z}\right) + \bar{n}_z\left(\frac{\partial n_x}{\partial y} - \frac{\partial n_y}{\partial x}\right) \quad \text{(B-11)}$$

Euler curvature

Similar to the apparent dip calculations, I compute the volumetric Euler curvature at different azimuth directions (Ψ') relative to the north as follows

$$K'_{\Psi} = K_1\, cos^2(\Psi' - \Psi'_2) + K_2\, sin^2(\Psi' - \Psi'_2) \quad \text{(B-12)}$$

where (K_1, Ψ_1) and (K_2, Ψ_2) represent the magnitude and strike of the most positive and most negative principal curvatures (Chopra and Marfurt, 2014).

Aberrancy

Aberrancy measures the third derivative of reflection time or depth, so its computation is complicated compared to the curvature calculations because no eigenvalue and eigenvector solution has been found yet for aberrancy calculations. In this work, I follow Qi and Marfurt's (2018) approach and compute the second derivatives of the dip components in the original coordinate system. Then I rotate or flatten the dip components and the derivative operators at each voxel then the apparent aberrancy at any azimuth (Ψ) can be computed as follows

$$f(\Psi) = \frac{\partial^3 z'}{\partial x'^3}\, cos^3\Psi + 3\,\frac{\partial^3 z'}{\partial x'^2\,\partial y'}\, cos^2\,\Psi\, sin\,\Psi + 3\,\frac{\partial^3 z'}{\partial x'\,\partial y'^2}\, cos\Psi\, sin^2\Psi + \frac{\partial^3 z'}{\partial y'^3}\, sin^3\Psi \tag{B-13}$$

The extrema of the aberrancy are computed by determining the roots of the above equation. These extrema represent the maximum, intermediate and minimum aberrancy vectors that can be expressed by their magnitude $f(\Psi)$ and azimuth (Ψ).

Gray-level co-occurrence matrix (GLCM)

GLCM is a matrix that quantifies the lateral changes in seismic amplitude (reflectivity) along structural dip. Haralick et al. (1973) showed that 14 various textural attributes can be derived from the GLCMs. Each attribute images a specific property. These attributes can be combined into three different groups: contrast, orderliness and statistic groups (Marfurt, 2018). The contrast attribute (C_{GLCM}) quantifies the local variations within an image and can be computed as follows (Chopra and Marfurt, 2006).

$$C_{GLCM} = \sum_{i=-L}^{+L}\sum_{j=-L}^{+L} P_{ij}(i-j)^2 \tag{B-14}$$

where $2L+1$ is the number of gray levels

The dissimilarity attribute D_{GLCM} can be calculated as follows

$$D_{GLCM} = \sum_{i=-L}^{+L}\sum_{i=-L}^{+L} P_{ij}|i-j| \tag{B-15}$$

The homogeneity attribute H_{GLCM} measures the smoothness of an image and can be calculated as follows

$$H_{GLCM} = \sum_{i=-L}^{+L} \sum_{j=-L}^{+L} \frac{P_{ij}}{1+(i-j)^2} \quad \text{(B-16)}$$

The energy attribute E_{GLCM} measures the degree of textural uniformity within an image and can be computed as follows

$$E_{GLCM} = \left(\sum_{i=-L}^{+L} \sum_{j=-L}^{+L} P_{ij}^2\right)^{0.5} \quad \text{(B-17)}$$

The entropy S_{GLCM} describes the disorderliness (or roughness) of a patch of seismic amplitude. It can be computed as follows

$$S_{GLCM} = \sum_{i=-L}^{+L} \sum_{j=-L}^{+L} P_{ij} \left(\ln P_{ij}\right) \quad \text{(B-18)}$$